SEARCHES FOR VECTOR-LIKE QUARKS DECAYING TO W BOSONS AND MODULE PLACEMENT QUALITY ASSURANCE FOR THE ATLAS ITK UPGRADE

By

JOSHUA R. STEWART

Bachelor of Business Administration
New Mexico State University
Las Cruces, New Mexico
2009

Bachelor of Science in Physics
Cameron University
Lawton, Oklahoma
2018

Master of Science in Physics
Oklahoma State University
Stillwater, Oklahoma
2022

Submitted to the Faculty of the
Graduate College of the
Oklahoma State University
in partial fulfillment of
the requirements for
the Degree of
DOCTOR OF PHILOSOPHY
May, 2024

SEARCHES FOR VECTOR-LIKE QUARKS DECAYING TO W BOSONS AND MODULE PLACEMENT QUALITY ASSURANCE FOR THE ATLAS ITK UPGRADE

Dissertation Approved:

Dr. Joseph Haley

Dissertation Advisor

Dr. Alexander Khanov

Dr. Flera Rizatdinova

Dr. Yolanda Vasquez

ACKNOWLEDGMENTS

I've been incredibly blessed with people in my life who have been dedicated to guiding me and teaching me how to make wise decisions. Navigating life's challenges requires a reliable compass, and I've found that in the principles taught to me by those closest to me. Foremost, I am deeply thankful to my parents for instilling in me the belief that God is that unwavering true north, providing guidance through the most trying times. Without the hope He has instilled in me, I would have given up long before discovering my passion for physics.

My wife Jackie and my children, Josie and Joseph, have been the bedrock of my inspiration. They give me compelling reasons to persevere during tough times. My family has supported me unwaveringly, offering comfort and refuge when obstacles cloud my path. Josie and Joseph remind me daily to prioritize fatherhood above all else, helping me to leave professional concerns at the door. Jackie's relentless support and belief in my dreams, even as we've moved across the country, have deeply touched me. Her forgiveness and commitment are lessons in true humility and nurture.

I owe a great deal of gratitude to Dr. Saeed Ahmed and Dr. Narayan Thapa, my undergraduate advisors. They saw potential in me I hadn't recognized, encouraging me to pursue graduate studies and join a select group dedicated to uncovering universal truths. Their belief in my abilities has been a gift.

Acknowledgments reflect the views of the author and are not endorsed by committee members or Oklahoma State University.

Additionally, Dr. Joseph G. Haley, my Advisor, has been an indispensable mentor. Amidst my doubts and anxieties, his faith in me helped me find my own confidence. Unlike others who might have left me to my own devices, he generously shared his passion for understanding, teaching me in ways that resonated deeply. We have discussed, argued, agreed and disagreed on many things, ultimately learning a great deal from each other about life in general. My decision to come to Okalhoma State University was centered on the quality of the people that I would be working most closely with. Now that my time here is coming to an end, I can say that I made a very good decision.

To everyone who has been a part of this life-long journey to becoming a Doctor of Physics, I extend my deepest thanks. Your support has been a cornerstone of my success.

Acknowledgments reflect the views of the author and are not endorsed by committee members or Oklahoma State University.

Name: JOSHUA R. STEWART

Date of Degree: MAY 2024

Title of Study: SEARCHES FOR VECTOR-LIKE QUARKS DECAYING TO W BOSONS AND MODULE PLACEMENT QUALITY ASSURANCE FOR THE ATLAS ITK UPGRADE

Major Field: PHYSICS

Abstract:

This dissertation explores the realm of particle physics through two distinct yet interconnected lenses: the search for Vector-Like Quarks (VLQs), and the quality assurance in module placement for the ATLAS Inner Tracker (ITk) upgrade in preparation for the High Luminosity Large Hadron Collider (HL-LHC). The Standard Model (SM) of particle physics explains many natural phenomena yet remains incomplete. VLQs lie at the heart of many extensions to the SM seeking to address the hierarchy problem. VLQs could be produced either singly or in pairs, and then decay to a SM boson and a third-generation quark. While single-production depends on the coupling of the VLQ to the SM particles, pair-production via the QCD interaction provides a model-independent test for VLQs. This paper presents a search for singly- and pair-produced VLQs. The pair-production analysis considers VLQs that decay into a W boson and a bottom quark, with one W decaying leptonically while the other decays hadronically. The analysis uses b-tagging algorithms, charge asymmetry metrics, multiple on-line triggers, and data driven corrections of the ttbar and W+jets background Monte Carlo samples to improve sensitivity during the analysis of the full LHC Run 2 ATLAS dataset. Maximum excluded mass limits were set in this analysis at 1500 GeV for the $\mathcal{B}(T \rightarrow Wb) = 1$ scenario. Similar methodologies were followed in the Single VLQ analysis, but remains in the stages of unblinding. Finally, the paper explores the technical challenges and innovations surrounding the ATLAS ITk upgrade, focusing on ensuring the utmost precision in module placement for the inner detector rings and staves. Through comprehensive data analysis and experimental rigor, this dissertation not only contributes to our understanding of fundamental particles but also enhances the technological framework essential for future discoveries in high-energy physics.

TABLE OF CONTENTS

LIST OF TABLES

LIST OF FIGURES

Figure Page

Figure Page

Figure Page

NOMENCLATURE

HEP	High Energy Physics
CERN	European Council for Nuclear Research
LHC	Large Hadron Collider
HL-LHC	High Luminosity Large Hadron Collider
ITk	Inner Tracker
VLQ	Vector-Like Quark
VLT	Vector-Like T Quark
VLB	Vector-Like B Quark
BSM	Beyond Standard Model
VEV	Vacuum Expectation Value
$E_{\mathrm{T}}^{\mathrm{miss}}$	Missing Transverse Momentum
ID	Inner Detector
TDAQ	Trigger and Data Acquisition
SCT	Semi-Conductor Tracker
TRT	Transition Radiation Tracker
IBL	Insertable B-Layer
LAr	Liquid Argon
FCal	Forward Calorimeter
HLT	High Level Trigger

$\mathrm{n_{eq}/cm^2}$	Neutron Equivalent
pp	Proton-Proton
MC	Monte Carlo
PDF	Parton Distribution Function
COM	Center of Mass
LLP	Long-Lived Particles
LRT	Large Radius Tracking
PV	Primary Vertex
p_T	Transverse Momentum
EM	Electro-Magnetic
JVT	Jet Vertex Trigger
MET	Missing Transverse Energy
CR	Control Region
VR	Validation Region
SR	Signal Region
MVA	Multivariate Analysis
NP	Nuisance Parameter
SF	Scale Factor
LLR	Log Likelihood Ration
CL	Confidence Level
S+B	Signal-Plus Background

CHAPTER I

PRELUDE

1.1 A Brief History of Physics

The endless quest to understand the universe's fundamental nature has been an enduring force in human inquiry since the beginning of existence. At the heart of this intellectual odyssey lies physics, the foundational science that seeks answers to the profound questions posed by the observed universe.

Tracing the roots of physics catapults us back to ancient civilizations, where early thinkers endeavored to unravel the mysteries of the natural world through a tapestry woven with threads of philosophy and keen observation.

From the philosophical thought experiments of Thales in ancient Greece—often hailed as the first philosopher—who contemplated the essence of matter and postulated water as the fundamental substance, to the continued explorations of successors like Anaximander and Heraclitus, a gradual evolution from philosophical pondering to scientific inquiry took shape. This transformation reached its peak with Aristotle, whose comprehensive system of natural philosophy, despite facing subsequent challenges and revisions, left an indelible mark, shaping the worldview of medieval thinkers [83].

As the march of time continued, the Renaissance heralded a pivotal moment in the study of physics—the Copernican Revolution. Nicolaus Copernicus dared to challenge the centuries-old geocentric view, proposing a heliocentric model that not only revolutionized our understanding of the solar system but also laid the groundwork for a more empirical approach to scientific thought [75].

The 17th century witnessed the development of the scientific method—an approach characterized by systematic investigation, empirical observation, and mathematical analysis. Galileo Galilei's telescopic revelations and Johannes Kepler's laws of planetary motion enriched the scientific realm. The pinnacle of this era materialized with Sir Isaac Newton's Principia Mathematica, a collection that elegantly formulated the laws of motion and universal gravitation, providing a unifying framework for understanding celestial and terrestrial phenomena.

As we skip forward to the 19th century, we see new frontiers on the horizon, with Michael Faraday's pioneering work on electricity and magnetism laying the groundwork for James Clerk Maxwell's unification of these forces—a synthesis immortalized in a set of equations that became a cornerstone of classical physics (elegantly named, Maxwell's Equations) [64]. Simultaneously, Rudolf Clausius and Lord Kelvin expanded the scope of physics with groundbreaking contributions to thermodynamics, developing the principles governing heat and energy transfer.

The early 20th century witnessed a dual revolution: Albert Einstein's theories of relativity and the advent of quantum mechanics. Einstein's conceptual upheaval transformed our perception of space, time, and gravity, challenging the well-established Newtonian model. Concurrently, quantum mechanics, with its wave-particle duality and probabilistic nature, introduced a profound level of uncertainty that defied classical intuition [70].

In the latter half of the 20th century, particle physics achieved monumental strides with the formulation of the Standard Model. This theoretical edifice successfully unified electromagnetic, weak, and strong nuclear forces, offering a comprehensive description of elementary particles.

1.2 Synopsis

This paper continues our exploration of physics, beginning with the Standard Model. It is proposed in such a way as to offer a holistic approach to the research topics. The main text is brief and easy to read, while more detail can be found in the associated appendices.

To begin, in Chapter II the existence of elementary particles and their interactions will be defined, navigating the elegant framework that describes the subatomic realm. Chapter III sets the stage for the proposed analyses, introducing Vector-Like Quarks (VLQ's) as an intriguing extension of the known particle spectrum. Moving deeper into the heart of experimental particle physics, the chapters on the Large Hadron Collider (LHC), the ATLAS detector and experimental methods will serve as a guide through the design, function, and groundbreaking experiments conducted within the world's most powerful particle accelerator.

With the needed definitions now in place, the two subsequent chapters (VII and VIII) focus on the analyses "Wb+X" and "Single VLQ," which dissect the methodologies and outcomes of these studies.

Following the VLQ searches, the future of the LHC now comes into view. The chapter on the High Luminosity LHC (HL-LHC) unveils the next era of experimental endeavors, examining upgrades and advancements planned for the LHC. Our exploration concludes with a technological spotlight in Chapter X, "Module Placement Quality Assurance". Here, we delve into the engineering precision required to optimize the performance of the Inner Tracker (ITk), a crucial component for unraveling the secrets hidden within particle collisions.

This comprehensive overview offers readers a roadmap for the multifaceted exploration of particle physics—spanning theoretical foundations, cutting-edge experimental analyses, and the technological innovations propelling the field forward.

CHAPTER II

THE STANDARD MODEL

The Standard Model of Particle Physics stands as a pinnacle in our understanding of the fundamental constituents of the universe and the forces governing their interactions. This theoretical framework, developed over several decades, elegantly encapsulates the diversity of subatomic particles and their intricate interplay. In this comprehensive exploration, we delve into the historical evolution of the Standard Model, highlight the key scientists behind its development, and elucidate its core principles.

2.1 Historical Background

The roots of the Standard Model trace back to the mid-20th century when physicists were grappling with the bewildering variety of particles discovered in cosmic rays and particle accelerators. The framework took shape in the 1960s and 1970s, emerging from the convergence of various theoretical developments.

The foundation for the Standard Model was laid by the success of Quantum Electrodynamics (QED), developed by Nobel laureates Richard Feynman, Julian Schwinger, and Sin-Itiro Tomonaga in the late 1940s [55, 80, 86]. QED successfully described electromagnetic interactions among charged particles. In the 1970s, Sheldon Glashow, Abdus Salam, and Steven Weinberg independently proposed a unification of electromagnetism and the weak nuclear force, leading to the electroweak theory [62, 78, 88]. This groundbreaking idea was later integrated into the Standard Model. The development of Quantum Chromodynamics (QCD), describing the strong force binding quarks within protons and neutrons, was spearheaded by physicists such as Murray Gell-Mann and George Zweig [61, 57]. The missing piece to endow particles with mass was provided by the Higgs mechanism, proposed independently by Robert Brout and François Englert, and by Peter Higgs [46, 67]. The discovery of the Higgs boson in 2012 at CERN's Large Hadron Collider validated this pivotal aspect of the Standard Model [9][51].

2.2 Key Principles of the Standard Model

The Standard Model classifies elementary particles into two main categories based on their intrinsic spin [65] as shown in Figure 1.

1. Fermions: These are particles with half-integer spin, constituting matter. Quarks (up, down, charm, strange, top, bottom) and leptons (electron, muon, tau, and their associated neutrinos) are fermions. They obey Fermi-Dirac statistics (see appendix B), which describe the statistical behavior of particles with half-integer spin. Fermions exhibit the Pauli exclusion principle, preventing two identical fermions from occupying the same quantum state simultaneously.

2. Bosons: These are particles with integer spin, serving as force carriers. Gauge bosons (see appendix J) mediate fundamental forces: photons for electromagnetism, W and Z bosons for the weak force, and gluons for the strong force. The Higgs boson, though a scalar boson, also plays a crucial role by imparting mass to particles. Bosons follow Bose-Einstein statistics (see appendix B), governing the behavior of particles with integer spin. Unlike fermions, bosons can occupy the same quantum state simultaneously, leading to phenomena like Bose-Einstein condensation.

In addition to the intrinsic spin angular momentum of the particle, the Standard Model involves a complex web of quantum numbers that characterize fundamental particles and their interactions [85]. Electric charge, a fundamental property, defines the strength and direction of electromagnetic interactions, with quarks and charged leptons carrying various electric charges. Color charge, a property related to the strong force in quantum chromo-

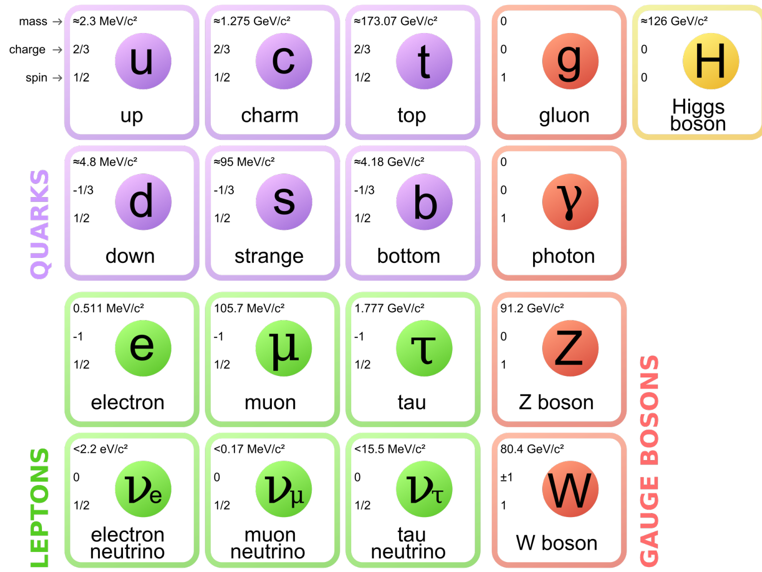

Figure 1: Diagram showing the particles in mass eigenstates (sans anti-particles) in the Standard Model of Particle Physics.

dynamics, distinguishes quarks, which can exhibit three different colors (red, green, blue) or their corresponding anti-colors. Weak isospin and weak hypercharge are associated with the weak force, influencing processes like beta decay, and particles such as electrons and neutrinos possess specific values for these quantum numbers. The Lorentz invariant relative to Helicity, Chirality further refines the classification of particles into left-handed and right-handed chiral states. (see appendix G).

Particles exist in mass eigenstates, states that interact with the Higgs field and have definite masses [85]. These are the states in which we label particles (except Neutrinos)because of their constant interaction with the Higgs field. Flavor quantum numbers differentiate between particle generations, such as up and down quarks or the three generations of leptons.

The interaction of particles with gauge bosons further defines their behavior. The photon mediates electromagnetic interactions and interacts with charged particles carrying electric charge. The W and Z bosons, responsible for the weak force, interact with particles possessing weak isospin and weak hyper-charge, influencing processes like beta decay and neutrino interactions. Gluons mediate the strong force, binding quarks within hadrons, and their exchange contributes to the color-charged interactions between quarks.

In essence, this intricate interplay of quantum numbers and interactions governs the classification and behavior of particles within the Standard Model, providing a comprehensive framework for understanding the fundamental forces shaping the universe.

2.2.1 Standard Model Lagrangian

The evolution from Schrödinger's wave equation to Dirac's relativistic wave equation marked a pivotal shift in the landscape of quantum mechanics (see appendix D). In the 1920s, Schrödinger formulated a wave equation that described the non-relativistic behavior of quantum particles [63]. However, as the need to extend quantum mechanics to relativistic speeds became apparent, Paul Dirac introduced the Dirac equation in 1928. This equation, incorporating special relativity, successfully described the behavior of fermions, particularly electrons, and introduced the concept of spin through the use of 4-component spinors [65].

Dirac's work laid the groundwork for the development of quantum field theory (QFT), a framework that treats particles as manifestations of underlying fields. In QFT, Lagrangians are employed to describe the dynamics and interactions of these fields. Despite the departure from classical mechanics, where Lagrangians describe particle trajectories, the quantum field Lagrangian serves a similar purpose, albeit in the context of fields.

The Lagrangian in quantum field theory is a function that, when integrated over spacetime, yields the action—a fundamental quantity (see appendix E). The principle of least action, familiar from classical mechanics, asserts that the true path of a system minimizes the action. By varying the fields in the Lagrangian and setting the variation of the action to zero, the Euler-Lagrange equations are derived. These equations dictate the evolution of fields over spacetime, providing predictions for changes in particle properties.

Therefore, the Lagrangian in quantum field theory, building on the foundations laid by Dirac, not only describes the dynamics of fields and their interactions but also predicts changes in particle properties, including momentum. This framework has proven to be a powerful and successful tool for understanding the behavior of particles within the principles of quantum mechanics and relativity.

2.2.2 Higgs Mechanism

The Higgs mechanism, a pivotal component of the Standard Model of Particle Physics, addresses the longstanding puzzle of how elementary particles acquire mass. The mechanism introduces the concept of a Higgs field that pervades all of space [46, 67]. Unlike familiar force fields, the Higgs field does not diminish with distance and has a non-zero value even in the vacuum, the vacuum expectation value. As particles such as quarks and leptons move through the Higgs field, they experience resistance, somewhat akin to moving through a thick syrup. This resistance, imparted by the Higgs field, manifests as mass for certain particles, while others with weaker interactions remain relatively massless.

The mathematical formulation of the Higgs mechanism involves the Standard Model Lagrangian (see appendix E), a formalism describing the dynamics of particle fields. The key mathematical elements include the introduction of a complex doublet of scalar fields, known as the Higgs doublet, and a potential energy term that ensures spontaneous symmetry breaking [46, 67] (see appendix C and I). This potential energy with the non-zero vacuum expectation value leads to spontaneous symmetry breaking, breaking the electroweak symmetry and resulting in the emergence of mass for both fermions and gauge bosons. See details in appendix C.

Experimental validation of the Higgs mechanism occurred through the search for the Higgs boson at the Large Hadron Collider (LHC). Proton-proton collisions at the LHC, conducted at high energies, created conditions where the Higgs field could be excited, leading to the production of Higgs bosons. The detection of decay products from these bosons provided compelling evidence supporting the existence of the Higgs field and its role in granting mass to particles [9, 51]. See Figure 2 for the confirmation of the Higgs at 125 GeV (gigaelectronvolts) in the $H \rightarrow 4l$ analysis.

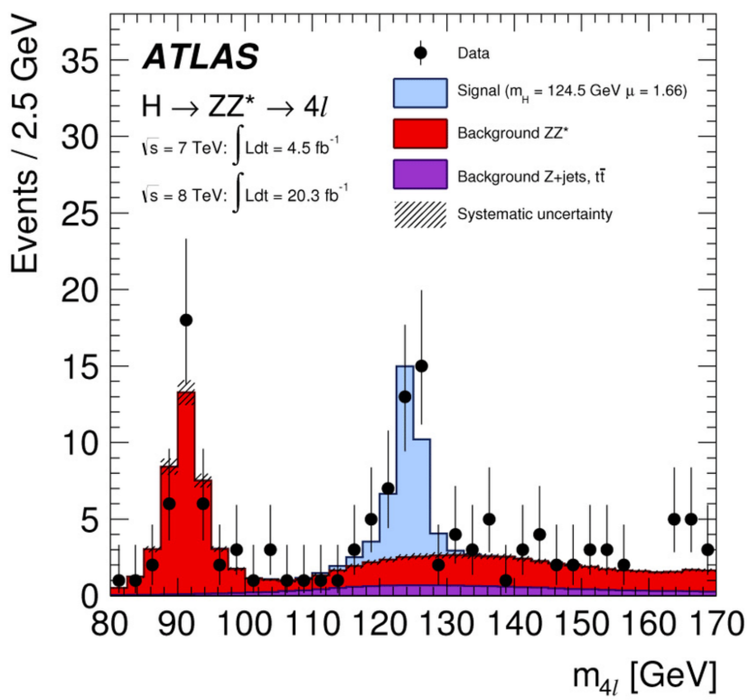

Figure 2: Four-lepton invariant mass distribution for the Higgs boson candidates in the ATLAS detector (CERN). The blue shaded region is the contribution from the Higgs boson at 125 GeV, if the Higgs did not exist, the data points in black would match the red shaded in region [67].

The significance of the Higgs mechanism extends beyond resolving the mystery of mass generation. It plays a crucial role in the electroweak unification, explaining how the electromagnetic force and the weak nuclear force, initially distinct, become unified at high energies. Moreover, the presence of the Higgs field throughout space has cosmic implications, influencing the properties of particles and fields during the early moments of the universe. In essence, the Higgs mechanism stands as a cornerstone in our understanding of the subatomic world, providing profound insights into the fundamental forces that shape the fabric of our universe.

2.2.3 Invariant Amplitude

As with any quantum mechanical system, the results are probabilistic [63]. The invariant amplitude is the key concept in particle physics that predicts the probability of various outcomes or interactions. It represents the probability amplitude for a particular process to occur. It's "invariant" because it is independent of the coordinate system or frame of reference.

In the framework of the Standard Model (SM) of particle physics, Feynman rules are used to calculate the invariant amplitude for a given process. The Feynman rules provide a systematic way to associate mathematical expressions with different components of a Feynman diagram, which is a graphical representation of particle interactions (see appendix F).

In summary, the most useful value to have is the invariant amplitude, which is a fundamental quantity in quantum field theory. The total amplitude is obtained by summing over all relevant Feynman diagrams for a given process. For the following experiments mentioned in this paper, this quantity is pivotal in order to develop predictions about the outcomes of high energy proton collisions.

CHAPTER III

BEYOND STANDARD MODEL PHYSICS

The SM aims to describe how all fundamental matter interacts. If it were a perfectly complete theory, it could be extended to any scale. However, we find that it still has limitations, expecially at the cosmic scale. This can only mean that the search for such a complete theory is not yet finished. "Beyond the Standard Model (BSM)" physics refers to a fascinating and cutting-edge realm in the field of theoretical and experimental physics that explores the mysteries lying beyond the well-established framework of the Standard Model (SM).

3.1 Limitations in the Standard Model

Despite its remarkable success, the SM of particle physics has limitations and leaves several experimental observations unexplained. Some of the phenomena that the Standard Model cannot directly account for include:

1. **Dark Matter:** The SM does not include a particle that could account for dark matter, which is most likely a new form of matter that does not interact with electromagnetic forces and thus cannot be directly observed. Observations from cosmology and astrophysics strongly suggest the presence of dark matter, but its nature remains one of the biggest mysteries in contemporary physics.

2. **Neutrino Mass:** While an extension of the SM has been proposed to incorporate neutrino masses, the original formulation assumed that neutrinos were massless. Neutrino oscillation experiments have confirmed that neutrinos do have mass, challenging the initial assumptions of the Standard Model.

3. **Gravity Integration:** The Standard Model successfully describes the electromagnetic, weak, and strong nuclear forces, but it does not include gravity. Efforts to incorporate gravity within the framework of quantum mechanics have been challenging, and a unified theory of all fundamental forces, including gravity, remains elusive.

4. **Cosmic Asymmetry:** The observed predominance of matter over antimatter in the universe, known as baryon asymmetry, is not adequately explained by the Standard Model. The mechanisms within the model do not generate a sufficient imbalance between matter and antimatter to account for the universe's observed composition.

5. **Hierarchy Problem:** The Standard Model does not provide a natural explanation for the vast disparity in the strength of gravity compared to the other fundamental forces. This hierarchy problem raises questions about the stability of the mass of the Higgs boson and suggests that there might be new physics beyond the Standard Model at energy scales that have not yet been probed.

The analyses proposed in this paper are searching for a particle that would help rectify the Hierarchy Problem specifically. Naturally, if one of these problems is solved, it may pave the way to the solution of others.

3.1.1 Hierarchy Problem

To grasp the intricacies of the Hierarchy Problem, it is essential to understand the concept of "naturalness." This notion states that within significantly small sample sets, outcomes with exceedingly low probabilities, although statistically possible, are not naturally favored. To illustrate, winning the lottery on a single attempt in a lifetime would be perceived as highly unnatural due to the improbability of such an event. The mass of the Higgs boson is much more incredible, if the events of the last example are considered unnatural.

The Higgs boson mass can be described in terms of its "bare mass" and "quantum corrections" within the framework of Quantum Field Theory. In the Standard Model of particle physics, the Higgs boson mass is subject to quantum corrections due to interactions with other particles and fields.

The bare mass of the Higgs boson is a theoretical parameter introduced in the Lagrangian of the theory. However, the observed mass of the Higgs boson, denoted as m_H, is influenced by quantum corrections arising from virtual particle loops in Feynman diagrams.

The relationship can be expressed as:

$$m_H^2 = m_{\text{bare}}^2 + \delta m^2 \tag{3.1.1}$$

where:

- m_H is the observed mass of the Higgs boson
- m_{bare} is the bare mass
- δm^2 represents the quantum corrections

The observed mass (m_H) of the Higgs boson, measured experimentally, is on the order of 10^2 GeV. The bare mass (m_{bare}), which represents the mass at the tree level without quantum corrections, is expected to be around the Planck scale, approximately 10^{18} GeV. The quantum corrections (δm) arise from interactions with other particles and contribute at the loop level, typically on the order of 10^{10} GeV or higher [54].

This significant discrepancy in orders of magnitude between the observed mass and the bare mass, along with the substantial contributions from quantum corrections, underscores the unnaturalness of the Higgs boson mass. The need for fine-tuning (the notion these values were "made this way" rather than occurring at random) to reconcile these values challenges the notion of naturalness, as such a delicate balance is unlikely to occur without some underlying reason or additional physics yet to be discovered.

3.2 Vector-Like Quarks

The two searches in this paper seek Vector-Like Quarks (VLQs), therefore we will focus on defining it here. VLQs are a hypothetical type of quark that differs from the usual quarks in terms of its interactions under the Standard Model (see appendix G and H). Its main attributes are:

1. **Electric Charge:**

   VLQs carry electric charges that are integer multiples of the elementary charge ($e/3$) (see Figure 3 for more details).

2. **Weak Isospin:**

   VLQs may come as a weak isospin singlet, or have different weak isospin quantum numbers (see Figure 4).

3. **Intrinsic Spin:**

   VLQs are fermions and, as such, have intrinsic spins. SM quarks have spin-$\frac{1}{2}$, similarly VLQs also have spin-$\frac{1}{2}$. (see Figure 3 for more details).

4. **Color Charges:**

   Quarks carry color charges, which are associated with the Strong force. The color charges of VLQs are similar to those of standard quarks and can be red (r), green (g), or blue (b), along with their corresponding antiparticles carrying anti-color charges.

5. **Chirality:**

   This is what gives Vector-Like Quarks their name. VLQ's interact with the Weak force equally with their left and right handed components, see appendix G.

VLQs can play a role in addressing the hierarchy problem through their contributions to the quantum corrections (Figure 5). The idea is that the effects of VLQs could cancel or significantly reduce the large quantum corrections to the Higgs boson mass, that are mainly

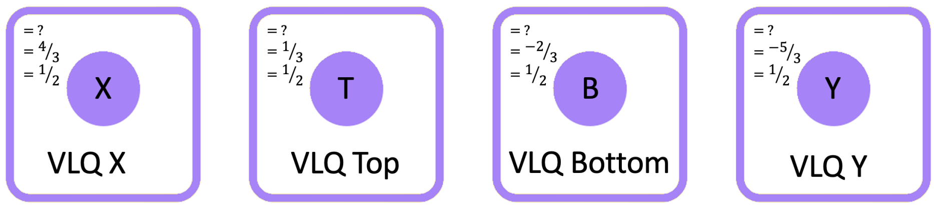

Figure 3: A figure of possible VLQ's in weak eigenstates. Attributes from top to bottom: mass, electric charge, spin

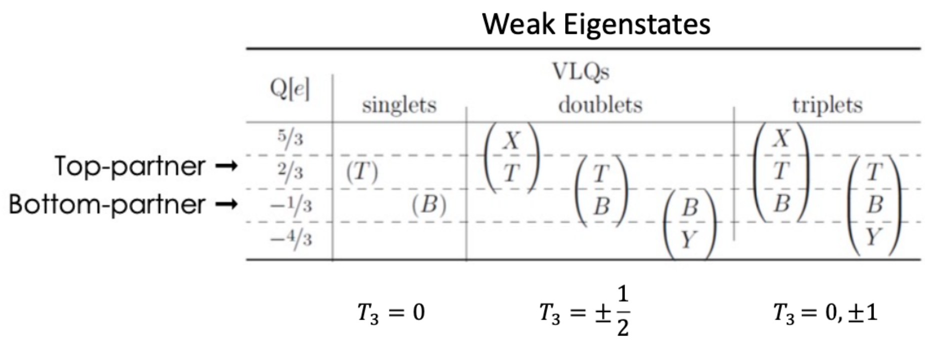

Figure 4: VLQ's can come in singlets, doublets or triplets. This is highly model dependent. The X and Y VLQ have identical mass and weak eigenstates, while the T and B mix with the SM top and bottom.

attributed to the SM t and its large coupling to the Higgs field. The radiative corrections from the VLQs would have the opposite sign as the SM t, making it is possible to achieve a more natural and stable hierarchy between the electroweak and Planck scales.

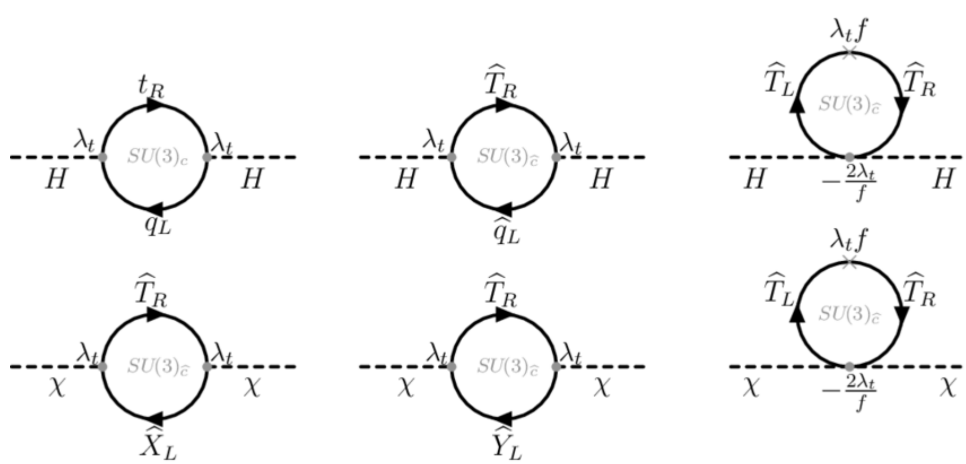

Figure 5: The cancellation mechanism can be understood by considering the loop diagrams in Feynman diagrams. The VLQ loops introduce negative contributions that can offset the positive contributions from the top quark loop, leading to a more stable Higgs boson mass [66].

Considering the example of the Higgs boson mass mentioned above, the addition of VLQ's to the SM would mean that the quantum correction value (δm) to the Higgs mass would be much smaller, making the unnaturalness of the problem much less.

CHAPTER IV

LARGE HADRON COLLIDER

The theoretical framework has been stated. To accept or deny any extensions to the SM, we must introduce an experimental apparatus; for these analyses, it will be the Large Hadron Collider (LHC). Before getting into details, some key events will be explored that shaped the Large Hadron Collider as we know it today.

The LHC is the world's largest and most powerful particle accelerator, located at CERN (European Council for Nuclear Research) near Geneva, Switzerland. Its history can be traced back to the early 1980s when discussions and plans for a new accelerator at CERN began. However, the actual construction of the LHC took place over several decades, and it officially started operating in 2008.

4.1 Physical Characteristics

The LHC is a remarkable feat of engineering with impressive physical dimensions and capabilities:

- **Diameter:** The LHC is a circular accelerator with a circumference of approximately 27 kilometers (about 17 miles).

- **Depth:** It is located about 100 meters (328 feet) underground, spanning the border between Switzerland and France.

- **Magnets:** The LHC utilizes powerful superconducting magnets, with some capable of generating magnetic fields over 100,000 times stronger than the Earth's magnetic field.

- **Temperature:** The LHC operates at extremely low temperatures to maintain the superconducting state of its magnets. The temperature inside the accelerator can be as low as 1.9 Kelvin (-456.3 degrees Fahrenheit), just above absolute zero.

- **Proton Acceleration:** Protons within the LHC are accelerated to nearly the speed of light. The accelerator can propel protons to energies of up to 7 teraelectronvolts (TeV).

- **Collisions:** The primary purpose of the LHC is to collide protons at high energies. These collisions allow scientists to study fundamental particles and recreate conditions similar to those just after the Big Bang.

4.2 Timeline of Key Events

The concept for the LHC traces its roots back to the 1980s, when discussions emerged about the necessity for a more powerful particle accelerator to delve into new frontiers in particle physics. The formal approval for the LHC project came in 1994, marking the beginning of an ambitious undertaking in the realm of experimental physics [72].

The construction of the LHC was a monumental collaborative effort, involving thousands of scientists and engineers from across the globe. This circular tunnel, approximately 17 miles (27 kilometers) in circumference, was built underground. Despite facing various technical and financial challenges, the construction successfully concluded in 2008, showcasing the dedication and cooperation of the international scientific community.

In September 2008, the LHC saw its first operational beam. However, a mere nine days later, a significant setback occurred—a Helium leak, leading to a swift shutdown. The subsequent year was dedicated to repairs and improvements, addressing the issues that had arisen [68].

The LHC re-entered the scientific stage in November 2009, marking the beginning of a new era in particle physics. In July 2012, scientists at CERN made a groundbreaking announcement—the discovery of the Higgs boson, the last missing elementary particle predicted by the Standard Model of particle physics [47].

Following this pivotal discovery, the LHC continued its operations, providing valuable data for a myriad of experiments. The ensuing years have seen researchers making significant contributions to our comprehension of fundamental particles and forces in the universe. The LHC's role expanded to encompass studies on dark matter, antimatter, and the exploration of physics beyond the Standard Model.

As of the present day, the LHC remains at the forefront of experimental particle physics, playing an indispensable role in advancing our understanding of the fundamental building blocks of the universe. It stands as a testament to the collaborative spirit of the scientific community and the relentless pursuit of knowledge.

4.3 Acceleration Process

4.3.1 Proton Production

Protons used in the LHC experiments are generated by ionizing hydrogen gas. Hydrogen gas, composed of protons and electrons, is first stripped of its electrons, resulting in a beam of protons. This beam then undergoes a series of radio-frequency (RF) manipulations to form tightly packed proton bunches.

4.3.2 Accelerator Chain

The protons then go through a sequence of accelerators (see Figure 6) before reaching the LHC. The initial acceleration takes place in a linear accelerator (LINAC), followed by the Proton Synchrotron Booster (PSB), the Proton Synchrotron (PS), and the Super Proton Synchrotron (SPS). Each stage increases the energy of the proton bunches, preparing them for injection into the LHC.

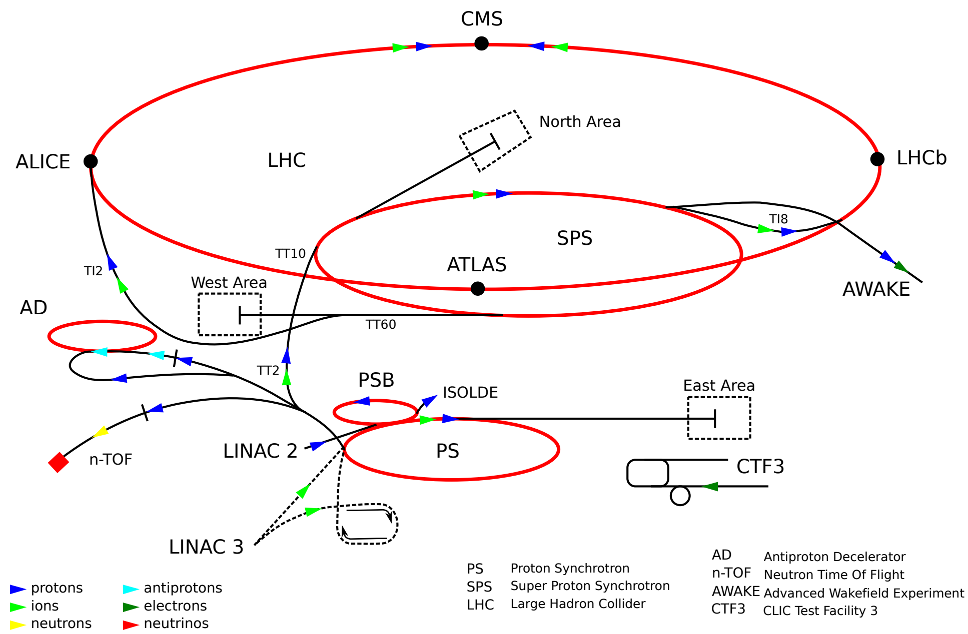

Figure 6: The various steps that the LHC requires to accelerate protons to 6.5 TeV.

The LINAC provides the initial energy boost, followed by further acceleration in the PSB, PS, and SPS. By the time the protons reach the LHC, they have been accelerated to energies on the order of several GeV per nucleon.

The transition into the LHC is a critical phase. During the injection process, protons are carefully guided into the LHC ring through a complex network of beam lines and magnetic fields. This precise arrangement ensures that the protons seamlessly transition into the LHC without losing their high energy or deviating from their trajectory. The LHC operates with two proton beams moving in opposite directions, each within its own ultra-high vacuum pipe. This dual-beam setup is pivotal for the collider's primary purpose of facilitating head-on proton collisions.

Once inside the LHC, the protons are not yet at their maximum energy level. Additional acceleration within the LHC is essential. This is achieved using powerful Radio Frequency (RF) cavities that oscillate at very high frequencies. These cavities boost the energy of the protons each time they pass through, a process that is repeated thousands of times as the protons circulate around the LHC's ring. Through this method, protons achieve energies up to 7 TeV, enabling the LHC to probe the fundamental particles and forces of the universe with unprecedented depth.

4.4 Focusing Beams at LHC Collision Points

The precision focusing of proton beams at the collision points within the LHC is a crucial aspect of experimental design, ensuring accurate and high-energy collisions for the study of fundamental particles and forces. In order to properly focus the proton beams, they must be properly collimated. Collimator systems are strategically placed at various points around the LHC ring to trim and clean the proton beams, ensuring that only well-focused beams reach the collision points. These systems enhance the overall luminosity and minimize unwanted background events in the detectors.

4.4.1 Quadrupole Magnets

To achieve beam focusing, the LHC utilizes a series of quadrupole magnets strategically placed along the accelerator ring at various collision points (see Figure 7). Quadrupole magnets have a unique magnetic field configuration that focuses the proton beams in both horizontal and vertical planes. These magnets play a pivotal role in maintaining the small beam size required for high-luminosity (see appendix K) collisions.

4.4.2 Feedback and Correction

Sophisticated beam control systems continuously monitor and adjust the magnetic fields to correct any deviations in the proton trajectories. Feedback loops based on beam position monitors and corrector magnets contribute to real-time adjustments, maintaining optimal focusing conditions for extended periods.

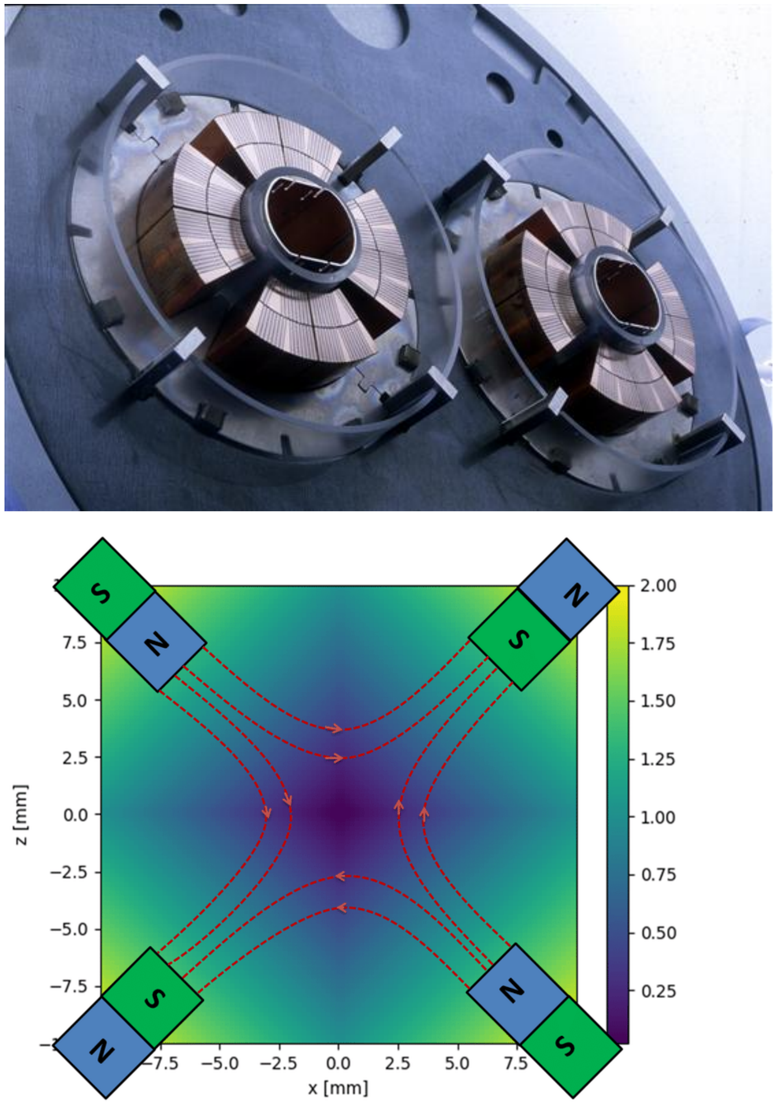

Figure 7: The quadrapole magnets and their focusing feild that squeezes the proton cluster in 2 of the 3 dimensions, temporarily increasing intensity preparing for the collision [2].

4.5 Collected Data

During the entirety of Run 2, the LHC achieved an aggregate integrated luminosity of 156 fb^{-1} [9]. Of this total, the ATLAS experiment succeeded in capturing 147 fb^{-1}, with 140 fb^{-1} of this data being deemed appropriate for physics analysis. Figure 8 illustrates the comparison between the luminosity generated by the LHC and that which was documented by ATLAS.

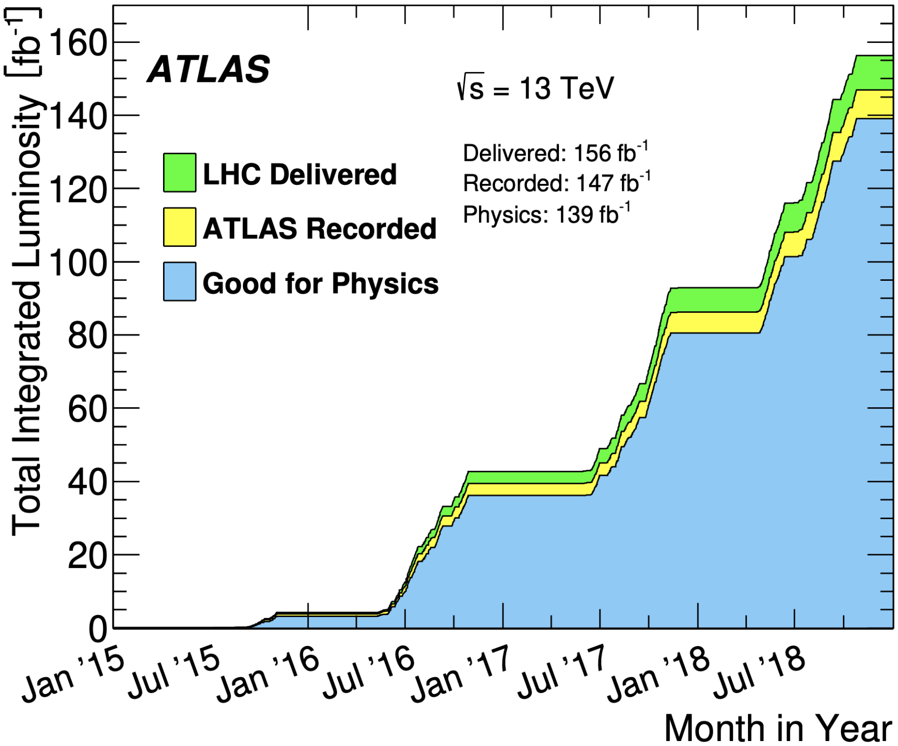

Figure 8: The chart presents a detailed segmentation of the luminosity: it delineates the portion provided by the LHC, the fraction recorded by ATLAS, and the segment deemed suitable for physics analyses, all categorized according to the data collection period [50]

4.6 Pile-up

Amidst the excitement of high-energy proton-proton collisions, scientists grapple with the complex phenomenon known as pile-up within the LHC detectors, a technical challenge that requires thoughtful solutions.

When proton beams collide at the heart of the detectors, they generate a cascade of particles and interactions. Pile-up occurs when multiple proton-proton collisions overlap within the detector, due to the narrow time gap between collisions. This creates a dense and intricate web of particle tracks.

At any given moment, the LHC experiences an enormous number of collisions. The peak luminosity, a measure of collision rates, has reached values of around 2×10^3 collisions per square centimeter per second (see appendix K). This intense collision density results in a multitude of particle tracks and signals within the detectors, leading to challenges in accurately identifying and isolating individual collision events.

One of the primary difficulties lies in the reconstruction of particle tracks amid this chaotic environment. The detectors, such as ATLAS and CMS, record the paths and properties of particles emerging from each collision. However, when multiple collisions occur simultaneously, distinguishing between tracks originating from different events becomes a formidable task.

The CERN clock, a crucial component of the LHC's synchronization system, ensures precise time-stamping of events (every 25 nanoseconds). Given that protons within the accelerator travel at nearly the speed of light, maintaining synchronization across the vast LHC ring is a technological feat. The CERN clock plays a pivotal role in differentiating events, providing a chronological framework for reconstructing all detector signals accurately.

CHAPTER V

ATLAS DETECTOR

Situated at one of the four collision points on the LHC ring, the ATLAS Detector is one of primary experiments. This cylindrical apparatus, with its notable forward-backward symmetry, extends 46 meters in length and 25 meters across in diameter. Encompassing the majority of the solid angle, its architecture comprises three layered subsystems, each engineered to assess diverse particle properties emanating from collision events. For enhanced clarity, a computer-illustrated model of the ATLAS detector is presented, partially sectioned to improve visibility and scaled with human figures, is illustrated in Figure 9.

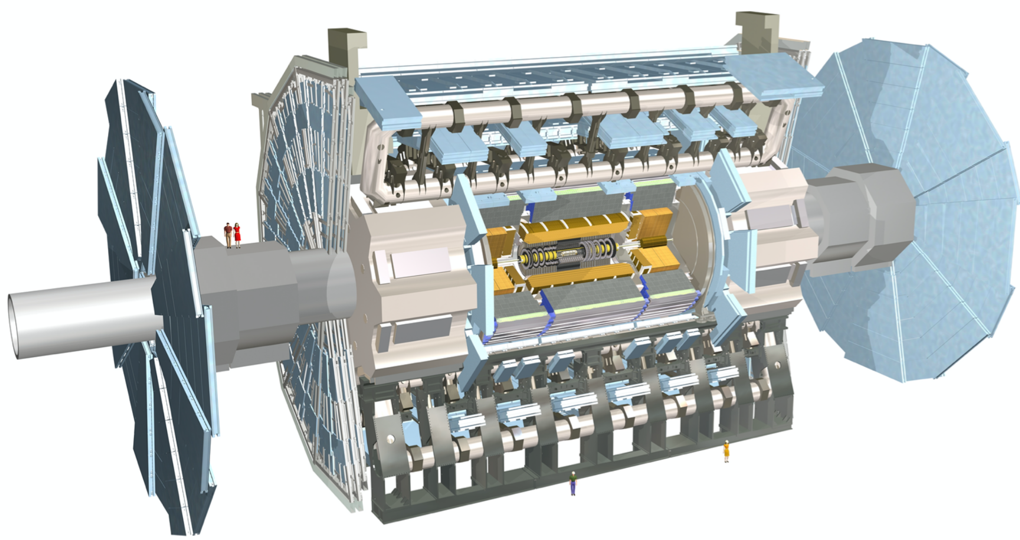

Figure 9: Computer-generated model of the ATLAS detector with a section removed to show the subsystems. Humans are included for scale.

5.1 Coordinate System in the ATLAS Detector

The ATLAS detector at CERN uses a right handed coordinate system with the x-axis pointed toward the inside of the LHC ring. Cylindrical and polar coordinates are also defined for the ease of analyses (see figure 10).

Cylindrical Coordinates

- Radial Distance (r): Distance from the beam axis.
- Azimuthal Angle (ϕ): Angle in the transverse plane.
- Longitudinal Axis (z): Axis parallel to the beam direction.

Polar Coordinates

- Polar Angle (θ): Angle from the beam axis.
- Pseudorapidity (η): Related to rapidity $y = \ln(\frac{E+p_z}{E-p_z})$, $\Delta\eta$ is Lorentz invariant for boost along the z-axis (or beam line). Defined as:

$$\eta = -\ln\left(\tan\left(\frac{\theta}{2}\right)\right) \tag{5.1.1}$$

and is a measure of angle relative to the beam axis (see figure 11).

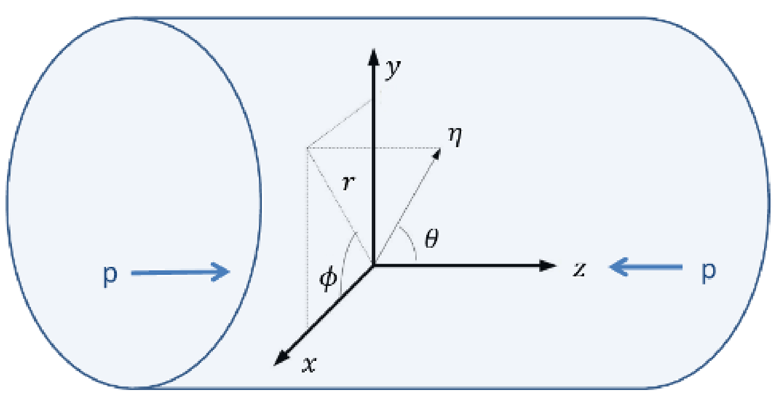

Figure 10: Right handed coordinate system used by ATLAS.

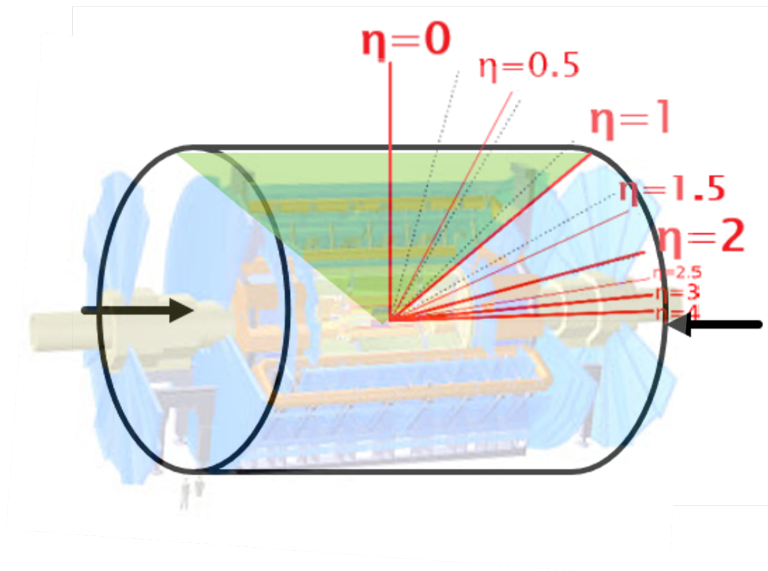

Figure 11: Pseudo rapidity used by ATLAS analyses to provide a Lorentz invariant scale for the partial measurement of the solid angle.

Distance Measurements

In high-energy physics, particularly in the context of the ATLAS detector, distance measurements between particle trajectories are crucial. These are often expressed in terms of angular differences:

An important combined measure of distance in the detector's coordinate system is given by the relationship:

$$\Delta R = \sqrt{(\Delta\eta)^2 + (\Delta\phi)^2} \tag{5.1.2}$$

Where ΔR provides a measure of spatial separation in the $\eta - \phi$ space, combining differences in pseudo-rapidity and azimuthal angle.

5.2 Components of ATLAS

The ATLAS detector comprises three subsystems: the Inner Detector (ID), calorimeters, and muon spectrometers. The ID, located closest to the collision point, measures the trajectory of charged particles created in collisions. Calorimeters measure the energy of electromagnetic and hadronic particles. The muon spectrometer, the final subsystem, measures the path of muons, combining this information with the ID to determine energy and trajectory. Each subsystem includes a barrel region (cylindrical component at low η) and an end-cap region (disk-shaped components at higher η). Neutrinos, commonly produced in interactions but not interacting with the detector, are accounted for through the calculation of Missing Transverse Energy, $E_{\mathrm{T}}^{\mathrm{miss}}$, the negative vector sum of all other transverse momenta (see appendix M).

The ATLAS detector features two different magnetic fields and components for trigger and data acquisition (TDAQ). A solenoid magnet surrounds the ID, and a toroid magnet encircles the muon spectrometer. These magnets cause charged particles to bend as they move through the magnetic fields. The TDAQ system filters out unwanted events and retains desired ones for analysis.

5.2.1 The Inner Detector

The ID [2] is the subsystem closest to the interaction point within ATLAS. Its primary function is to track the path of charged particles produced in Proton-Proton collisions. This subsystem is located within a 2 T solenoid magnet that influences the trajectory of the charged particles. It reconstructs tracks of the charged particles, assisting in defining the transverse momentum of any charged particle produced. The ID is composed of three subsystems:

- The Pixel Detector, using silicon-based sensors to track particle paths.
- The Semi-Conductor Tracker (SCT), also utilizing silicon sensors.
- The Transition Radiation Tracker (TRT), which employs noble gas ionization for trajectory reconstruction.

Figure 12 illustrates the layout of the ID and a representation of track reconstruction from the detector signals.

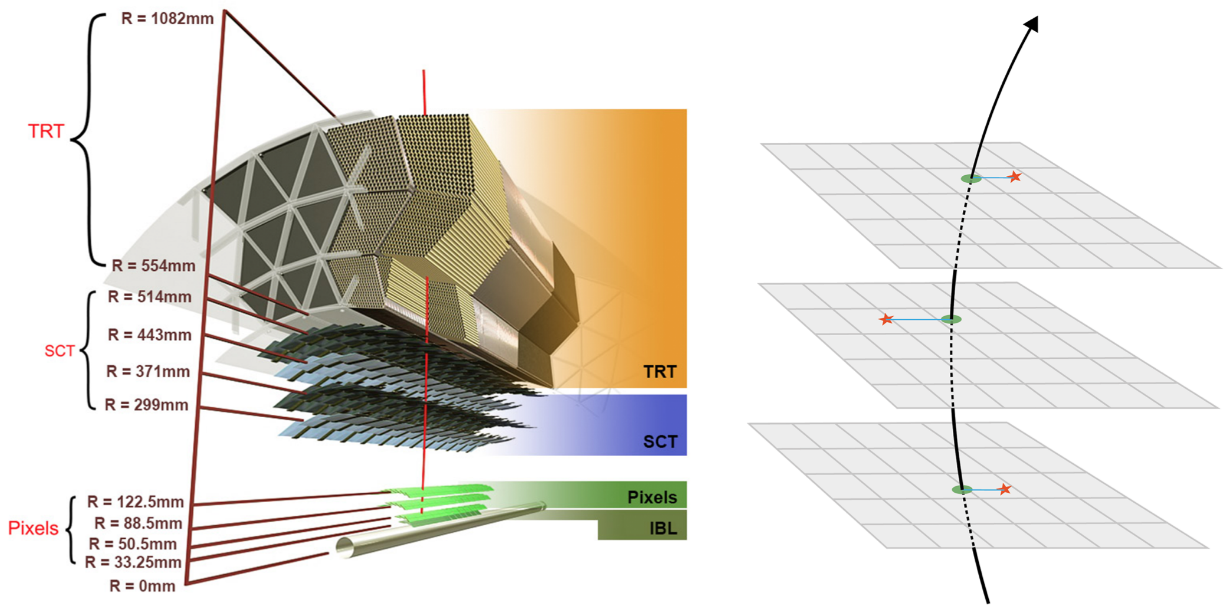

Figure 12: Diagram of the Inner Detector layout showing the subsystems relative to the beam pipe and a schematic of track reconstruction.

The innermost system in the ID is the Pixel Detector, which provides high-efficiency tracking for $|\eta| < 2.5$ [2]. During the first run of ATLAS, the Pixel Detector comprised three sensor layers in the barrel region and three end-cap disks on each side. The barrel layers were located at radii of 50.5 mm, 88.5 mm, and 122.5 mm from the beam pipe, while the disks had sensors at radii of 88.8 mm and 149.6 mm. The detector contained 1744 pixel sensors, each with a size of $50 \times 400 \times 250\,\mu$m, resulting in 46,080 readout channels for tracking. Figure 13 displays the locations of the barrel layers and end-cap rings.

The Insertable B-Layer (IBL) [50] was added to the detector for its second run. This layer introduced an additional sensor layer in the barrel region at a radius of 33.3 mm from the beam pipe center. It comprised 896 sensors, each measuring $50 \times 250 \times 250\,\mu$m, enhancing the Pixel Detector's tracking capabilities, particularly in identifying particles like top and bottom quarks.

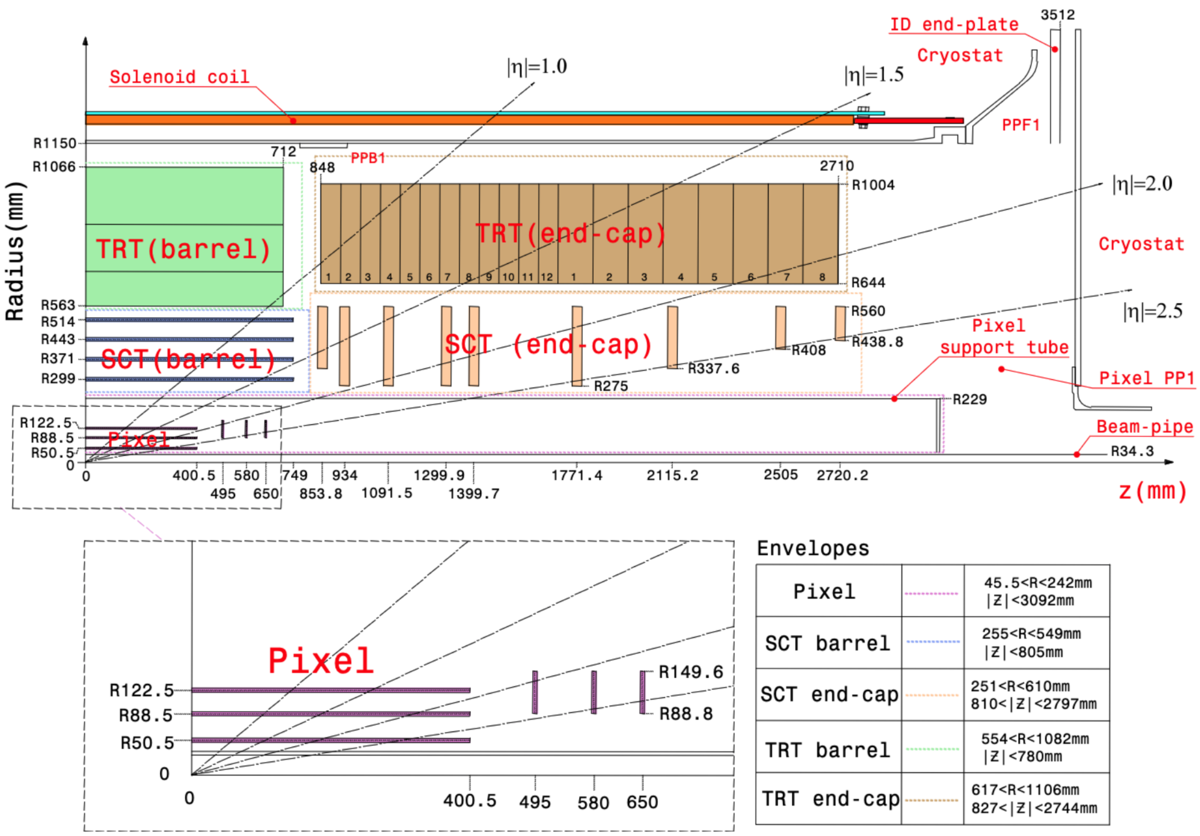

Figure 13: Schematic of the Inner Detector layout for both the barrel and end-cap regions during Run 1, illustrating the pseudo-rapidity coverage and radius of each component [2].

Semi-Conductor Tracker

The SCT [2] follows the Pixel Detector in the ID sequence. It consists of four layers in the barrel region and nine rings in the end-cap. The layers range from radii of 299 mm to 514 mm. The SCT employs silicon strip sensors, each measuring $80 \times 120,000 \times 258\,\mu$m. In total, the SCT uses 15,912 sensors, each with 768 strips.

Transition Radiation Tracker

The final subsystem in the ID is the TRT [35]. It uses a gas mixture of 70% Xenon, 27% Carbon Dioxide, and 3% Oxygen for ionization. At the center of each tube in the TRT is a 31 μm gold-plated tungsten anode, which collects Electrons freed by the ionized gas. The barrel region comprises 73 layers of straws, organized into three concentric rings, totaling 52,544 straws and covering radii from 560 mm to 1080 mm. Each straw, parallel to the beam pipe, measures 142.4 cm in length. The end-caps consist of two types of rings: one with a 4 mm gap between layers and another with a 16 mm space, including 12 mm of the gas mixture. Each end-cap side has 12 of the 4 mm gap rings and eight of the 16 mm gap rings. Although the TRT's spatial resolution is lower than other subsystems, it is particularly effective in distinguishing between particles, notably Electrons and Pions, through transition radiation dependent on the Lorentz γ-factor.

5.2.2 Calorimeters

The calorimeters, situated outside the solenoid, form the next subsystem in ATLAS after the ID. Their role is to measure the energy of outgoing particles. This subsystem includes two types of calorimeters:

- The Electromagnetic Calorimeter, measuring the energy of electromagnetic particles such as Electrons and Photons.
- The Hadronic Calorimeter, gauging the energy of hadronic products from collisions.

Both calorimeters are of the sampling variety, alternating between active and sampling layers. The active layers interact with collision products to create secondary particles, which are then measured by the sampling layers. A calibration process translates the data from the sampling layers into energy measurements. Figure 14 shows the various components of the ATLAS calorimeters.

Electromagnetic Calorimeter

The Electromagnetic Calorimeter [2] uses lead plates interspersed with stainless-steel sheets as the absorber and liquid Argon as the sampling material. Copper electrodes are placed in the gaps of the absorber for signal readout. The absorbers are designed with an accordion

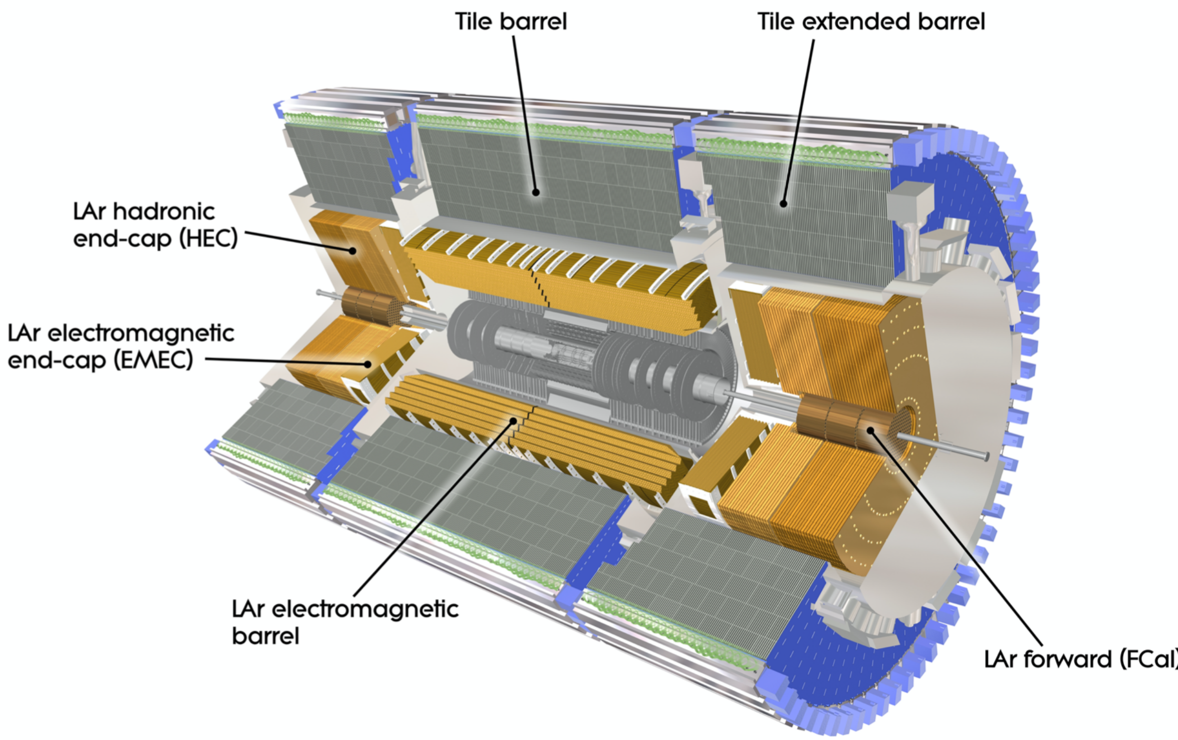

Figure 14: Illustration of the different components of the ATLAS calorimeters.

geometry to ensure full coverage in ϕ and expedite signal extraction. The barrel region of this calorimeter, known as the LAr Electromagnetic Barrel, covers $0 < |\eta| < 1.475$ and is situated between 2.8 m and 4 m from the beam pipe. It comprises three layers, each with decreasing granularity in solid angle as the distance from the beam pipe increases. The end-cap calorimeters, each containing a wheel, span $1.375 < |\eta| < 3.2$. The space between the end-cap and barrel calorimeters is filled with a liquid Argon pre-sampler to enhance measurement accuracy in this region. Each end-cap features two co-axial wheels separated by a 3 mm gap at $|\eta| = 2.5$. This section of the calorimeter is known as the LAr Electromagnetic End-cap. A schematic of the calorimeter geometry near $\eta = 0$ is shown in Figure 15.

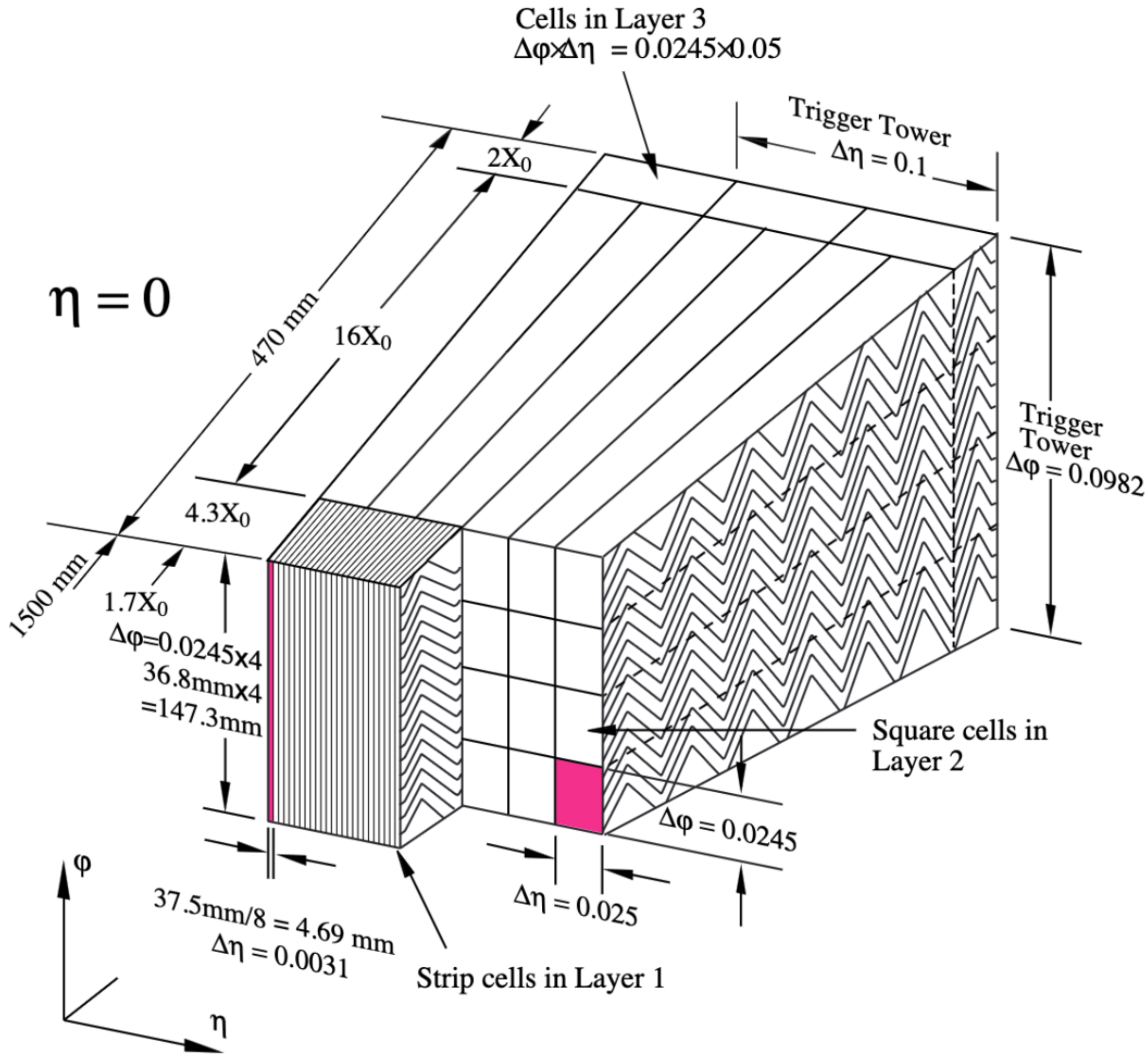

Figure 15: Diagram of the three LAr calorimeter layers and their granularity at each layer [2].

Hadronic Calorimeter

The Hadronic Calorimeter [2] is another sampling calorimeter, comprising the Tile Barrel, the LAr Hadronic End-cap (HEC), and the LAr Forward Calorimeter (FCal). The Barrel utilizes steel as the absorber and scintillators as the sampling material. Wavelength-shifting fibers transmit signals from the scintillators to photomultiplier tubes, which record the output. The layout of the Tile Barrel is illustrated in Figure 16. The Tile Barrel includes a central component, 5.8 m in length, and two 2.6 m Tile Extended Barrels on either side, collectively covering $|\eta| < 1.7$. The HEC and FCal employ copper as the absorber and liquid argon as the sampler. The HEC comprises two wheels covering $1.5 < |\eta| < 3.2$, while the FCal includes three cylinders spanning $3.1 < |\eta| < 4.9$. Due to its positioning at higher η, the FCal encounters a greater flux of particles, leading to a reduction in the size of liquid Argon-filled gaps to mitigate ion buildup. The HEC and FCal are housed within the same cryostat, creating a highly integrated system that minimizes energy loss between the components.

5.2.3 Muon Spectrometer

The final subsystem within ATLAS is the Muon Spectrometer [2]. It consists of three concentric cylinders in the barrel region, with radii of 5 m, 7.5 m, and 10 m, and four disks at approximately $|z| = 7.4$ m, 10.8 m, 14 m, and 21.5 m. The layouts of the barrel components (in green) and the disks (in light blue) are shown in Figure 17. These cylinders and disks utilize Monitored Drift Tubes (MDTs) with a radius of about 30 mm, filled with a gas mixture of 93% Argon and 7% Carbon Dioxide, covering $|\eta| < 2.7$. The first end-cap disk employs Cathode-Strip Chambers (CSC) for $|\eta| > 2$, where particle flux is highest. The CSCs feature cathodes perpendicular to the central wires in the drift tubes, with the induced charge on the cathodes providing the signal. The barrel region of the muon spectrometer is encased within eight coils of a superconducting toroid magnet, while the end-cap disks are positioned outside these coils. This configuration allows the spectrometer to achieve a resolution of 10% for particles with a transverse momentum of 1 TeV.

5.2.4 Trigger and Data Acquisition

Every collision is not recorded, only the ones that are deemed “interesting”. This is because most collisions are very forward, elastic collisions, where the protons collide, without converting energy to mass. Recording the “interesting” collisions requires a triggering system, which quickly determines if an event is worth saving, or not. Once ATLAS detects the parti-

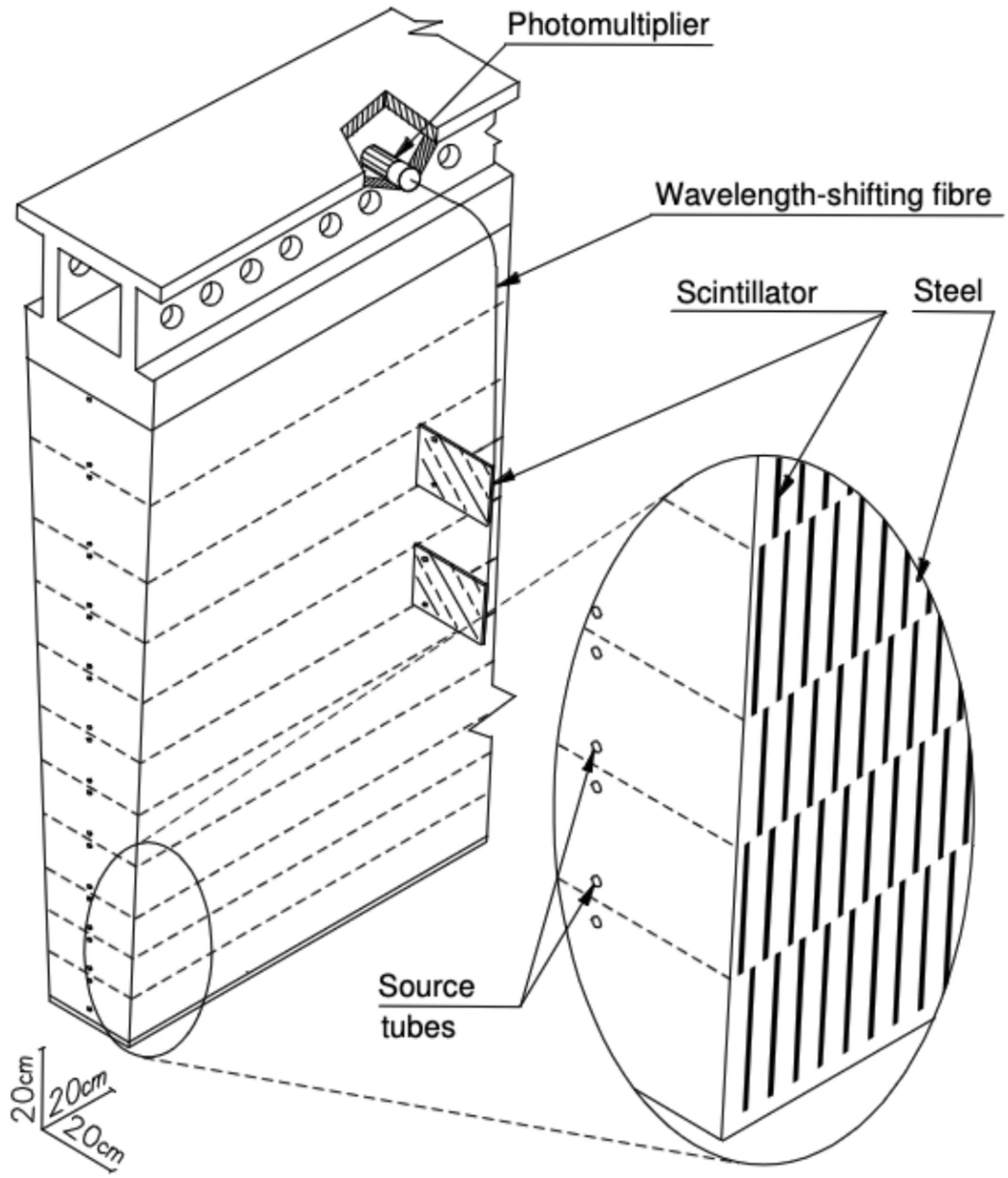

Figure 16: Schematic of the Tile Barrel Calorimeter, showing the absorber and sampling layers, the wavelength-shifting fiber, and the photomultiplier tube [2].

cles, the trigger and data acquisition (TDAQ) system processes the signals. The trigger is a two-level process that filters events based on information from each subsystem. The Level-1 (L1) trigger selects an event by evaluating data from the calorimeters and muon spectrometer. The L1 Calorimeter Trigger (L1Calo) identifies events with significant total transverse

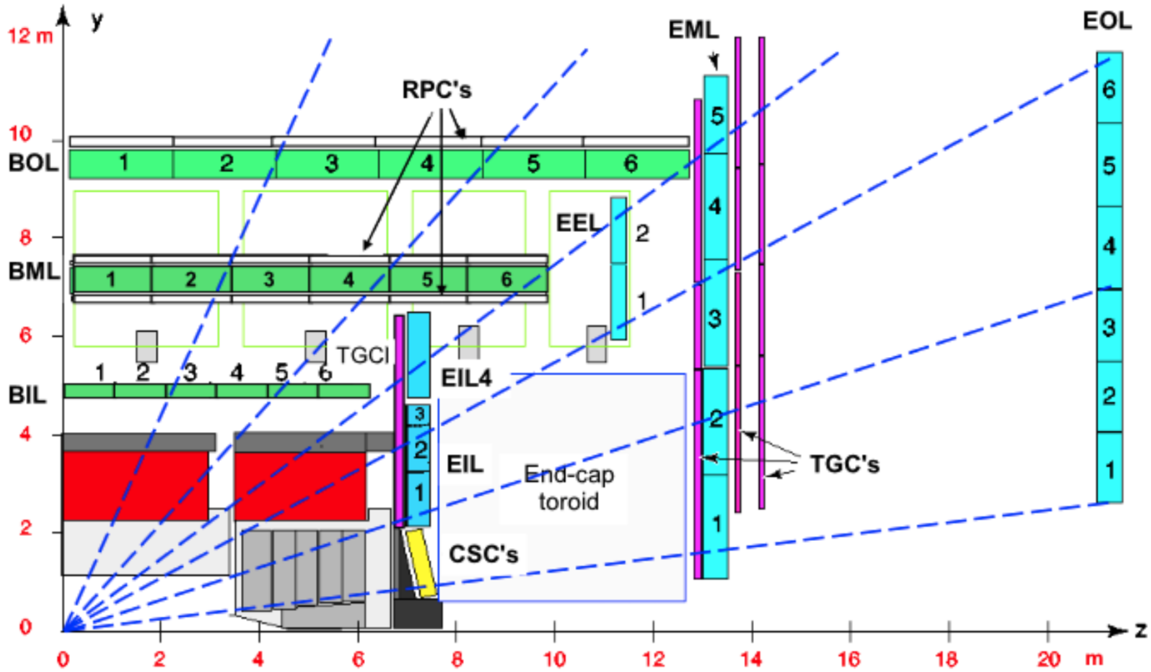

Figure 17: Cross-sectional schematic of the Muon Spectrometer, highlighting the barrel region in green and the end-cap disks in light blue.

energy or events featuring high transverse energy in an electron, photon, jet, hadronically decaying τ-lepton, or large missing transverse momentum (E_T^{miss}). The L1 muon trigger seeks muons meeting certain transverse momentum thresholds. The maximum event rate for the L1 trigger is 75 kHz.

The second stage is the High-Level Trigger (HLT), combining a Level-2 trigger and an event filter. The Level-2 (L2) trigger refines the selection by incorporating coordinates, energy, and types of signatures to limit the data transferred from the detector, reducing the event rate to 3.5 kHz. The event filter, employing fully reconstructed events and offline analysis procedures, further decreases the event rate to approximately 2 kHz. Events passing the HLT are then transferred to permanent storage by the DAQ system.

CHAPTER VI

EXPERIMENTAL METHODS

There are two main types of analyses for experimental high energy physicists; measurements and searches. The subsequent chapters propose two searches for the same type of VLQ, so this section will outline the general steps and methods that are used to determine if the universe is best described by the SM or a BSM theory that include this new exotic particle.

Focusing on particle searches, there is a singular concept that guides the work: find a region in phase space that is rich in signal, prepare the best SM theory prediction for that space, then compare it with the data that is available from the detector. The remaining sections in this chapter serve as a guide through this processes in general, preparing the way for the details to be stated in the analysis chapters ahead. Typically, the material presented in this chapter would be integrated directly within the analysis section. However, given that two similar analyses are proposed in this study, to avoid repetition, the information is consolidated here for clarity and coherence.

6.1 Monte Carlo Background Estimation

The Monte Carlo (MC) method, named after the famous Monte Carlo Casino due to its foundational reliance on randomness and probabilistic outcomes, emerged as a significant computational algorithm in the 1940s. In the realm of particle physics and quantum systems, the intrinsic stochastic nature of quantum mechanics makes the Monte Carlo method particularly valuable. Quantum mechanics is fundamentally probabilistic, exemplified by uncertainties in particle positions and momenta, and this uncertainty resonates well with the random sampling approach integral to Monte Carlo simulations. These simulations adequately model the complex, often non-linear interactions characteristic of quantum systems by randomly sampling possible states and paths of particles. This approach is not just about modeling, it's pivotal for statistical analysis too. These estimations are derived from simulating a large number of events and analyzing the distribution of outcomes. Moreover, the method is instrumental in quantifying uncertainties in quantum physics experiments, which can stem from both the inherent randomness of quantum processes and practical limitations of experimental setups. The Monte Carlo method, with its unique ability to provide a spectrum of possible outcomes rather than a singular deterministic result, thus stands as an indispensable tool in the study and analysis of quantum systems in particle physics.

6.1.1 Background Processes

In experimental particle physics, a background process is an event that "mimics" the signal at the detector level. This means that the background process produces similar readings or data in the detectors as the actual signal of interest, making it challenging (or impossible) to distinguish between the true signal and these unwanted events. Background processes can arise from various sources and are a fundamental consideration in the design and interpretation of experiments in particle physics. For example, refer to Figure 18.

The decay of the SM t quark happens in 5×10^{-25} seconds. Even at light speed, this means the once the quark is made via an inelastic collision in the detector, it travels less than 1.5×10^{-7} nanometers. The first detection site in the ATLAS detector is the pixel detector, 5 centimeters from the collision site. This means that as far as the detector is concerned, it knows nothing about where the decay particles came from. This is the physicists job as will be explained in later sections.

This is an example of using MC to predict the contribution of similar detector level particles. In the most simple sense; if we predict that the SM t decay is the only background,

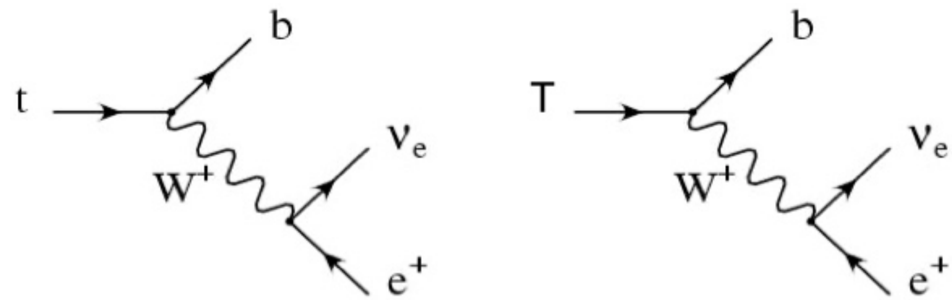

Figure 18: The tree level Feynman diagram for SM t quark BSM T quark decay [6].

and it should produce 50 ± 9 events, we would consider the BSM affirmed if we counted 90 events (a 5σ deviation).

6.1.2 Constructing the MC

There are several steps involved in producing events that are usable in a physics analysis. This is a high level picture of the process, more technical details are found in the referenced appendices.

Theoretical Framework and Initial Probabilities

The process begins with a theoretical framework, which in the case of Proton-Proton collisions at the LHC, is based on the Standard Model of particle physics. The initial probabilities for various processes are calculated to a high order, specifically through the computation of Proton-Proton (*pp*) matrix elements. These calculations involve complex perturbative techniques in QCD and electroweak theory. To best imagine the *pp* matrix element, think of all the possibilities that a *pp* collision could yield. Each of these outcomes have a specific probability, which the MC will use to weight the randomness of the events generated. Of course, the outcomes are then separated again by momentum distribution, which ultimately rests as an attribute to the individual event itself (after reconstruction).

The only exception to this process would be when considering signal MC events that comes from the BSM theory. This would be considered an artificial *pp* matrix element, because it is not proven.

Event Generation

Using the calculated probabilities, Monte Carlo event generators like PYTHIA, HERWIG, or POWHEG [41] are employed to simulate the outcomes of particle collisions. These event generators use the matrix elements to simulate the hard scattering processes, followed by parton showers, hadronization, and the decay of unstable particles (see appendix L) [82].

Detector Simulation

Once the events are generated, the next step is to simulate how these events would interact with the ATLAS detector. This involves a detailed model of the detector in a software framework like GEANT4 [4], which simulates the passage of particles through matter. The simulation accounts for various detector components, including the inner tracking system, calorimeters, and muon spectrometer, and how they respond to different types of particles [4, 84].

Reconstruction of Physics Objects

After simulating the detector response, the next phase is the reconstruction of physics objects. This step requires taking what the detector "sees" (see figure 19) and turning the picture into physics objects such as electron, photons, etc. This involves algorithms that interpret the simulated detector signals to reconstruct the trajectories (tracks) of charged particles, identify jets from quark and gluon fragmentation, measure the energy and momentum of particles in calorimeters, and identify other particles. The reconstruction algorithms are designed to mimic the actual data analysis processes used in ATLAS. Listed here are the basics for physics object reconstruction; the process is identical to the reconstruction of data events, however, for MC samples, the truth information is known. See the in depth reconstruction process in appendix M [84].

- **Track Reconstruction:** The inner detector's response is used to reconstruct the paths of charged particles.
- **Calorimetry:** Energy deposits in the calorimeters are analyzed to measure the energy of particles like electrons, photons, and hadrons.
- **Muon System:** The response in the muon spectrometer is used to identify and measure muons.

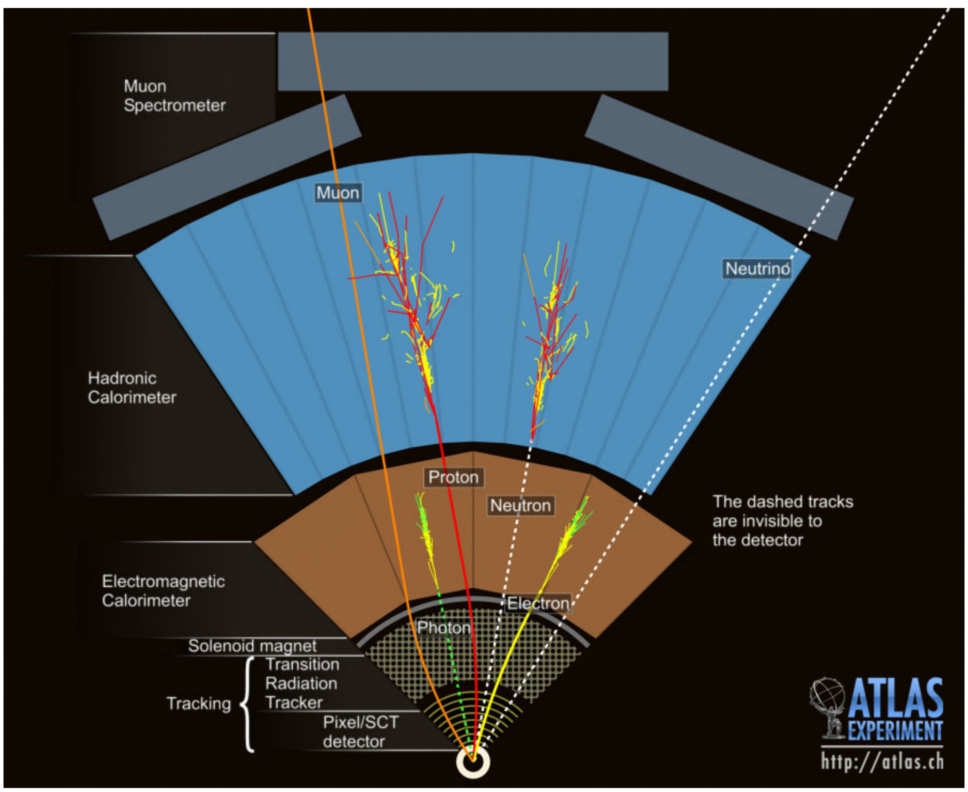

Figure 19: A snapshot of one event, from the perspective of the detector. At this level, the event is nothing more than binary information and requires analysis to determine the physical objects/processes that are present/took place.

Calibration and Validation

An essential part of Monte Carlo simulation is calibration and validation against real data. This ensures that the simulations accurately reflect the behavior of the ATLAS detector. The simulation includes adjustments for known inefficiencies and resolutions of the detector components [84]. One of the best ways to ensure this virtual detector is calibrated, is to use one of the many processes we know very well, called a "standard candle". For instance, we are very familiar with the $z \to ee$ decay, this decay has been measured very accurately and can calibrate the simulator response to this with a high level of precision.

Handling Systematic Uncertainties

Systematic uncertainties in the Monte Carlo simulations, arising from both the theoretical calculations and the detector modeling, are rigorously evaluated. This includes uncertainties in the parton distribution functions (PDF), scale uncertainties in QCD calculations, and uncertainties in the modeling of the detector response (see appendix L).

6.2 Analysis

Generally, a physics search can be summed up as trying to find a needle in a needle stack. The detector can find many events that match what the BSM particle would decay into, and they all look nearly identical. This is why it is important to use clever ways to enhance the signal/background ratio. It makes the analyses much more sensitive when considering the next step, which is predicting the number of events and then looking for an excess. One of the most important methods is to consider what's known as "phase space", and exploit the corners of it that best benefit the search.

6.2.1 Phase Space

The concept of phase space is essential for describing the state of a system of particles. This mathematical framework represents all possible states of a system, with each state corresponding to a unique point in the phase space. Classically, for a single particle, phase space consists of its position and momentum coordinates. However, in high energy particle physics, we often deal with multiple particles with a multitude of attributes, and this leads to a significant increase in the dimensionality of phase space. For instance, a system of N particles in three-dimensional space would have a $6N$-dimensional phase space, accounting for each particle's position and momentum.

Phase space is particularly crucial in analyzing and predicting the outcomes of high-energy particle collisions, as conducted in particle accelerators like the LHC. It allows physicists to calculate the probabilities of various possible outcomes of a collision. Additionally, Feynman diagrams, which are graphical representations of particle interactions, are intimately linked to phase space calculations. These diagrams facilitate the visualization of scattering processes and the exchange of energy and momentum among particles.

The multidimensional nature of phase space becomes a powerful tool for understanding complex systems involving many particles. Each additional particle adds more dimensions, increasing the complexity of the analysis. Due to its high dimensionality, visualization and computation in these spaces require advanced mathematical techniques and computational methods. Overall, phase space is a fundamental concept for understanding the dynamics of particle interactions and plays a vital role in both theoretical and experimental aspects of particle physics.

6.2.2 Discriminating Variable

The next step in optimizing an analysis is to choose an appropriate discriminating variable. In general, a discriminating variable, also known as a *predictor* or *independent variable*, is a variable used to differentiate between groups or categories within a dataset. Its primary purpose is to distinguish, classify, or predict outcomes based on certain characteristics or features. This concept is extensively utilized in particle physics searches.

6.2.3 Characteristics of Discriminating Variables

1. **Differentiation**: A discriminating variable aids in differentiating between various groups or categories. For example, the mass of the reconstructed particle would be a good variable to tell the difference between a SM t quark and BSM T quark, because one weighs in at 173 GeV, while the other is at least 1000 GeV.

2. **Classification and Prediction**: In statistical models, discriminating variables are employed to classify subjects into different groups or to predict outcomes.

3. **Independence**: Typically considered independent variables in a statistical model, they are the inputs or predictors that explain, predict, or affect the dependent variable.

6.2.4 Event Selection

Optimizing the signal sensitivity is a critical task in high energy particle physics, involving the careful selection of a subset of events. This optimization starts with a detailed understanding of the characteristics of both signal and background, focusing on aspects such as energy, momentum, and decay patterns of particles. Such analysis is instrumental in differentiating signal events from background noise. Based on this knowledge, specific event selection criteria, or "cuts," are implemented. These criteria are designed to retain events more likely to be signal and discard those resembling background. Common approaches include setting energy thresholds, applying kinematic constraints to particle trajectories, and utilizing detector information for particle identification.

Refinement is further achieved through Multivariate Analysis (MVA), where multiple variables are simultaneously considered to distinguish signal from background. Techniques such as neural networks, decision trees, or support vector machines are employed to classify events based on complex data patterns. Importantly, these selection criteria are dynamic and require constant optimization, often utilizing MC simulations to assess how adjustments affect signal and background efficiencies. The overarching goal is to maximize signal detection while minimizing background interference.

This process is inherently iterative, necessitating frequent adjustments and re-evaluations of selection criteria by the analysis team. It's also crucial to account for systematic uncertainties in both signal and background estimations, which may arise from factors like detector performance and theoretical model assumptions.

Control Regions (CRs)

During the development phase of the background estimation, the LHC data in the signal regions (SRs) are kept "blinded" from the analysis team. While enhancing the signal-to-background ratio is essential, it is particularly relevant in the SRs, which are ultimately utilized to set limits on the existence of BSM particles. Early analysis stages aim to refine the MC to provide the most accurate estimate of SM background processes for the SRs. An example includes selecting events rich in SM $t\bar{t}$ decay while excluding VLQs, thereby allowing for precise normalization of the $t\bar{t}$ background estimation. Various CRs are established as needed to support this process.

Validation Regions (VRs)

Validation regions are employed to assess the accuracy of systematic adjustments from CR fits in the data phase space adjacent to the defined SRs. This serves as a health check before proceeding to unblind the SRs. If the fit, considering CRs, sets the nuisance parameters (NPs) to certain values that do not transfer effectively to the VRs, analysts must address this issue. It's presumed that similar discrepancies would occur in the SRs.

Signal Regions (SRs)

The SRs are optimized to achieve the highest possible signal sensitivity, ultimately determining the analysis's outcome. Once it is confirmed that the background prediction is accurate and transfers effectively to VRs, the SRs are "unblinded." This means comparing background templates to actual data in the SRs. Fitting software is then used to evaluate the strength of each hypothesis. Ideally, the fit will either strongly favor the null hypothesis (indicating a close match with SM background processes) or prefer the signal-plus-background model (validating the new theory). Ambiguous results, where the data neither support the null hypothesis nor the new theory, could indicate inaccurate background modeling in the SRs, as further discussed in appendix O.

6.2.5 Uncertainties

Statistical Uncertainties

In particle physics, many experiments are *counting experiments*, where the number of events observed in a certain category (such as particle collisions resulting in specific outcomes) is counted. The statistical uncertainty in these experiments can be modeled using a Poisson distribution [56].

The Poisson distribution is a discrete probability distribution that expresses the probability of a given number of events occurring in a fixed interval of time or space, if these events occur with a known constant mean rate and independently of the time since the last event. The probability mass function of the Poisson distribution is given by:

$$P(k;\lambda) = \frac{\lambda^k e^{-\lambda}}{k!} \tag{6.2.1}$$

where k is the observed number of events, λ is the average predicted number of events, and e is Euler's number (≈ 2.71828) [60].

For a Poisson distribution, the mean and the variance are both equal to λ. This is a unique property of the Poisson distribution. Therefore, if we observe n events, the best estimate of λ is n itself. The standard deviation, which is the square root of the variance, is:

$$\sigma = \sqrt{\lambda} = \sqrt{n} \tag{6.2.2}$$

In a particle physics experiment, if n events are observed, the uncertainty in the number of events (due to statistical fluctuation) is given by the standard deviation $\sigma = \sqrt{n}$. This represents the uncertainty inherent in any counting process due to the discrete and random nature of the events. This is exceedingly important when considering that after all the cuts, slimming and trimming is done, the analysis may be left with less than 100 signal and background events in singular bins. With this being the case, the statistical uncertainty is often the limiting factor when determing the "limits", which will be discussed shortly.

Systematic Uncertainties

Systematic uncertainties in a particle physics search account for possible errors that could arise from the methodology and instruments used in an experiment rather than statistical fluctuations. These uncertainties can significantly affect the accuracy and reliability of experimental results. Understanding and quantifying them is crucial for drawing valid conclusions from the data. Here are the key types of systematic uncertainties typically encountered in a particle physics search:

1. **Detector Response and Calibration:**
    - Energy/Momentum Scale and Resolution: Uncertainties in the measurement of energy or momentum of particles due to the calibration of detectors.
    - Position Resolution: Errors in determining the position of particle interactions or decays inside the detector.

- Detector Efficiency: Variability in the detector's ability to register particles or events.

2. **Background Estimation:**

   - Modeling of Background Processes: Inaccuracies in the theoretical models used to estimate background events.
   - Control Regions and Sidebands: Uncertainties associated with the selection of control regions or sidebands.

3. **Signal Modeling:**

   - Theoretical Uncertainties: These arise from limitations in the theoretical models used to predict the signal.
   - Monte Carlo Simulation Uncertainties: Errors in the simulation of the signal process.

4. **Luminosity Measurement:**

   - Integrated Luminosity Uncertainty: Errors in the measurement of the total amount of data collected.

5. **Pile-Up Effects:**

   - Multiple Interactions: Uncertainties due to simultaneous multiple particle collisions.

6. **Particle Identification and Reconstruction:**

   - Efficiency and Misidentification Rates: Uncertainties in the identification of particles and in reconstructing their trajectories.

7. **Trigger System:**

- Trigger Efficiency: Variability in the trigger system's efficiency.

8. **Methodological Uncertainties:**

   - Selection Cuts: Uncertainties related to the criteria used to select or reject events.
   - Statistical Methods: Uncertainties in the statistical methods used for data analysis.

9. **External Inputs:**

   - Dependence on External Measurements: Uncertainties arising from reliance on external measurements or parameters.

Each of these uncertainties needs to be carefully evaluated and quantified to understand their impact on the final results. The total systematic uncertainty is often combined with statistical uncertainties (arising from the finite size of the data sample) to provide a complete picture of the experiment's precision and accuracy.

6.2.6 Profile Likelihood Fit

A profile likelihood fit is a statistical method employed in experimental data analysis, notably in particle physics. The likelihood of a model quantifies how well it explains the observed data, calculated by the probability of observing the data given the model parameters. Fitting a model involves adjusting these parameters to maximize the likelihood. In a profile likelihood, the focus is on a parameter of interest (like the mass of a new particle), while other parameters, termed nuisance parameters (such as background noise or instrument calibration), are adjusted to their most likely values for each value of the parameter of interest. This approach is crucial in particle physics, where experiments, like those at the LHC, produce complex data with many variables. It aids in isolating the parameters of interest, like mass and decay rates of new particles, while accounting for background variables, thereby enhancing the robustness of conclusions about potential discoveries. In Figure 20, it is seen that the nominal values of all the scale factors (SF's) and nuisance parameters is predicting the phase space profile relatively well, given the complexity of the task. However, varying the NP's and the SF's can improve this prediction greatly as seen in the post fit results of the same region, Figure 21.

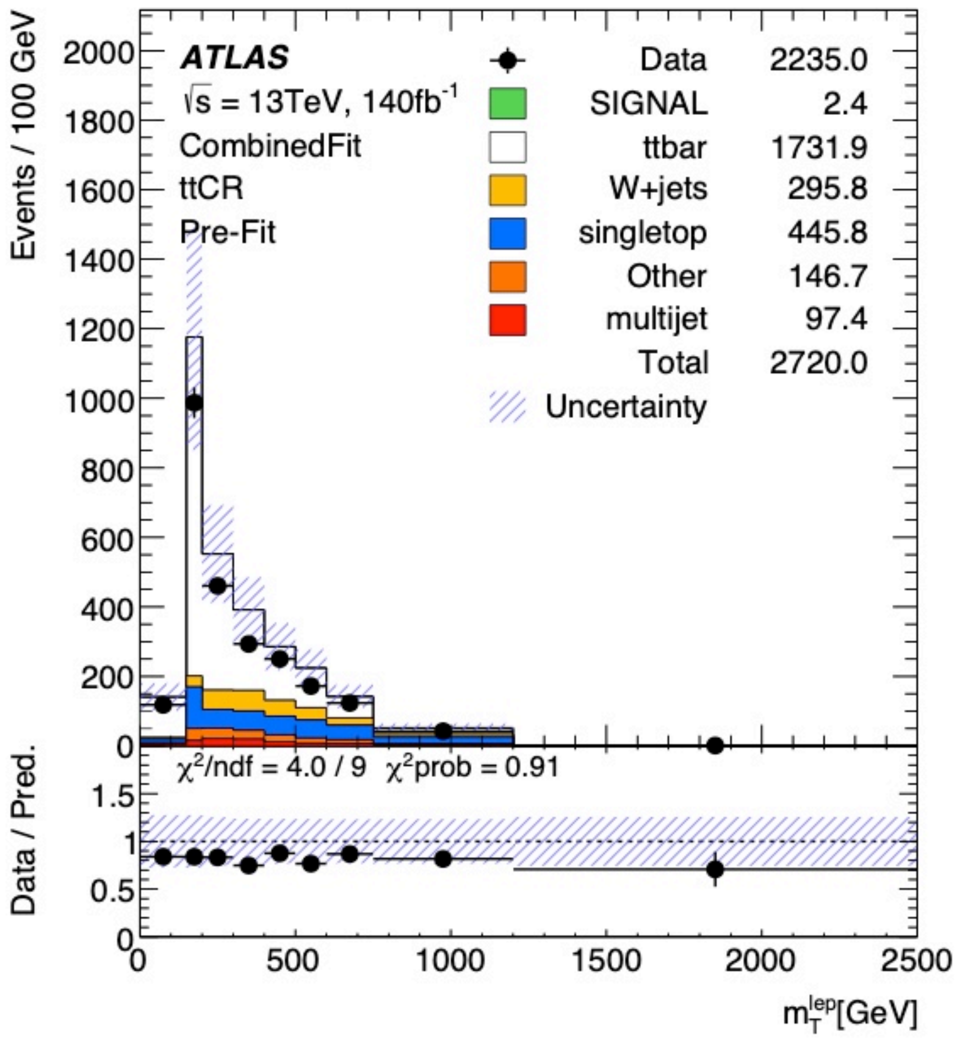

Figure 20: A sample control region pre-fit

Parameter of Interest

In the context of a likelihood fit, a parameter of interest (POI) is a specific variable within a statistical model that researchers aim to estimate or test. This contrasts with nuisance parameters, which are also part of the model but are not of primary interest. The parameter

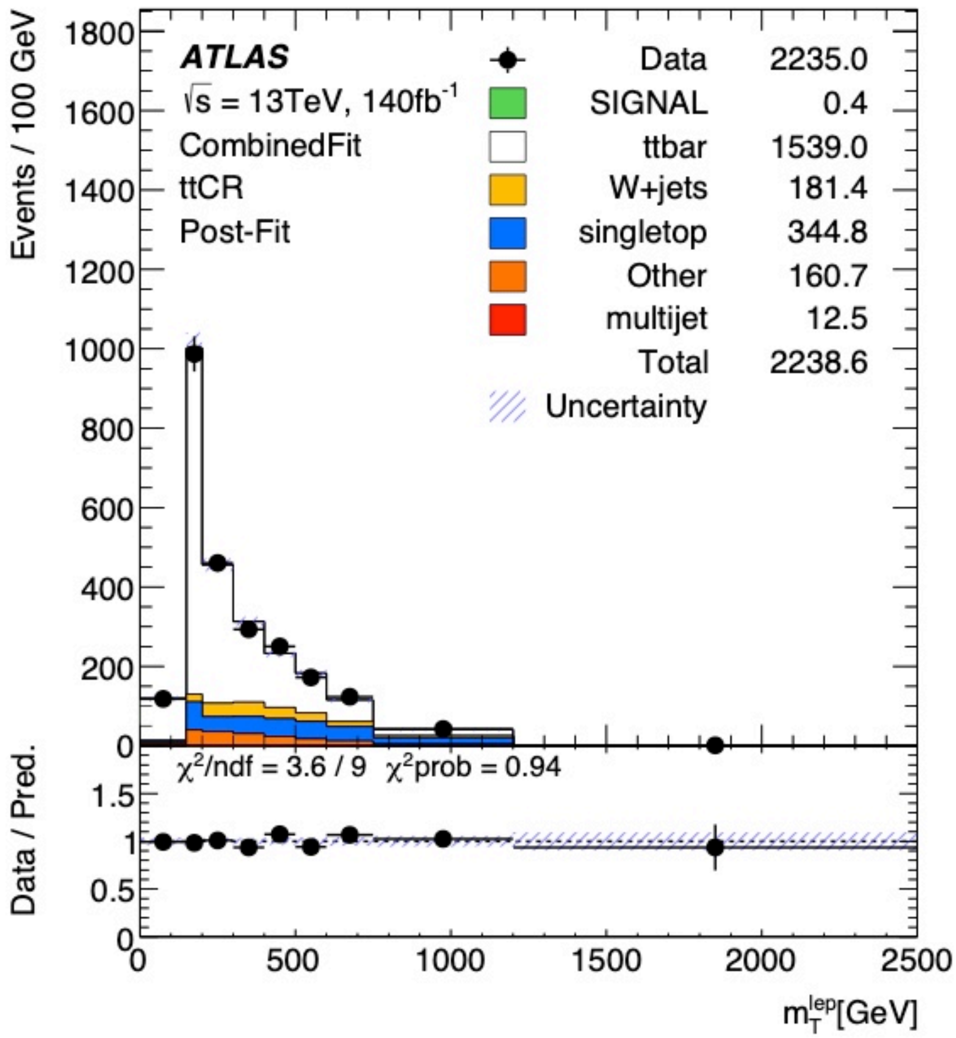

Figure 21: A sample control region post-fit

of interest is central for several reasons. Firstly, it is often directly related to the scientific question being investigated, such as the mass of a new particle, or cross-section for a BSM process. Secondly, the precision and accuracy with which this parameter is estimated are crucial for the validity of the study's conclusions. In likelihood fits, the focus is on finding the value of the parameter of interest that maximizes the likelihood function, indicating the most probable value given the observed data. Moreover, confidence intervals and hypothesis tests are typically constructed around this parameter, helping in understanding its uncertainty and statistical significance. Accurately estimating the parameter of interest is crucial for the success of statistical analysis in empirical research.

Log Likelihood Ratio (LLR)

The range of a log-likelihood ratio (LLR), particularly in statistical hypothesis testing, varies based on the hypotheses being compared. The LLR is defined as the logarithm of the ratio of likelihoods under two hypotheses: the null hypothesis (H_0) and an alternative hypothesis (H_1), given by:

$$\mathrm{LLR} = \log\left(\frac{L(H_1)}{L(H_0)}\right) \tag{6.2.3}$$

where $L(H)$ denotes the likelihood under hypothesis H.

The LLR values can be positive, indicating that H_1 provides a better fit; negative, suggesting a better fit under H_0; or around zero if both hypotheses explain the data equally well. There are no fixed upper or lower bounds for the LLR, with the range determined by the comparative fit of the two hypotheses to the data.

In hypothesis testing, the LLR assesses the strength of evidence against the null hypothesis. A large positive LLR value for the observed data suggests strong evidence favoring H_1, while a significant negative value supports H_0. Statistical significance of the LLR is often evaluated using a χ^2 distribution, particularly in large samples, as per Wilks' theorem [56]. The degrees of freedom for this distribution depend on the number of parameters differing between the models [89].

Now to make the connection between the POI and the LLR, the POI is typically the signal strength (or the cross section/total integral) of the signal sample. Basically a SF that the fit is allowed to move around freely. Looking at Figure 22, the movement of the signal strength parameter would move the H_1 hypothesis closer or further from the null hypothesis. This behavior is easy to understand when you think about varying the integral of the signal sample. This action would make the signal more or less obvious compared to the background noise in the region.

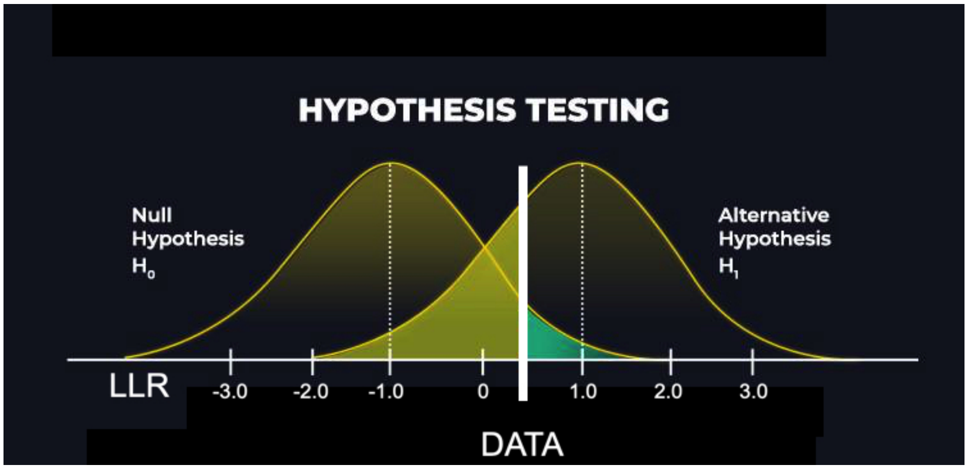

Figure 22: A graphic to aid in the explaination of hypothesis testing. See text for details on the components.

Confidence Level

Referring back to Figure 22, the H_0 distribution in LLR is what would be observed if the universe matched the SM background model, only varying uncertainties of the experiment. Similarly, the H_1 distribution represents what we expect to observe in data considering the unniverse matching the signal plus background (S+B) model. Finally, the solid white "DATA" line is the LLR that is calculated when comparing real data in the CR's and SR's with the MC.

The significance level (α) for the null hypothesis (H_0) is represented by the green shaded region. This value represents the probability of the test statistic (in this case, the LLR) being equal to or more extreme than the value observed in the data, under the assumption that H_0 is true. Similarly, the yellow shaded region represents the probability of the LLR being as extreme or more extreme than the observed value under the alternative hypothesis (H_1).

Most particle searches exclude potential new findings at a 95% $\mathrm{CL_{S+B}}$, which corresponds to a significance level of 0.05. Considering the last example, and figure 22, this would represent the yellow shaded region.

To note, this does not imply that there is a 95% probability that the observed data can be explained by the Standard Model (SM), or the null hypothesis H_0. Instead, it means that if the H_1 hypothesis is true, there is a 5% chance that the observed data is truly explained by the H_1 hypothesis. This range is determined by the confidence interval associated with the 95% $\mathrm{CL_{S+B}}$.

Mathematically, if μ represents a parameter of interest (e.g., a particle's mass or decay rate according to the SM), and confidence interval (CI) represents the interval calculated from the data, then the 95% $\mathrm{CL_{S+B}}$ can be expressed as:

$$P(\mu \in CI | H_1 \text{ is true}) = 0.05 \tag{6.2.4}$$

This equation states that there's a 5% probability that the confidence interval (CI) contains the true parameter μ, given that the H_1 hypothesis is true. It's important to note that this is a statement about the statistical performance of the confidence interval method, not about the probability of H_0 or H_1 being true in any specific experiment.

Furthermore, when an anomoly shows up as indicated by a deviation of three or more standard deviations (3σ) from the null hypothesis, the criteria for acceptance become more stringent. A deviation of 3σ is considered as evidence, 4σ as strong evidence, and 5σ as a discovery. The 5σ level, corresponding to a P_0-value of approximately 1 in 3.5 million, or 99.99995%, indicates an extremely low probability of the result occurring by random chance under H_0.

Limits

The limit plot produced by the analysis is useful in identifying μ value that corresponds with the previously stated 5% $\mathrm{CL_{S+B}}$. This can be rather complicated, so first the components of the plot should be explained, refer to Figure 23.

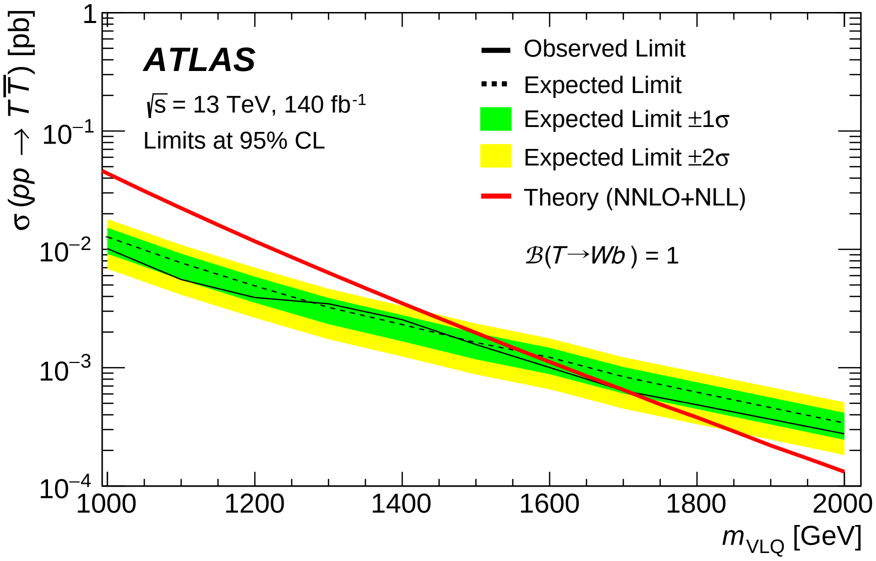

Figure 23: A sample limit plot that would be produced at the end of an analysis, describing the results. See text for details.

1. **Ordinate:** The POI or μ, see appendix O. In this specific case, the cross section of the decaying particle. In the analysis, the signal strength is defined as the percentage of signal with respect to the predicted theory at a given mass point. This is directly propotional to the cross section σ.

2. **Abscissa:** The scanned variable. For this plot, it is the mass of the decaying particle, since the theory cannot predict what the expected coupling to the Higgs field will be. This requires a scan of the masses. This does not have to be the descriminating variable, as in this case.

3. **Solid Red Line:** Theoretical prediction: This represents the theoretical cross section of the particle, as a function of it's mass.

4. **Dashed Black Line:** Expected Limit. This corresponds to a μ value that would produce a CL of 95% if the data was exactly the same as the mean of the H_0 distribution as defined in Figure 22. When we use this kind of data (that matches the SM nominal exactly) it's named Asimov data.

5. **Green and Yellow Regions:** 1 and 2 σ uncertainty bands. These values correspond to μ values when the "data" results an LLR that matches a P_0 value of 1 or 2 σ respectively.

6. **Solid Black Line:** Observed Limit. This is the μ value when real data is used.

7. **Intersection of Solid Black and Red Lines:** Maximum Exclusion Limit. This is the highest value that the scanned variable can be before the analysis loses sensitivity to the signal. Again, in this case, is the mass of the particle. It would be stated in the analysis that the maximum excluded mass limit for this particle is XXX GeV.

The mass exclusion limit stands as a pivotal outcome of the analysis, providing insights into the detectability of the particle in question. This limit essentially delineates the threshold below which the particle, if it existed, would have likely been detected by the analysis. The term 'detected' is used in a nuanced sense, considering the multitude of statistical factors involved, as previously discussed. This threshold is not just a simple observational boundary; it represents a complex interplay of theoretical predictions, experimental capabilities, and statistical interpretations, all of which contribute to understanding the limits of our current search for new particles.

The next chapters examine two specific analyses that explore the details and specific instances of these methods.

CHAPTER VII

Wb+X

Now we begin the exploration of the production of vector-like quarks that subsequently decay into a W-boson and a b-quark in the leptonic channel. We leverage the knowledge gained from previous chapters to devise a strategy for our analysis, aiming to ascertain the existence of any events potentially stemming from the decay of these VLQs.

7.1 Data and MC Samples

The dataset under consideration was obtained from pp collisions at a center-of-mass energy of $\sqrt{s} = 13$ TeV. This dataset, acquired via the ATLAS detector from 2015 to 2018, corresponds to an integrated luminosity of 140 fb^{-1} [43]. Selection of events was primarily based on single-electron and single-muon triggers, with minimum p_T thresholds varying between 20 and 26 GeV, influenced by the lepton type and the specific period of data collection. Furthermore, a trigger focused on events exhibiting significant missing transverse momentum ($E_{\mathrm{T}}^{\mathrm{miss}}$) was employed, having thresholds set at 70, 90, or 110 GeV, contingent on the period of data acquisition. Operational status and adherence to data quality standards of all detector subsystems were mandatory during the data collection phase.

For modeling both signal events and SM background events that included at least one prompt lepton, MC simulations were utilized. The estimation of contributions from processes that passed selection criteria due to either non-prompt leptons or hadronic jets misidentified as leptons (primarily from QCD multijet events) was achieved through a data-driven approach, with MC simulations providing validation. These samples were generated using the

ATLAS simulation infrastructure and GEANT4 [4]. For certain systematic uncertainties, a rapid detector simulation was employed, utilizing a parameterization of the calorimeter response [8]. Unless explicitly noted, the processes of parton shower, hadronization, and underlying events were simulated using Pythia8.230 [82], configured according to the A14 set of adjustable parameters (A14 "tune") and the NNPDF2.3$_{\mathrm{LO}}$ parton distribution functions (PDFs). Within these simulations, the masses of the t-quark and the SM Higgs boson were set at 172.5 GeV and 125 GeV, respectively. Additional pp interactions per bunch crossing (Pile-up) were represented by superimposing minimum-bias events simulated with Pythia8.186 [82], utilizing the A3 tune [33] and NNPDF2.3$_{\mathrm{LO}}$ PDFs, onto the hard-scattering process. To align the simulation with actual data, the distribution of the average number of interactions per bunch crossing in the simulation was adjusted to match the observed distribution in the data.

7.1.1 Signal Samples

For simulating signal events related to $T\bar{T}$ and $B\bar{B}$ production and decay, the Protos v.2.2 software [5] was employed at the leading-order level. Vector-Like Quark (VLQ) masses were considered from 1000 GeV up to 1800 GeV in increments of 100 GeV, alongside a higher mass scenario of 2000 GeV. These simulations catered to the singlet model, while alternative branching ratios were explored through event reweighting based on differing decay modes. For the doublet model, specific simulations at a VLQ mass of 1.2 TeV were conducted, confirming that kinematic variations attributable to isospin are minimal. Signal cross-section calculations were executed using Top++2.0 [5], incorporating NNLO in QCD and NNLL soft-gluon term resummation.

7.1.2 Standard Model Background Samples

The primary background originates from t-quark pair production ($t\bar{t}$). Significant contributions also come from events featuring a single t-quark (single top) or a W boson with jets

(W+jets). Additionally, events with a Z boson and jets (Z+jets), three or four t-quarks, multi-boson events, and t-quark pairs with a vector boson or a Higgs boson (ttV where $V = W, Z$ and ttH) contribute minimally [34].

$t\bar{t}$ event production is simulated using the Powheg Box v2 generator at NLO QCD accuracy with NNPDF3.0$_{\text{nlo}}$ PDFs and an h_{damp} parameter set to $1.5m_t$, where m_t is the t-quark mass [34]. The h_{damp} parameter, a resummation damping factor, helps control the Powheg matrix elements' (ME) matching to the parton shower, thereby regulating high-p_T radiation against which the $t\bar{t}$ system recoils. The parton shower and hadronization models' impact is assessed by comparing this nominal $t\bar{t}$ sample with an alternative Powheg Box v2 sample interfaced to Herwig7.04, using MMHT2014$_{\text{lo}}$ PDFs and the H7UE tune [34]. Uncertainties in NLO ME to parton shower matching are evaluated by comparing the nominal sample with one simulated using MadGraph5_aMC@NLO 2.6.0. The initial-state radiation (ISR) estimation effect is examined by comparing the nominal sample against one produced with an increased h_{damp} (to $3m_t$) [34] and halved renormalization and factorization scales, using the A14 tune's "Var3cUp" weight. The ISR overestimation effect is assessed by comparing with a sample with doubled scales and the "Var3cDown" A14 tune weight. Finally, the uncertainty in final-state radiation (FSR) modeling is gauged by modifying the renormalization scale for parton shower emissions.

The majority of single top events, specifically the tW production, are modeled using Powheg Box v2 at NLO QCD accuracy with NNPDF3.0$_{\text{nlo}}$ PDFs. The nominal sample employs the diagram removal (DR) method to exclude $t\bar{t}$ production's overlapping Feynman diagrams. An uncertainty due to the overlap removal scheme is estimated by comparing this with a sample using the diagram subtraction (DS) method. The parton shower and hadronization models' influence is evaluated by comparing the nominal sample with a Powheg Box v2 sample interfaced to Herwig7.04 with the H7UE tune and MMHT2014$_{\text{lo}}$ PDFs [34]. Uncertainty in ME to parton shower matching for the tW sample is assessed by comparison with a MadGraph5_aMC@NLO 2.6.2 generated sample using $\mathrm{NNPDF2.3_{nlo}}$ PDFs [34].

Single-top-quark t-channel and s-channel production contributions are simulated using Powheg Box v2 at NLO QCD accuracy with $\mathrm{NNPDF3.0_{nlo}}$ PDFs. The parton shower and hadronization models' impact is evaluated similarly to the tW case. The uncertainty in ME to parton shower matching is assessed by comparison with MadGraph5_aMC@NLO 2.6.2 generated samples using $\mathrm{NNPDF2.3_{nlo}}$ and $\mathrm{NNPDF3.0_{nlo}}$ PDFs for t- and s-channel, respectively [34].

V+jets ($V = W, Z$) production is simulated using Sherpa 2.2.1 at NLO QCD accuracy for up to two partons, and LO accuracy for up to four additional partons, normalized to NNLO predictions. Diboson (VV) events are simulated using Sherpa 2.2.1 or 2.2.2 at NLO accuracy for one additional parton and LO for up to three, incorporating off-shell effects and Higgs boson contributions. The ME calculations are matched with the parton shower using the MEPS@NLO prescription, with virtual QCD corrections by OpenLoops and the $\mathrm{NNPDF3.0_{nlo}}$ PDFs [34].

$t\bar{t}V$ and tWZ events are modeled using MadGraph5_aMC@NLO 2.3.3 at NLO with $\mathrm{NNPDF3.0_{nlo}}$PDFs, interfaced with Pythia8.210 (Pythia 8.211) for $t\bar{t}V$ (tWZ), using the A14 tune and $\mathrm{NNPDF2.3_{nlo}}$ PDFs. The diagram removal scheme is applied to the tWZ sample to address overlap with $t\bar{t}Z$. $t\bar{t}H$ events are simulated using Powheg Box v2 at NLO with $\mathrm{NNPDF3.0_{nlo}}$ PDFs. The production of tZ, three and four t-quark events, and $t\bar{t}WW$ is modeled using MadGraph5_aMC@NLO 2.2.2 interfaced to Pythia 8.186. Rare top processes including $t\bar{t}H$, tWZ, tZ, $ttWW$, and multi-top production are collectively termed as "rare top" processes. Multijet MC samples are simulated using Sherpa 2.1.1, including $2 \to 2$ matrix element calculations and the default Sherpa parton shower based on Catani–Seymour dipole factorization with p_T ordering and CT10 PDFs [34].

In all simulations except those using SHERPA, b- and c-hadron decays are simulated by EVENTGEN 1.6.0. For SHERPA simulations, the default configuration recommended by the SHERPA authors is utilized.

7.2 Object Reconstruction

In the analyzed events, the presence of at least one vertex with a minimum of two associated tracks, each having a transverse momentum (p_T) greater than 500 MeV, is a prerequisite. The primary vertex (PV) is identified as the one among all vertices that possesses the greatest sum of the squares of p_T of its associated tracks, as outlined in [17]. Electron reconstruction is achieved through the matching of ID tracks with clusters in the EM calorimeter, followed by a calibration process. Eligible electron candidates are those located within the central detector region ($|\eta| < 2.47$), exhibiting a p_T exceeding 27 GeV, and associated with a track that adheres to the conditions of $|z_0 \sin\theta| < 0.5$ mm and $|d_0/\sigma_{d_0}| < 5$, where d_0 denotes the track's impact parameter relative to the beam line, σ_{d_0} its uncertainty, and z_0 the closest distance in the z-axis between the track and the beam spot. Electron candidates found within the calorimeter's barrel-end-cap transition region ($1.37 < |\eta| < 1.52$) are excluded. Classification of electrons into "baseline" and "tight" categories is based on their adherence to *medium likelihood* and *tight likelihood* identification criteria respectively. The latter also necessitates meeting specific calorimeter and ID isolation criteria: $E^{\text{isol}}_{\text{T, cone}}/p_{\text{T,e}} < 0.2$ and $p^{\text{isol}}_{\text{T,var}}/p_{\text{T,e}} < 0.15$, with $E^{\text{isol}}_{\text{T,cone}}$ representing the energy deposited within a radius (R) of 0.2 around the candidate, and $p^{\text{isol}}_{\text{T,var}}$ the sum of track p_T excluding the electron candidate within a cone of radius $R = \min(10\ \text{GeV}/p_{\text{T,e}}, 0.2)$. Correction scale factors align data and simulation for reconstruction, identification, isolation, and trigger selection efficiencies.

Muon reconstruction integrates combined track data from the MS and ID, with "baseline muons" meeting the *loose* identification criteria and "tight muons" complying with the *tight* criteria alongside the track-based isolation standards of the *TightTrackOnly* working point. This standard involves the scalar p_T sum of all tracks within a cone of $R =$

$\min(0.3, 10 \text{ GeV}/p_{\mathrm{T},\mu})$ around the muon, excluding the muon's own track, with selection contingent on this sum being below 6% of the muon's p_T. Additional requisites include a $|z_0 \cdot \sin\theta| < 0.5mm$ and $|d_0/\sigma_{d_0}| < 3$. Calibration of muons is conducted, requiring a $p_T > 15$ GeV and an $|\eta| \leq 2.5$. Discrepancies in muon reconstruction, identification, vertex matching, isolation, and trigger efficiencies between simulation and actual data are rectified using efficiency scale factors.

Small-radius (small-R) jet candidates are constructed from particle-flow objects, following the procedures in [17], using the anti-k_t algorithm with a radius parameter of $R = 0.4$ as described in [49]. The jet formation is a composite of track data from the ID and calorimeter energy deposits. A series of corrections, including those based on simulation and in situ calibrations, are applied to calibrate the jet energy to particle level. Jets are accepted if they have $p_T > 25$ GeV and $|\eta| < 2.5$. For jets with $|\eta| < 2.4$ and $p_T < 60$ GeV, originating from Pile-up interactions, adherence to the "tight" jet vertex tagger (JVT) criterion is necessary, as explained in [17]. Identification of small-R jets with b-hadron decays utilizes the DL1r algorithm, a neural network-based method, aiming for an efficiency of 77% and specific mistag rates in simulated $t\bar{t}$ events, as documented in [7]. Adjustments for b-quark tagging efficiencies in simulation and mistag rates for charm and light jets are made to align with data performances.

To avoid ambiguity in object reconstruction, an overlap removal process using baseline lepton definitions is implemented. Initially, electron-muon overlaps are resolved by eliminating muons sharing an ID track with an electron, if calorimeter-tagged, or otherwise the electron. Jets within a $\Delta R = 0.2$ radius of an electron are discarded, followed by the exclusion of any electrons within a $\Delta R = 0.4$ radius of remaining jets. Jets with fewer than three associated tracks within $\Delta R = 0.2$ of a muon are also removed, or alternatively, the muon if it falls within $\Delta R = \min(0.4, 0.04 + 10 \text{ GeV}/p_{\mathrm{T},\mu})$ of a jet.

$E_{\mathrm{T}}^{\mathrm{miss}}$ is defined as the negative vector sum of the transverse momenta of all calibrated event objects, supplemented by a track-based soft-term accounting for unassociated energy deposits linked to the primary vertex, in line with the methodology in reference [17].

Lastly, large-radius (large-R) jets are formed from topological calorimeter-cell clusters, refined through local hadronic cell reweighting as per reference [17], using the anti-k_t algorithm with a radius parameter of $R = 1.0$. A 'trimming' algorithm, detailed in reference [71], is applied to reduce effects of soft radiation. This involves removing constituent small-R jets, reclustered using the k_t algorithm with $R = 0.2$, which have p_T less than 5% of the large-R jet p_T. Large-R jets must satisfy $p_T > 200$ GeV, $|\eta| < 2.0$, and a mass over 50 GeV. Calibration of jet energy scale (JES) and resolution (JER), and mass scale (JMS) and resolution (JMR). A W boson tagging algorithm, efficient at 80%, is employed for identifying high-p_T hadronically decaying W bosons within single large-radius jets applying criteria on the jet mass, associated inner-detector tracks, and the energy correlation function ratio D_2, with corresponding scale factor corrections.

7.3 Event Selection

This analysis focuses on final states characterized by the presence of exactly one electron or muon, $E_{\mathrm{T}}^{\mathrm{miss}}$, and jets. Events are selected through either a single lepton or $E_{\mathrm{T}}^{\mathrm{miss}}$ trigger. For events triggered by a single lepton, the lepton must have $p_T > 27$ GeV and match the triggering object. If triggered by the $E_{\mathrm{T}}^{\mathrm{miss}}$ criterion, events must exhibit $E_{\mathrm{T}}^{\mathrm{miss}} > 200$ GeV, compensating for the decreased efficiency of single muon triggers at higher muon p_T.

The selection criteria mandate precisely one tight muon with $p_T > 27$ GeV or one tight electron with $p_T > 60$ GeV. The higher p_T threshold for electrons of $p_T > 60$ GeV aids in estimating the background from non-prompt electrons. The methodology for fake lepton background estimation hinges on the lower efficiency of fake leptons, which comply with the baseline selection, to meet the stringent tight lepton criteria compared to real leptons. The single electron trigger, integral to both baseline and tight selections, enforces strict criteria on electrons with $p_T < 60$ GeV, thus challenging to tighten further than the baseline criteria. Investigations confirm that this elevation in electron p_T threshold does not detrimentally affect the analysis sensitivity. Events featuring additional leptons with $p_T > 25$ GeV that meet baseline criteria are excluded.

Additionally, all events must exhibit $E_{\mathrm{T}}^{\mathrm{miss}} > 60$ GeV and include at least three small-R jets, with at least one being b-tagged. These stipulations form the preselection criteria. The analysis primarily targets T-quarks heavier than 1.35 TeV, as outlined by the lower mass boundary established in previous work [40]. The significant mass of the T-quark implies that its decay products, particularly the hadronically decaying W boson, will be highly collimated, manifesting as large-R jets. Thus, the presence of at least one W-tagged large-R jet is essential. In scenarios with multiple W-tagged large-R jets, the one whose mass is closest to the W boson mass ($m_W = 80.38$ GeV) is selected to represent the hadronically decaying W boson (W_{had}) for reconstructing the hadronically decaying T-quark candidate. The leptonically decaying W boson (W_{lep}) is reconstructed from the selected lepton and a neutrino, whose p_T is derived from the $E_{\mathrm{T}}^{\mathrm{miss}}$, and p_z calculated assuming the lepton-neutrino system's invariant mass equals the W boson's mass, leading to a quadratic equation. The solution with the lesser absolute p_z value is preferred for real solutions, while for complex solutions, the neutrino's x and y momentum components are adjusted to minimize a χ^2 parameter. This parameter incorporates uncertainties in neutrino and lepton momenta and the W boson mass, requiring the angular distance between the lepton and the reconstructed neutrino to be $\Delta R(\ell, \nu) < 0.7$.

The reconstruction of the two T candidates involves pairing each of the W candidates, W_{lep} and W_{had}, with a small-R jet, prioritizing those combinations that minimize the discrepancy between the reconstructed hadronic and leptonic T masses, denoted as $\Delta m_{\mathrm{VLQ}} \equiv |m_T^{\mathrm{lep}} - m_T^{\mathrm{had}}|$. If an event contains a single b-tagged jet, only combinations including this jet are considered. For events with multiple b-tagged jets, combinations involving the two highest p_T b-tagged jets are selected. The expected separation between the jet paired with W_{had}, termed b_{had}, and the W_{had} itself is significant due to the anticipated low p_T and high mass of signal VLQs, unlike $t\bar{t}$ events where the t-quarks' high p_T results in a smaller separation between the W and b. Thus, a $\Delta R(W_{\text{had}}, b_{\text{had}}) > 1.0$ criterion is applied to diminish $t\bar{t}$ background interference. Accurately reconstructed signal events are anticipated to exhibit small Δm_{VLQ} values, with both reconstructed T-quark masses, m_T^{lep} and m_T^{had}, closely approximating the actual T-quark mass. Conversely, $t\bar{t}$ events will have m_T^{lep} and m_T^{had} values near the t-quark mass, m_t. $T\bar{T}$ events stemming from other decays like $T \to Ht/Zt$ will likely show m_T^{lep} and m_T^{had} values near the T-quark mass but with larger Δm_{VLQ} due to less optimized VLQ reconstruction for t-quarks emanating from T-quark decays. Misreconstruction, detector effects, and final state radiation can further broaden the reconstructed mass peaks for both signal and $t\bar{t}$ events. In contrast, a smooth Δm_{VLQ} distribution is anticipated for background processes such as W+jets and single-top-quark production, utilizing Δm_{VLQ} to delineate regions enriched in single-top-quark background that resemble the signal region's kinematic properties.

The scalar sum S_{T} of the p_T of the selected small-R jets, the lepton p_T, and the $E_{\text{T}}^{\text{miss}}$ serves as a significant discriminant due to the expected substantial mass of the T. Signal regions necessitate $S_{\text{T}} > 1900$ GeV, whereas regions designated for constraining background nuisance parameters and normalizations stipulate $1400 < S_{\text{T}} < 1900$ GeV. The splitting of control and signal regions based on Δm_{VLQ} is depicted in Figure 24. The signal region, defined by $S_{\text{T}} > 1900$ GeV and $\Delta m_{\text{VLQ}} < 500$ GeV, is subdivided into SR1 with $\Delta m_{\text{VLQ}} < 200$ GeV and SR2 spanning $200 < \Delta m_{\text{VLQ}} < 500$ GeV. Region SR1 aims to encapsulate optimally reconstructed VLQ events, anticipated to exhibit narrow peaks in the m_T^{lep} and m_T^{had} distributions. Conversely, region SR2 is expected to include less precisely reconstructed VLQ events, leading to broader mass distributions, yet a substantial fraction of VLQs is predicted to fall within this categorization. A control region, defined by $S_{\text{T}} > 1900$ GeV and $\Delta m_{\text{VLQ}} > 500$ GeV and denoted $S_{\text{T}}^{\text{High}}\Delta m$CR, possesses minimal signal contamination for yet unexcluded signal masses and is predominantly influenced by single top production.

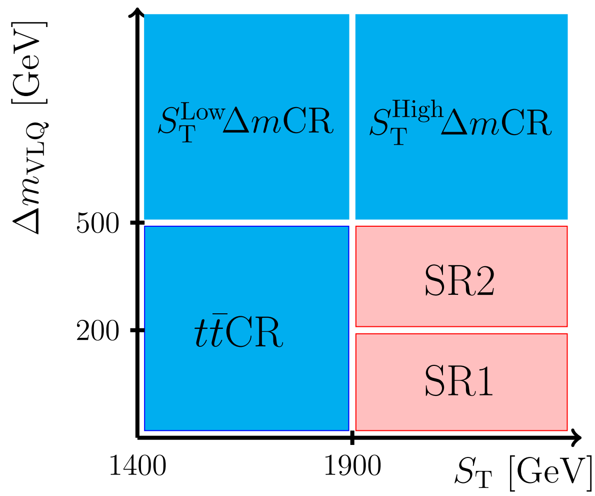

Figure 24: Diagram showing the two-dimensional plane within S_{T} and Δm_{VLQ}, delineating the signal and control regions utilized in the ultimate composite likelihood fitting process [34].

This region offers a means to refine the modeling of the single top background using events with kinematic similarities to the signal region. The interval $1400 < S_{\mathrm{T}} < 1900$ GeV is separated into two control regions based on Δm_{VLQ}: $t\bar{t}$CR with $\Delta m_{\mathrm{VLQ}} < 500$ GeV and $S_{\mathrm{T}}^{\mathrm{Low}}\Delta m$CR with $\Delta m_{\mathrm{VLQ}} > 500$ GeV. The $t\bar{t}$CR is characterized by a high concentration of $t\bar{t}$ events, with a purity nearing 70%, facilitating the adjustment of the normalization and modeling of t-quark pair production. The $S_{\mathrm{T}}^{\mathrm{Low}}\Delta m$CR furnishes an additional venue for refining the single top background, albeit with kinematic characteristics akin to the $t\bar{t}$CR. A comprehensive overview of all regions is encapsulated in Table 1. Regions excluded from the fit, namely W+jetsCR and $t\bar{t}$RWR ($t\bar{t}$ reweighting region), are leveraged to derive data-driven adjustments for the background modeling and are elaborated upon in subsequent sections.

7.4 Background Process Estimation

Contributions from dominant background processes, such as top quark pair ($t\bar{t}$) and W+jets production, are estimated using Monte Carlo (MC) simulations with data-driven corrections derived in control regions predominantly influenced by the respective process. Standard

Table 1: Summary of the signal and control regions employed in the analysis [34].

Selection	SR1 / SR2	$t\bar{t}$CR	$S_{\mathrm{T}}^{\mathrm{Low}}\Delta m$CR / $S_{\mathrm{T}}^{\mathrm{High}}\Delta m$CR	W+jetsCR	$t\bar{t}$RWR
Preselection	✓	✓	✓	✓	✓
$N_{\mathrm{Large}\text{-}R\ \mathrm{Jet}}$	≥ 1	≥ 1	≥ 1	≥ 1	≥ 1
$S_{\mathrm{T}}[GeV]$	>1900	1400–1900	1400–1900 / >1900	900–1900	>800
$N_{W\text{-tag}}$	≥ 1	≥ 1	≥ 1	≥ 1 partially inverted	≥ 1
$N_{b\text{-tag}}$	≥ 1	≥ 1	≥ 1	≥ 1	≥ 2
$\Delta R(W_{\mathrm{had}}, b_{\mathrm{had}})$	> 1.0	> 1.0	> 1.0	–	< 1.0
$\Delta R(\ell, \nu)$	< 0.7	< 0.7	< 0.7	< 1.0	< 1.2
$\Delta m_{\mathrm{VLQ}}[GeV]$	< 200 / 200–500	< 500	> 500	–	–
$m_T^{\mathrm{lep}}, m_T^{\mathrm{had}}[GeV]$	–	–	–	–	< 700
Included in fit	yes / yes	yes	yes / yes	no	no
Goal	Optimise signal sensitivity	Constrain $t\bar{t}$ normalisation	Constrain single top uncertainties	Derive W+jets normalisation factor	Derive $t\bar{t}$ S_{T} shape reweighting

Model (SM) backgrounds featuring a prompt lepton (e.g., single top, Z+jets, diboson) are also estimated through MC simulations. The minor contribution from multijet events is assessed using a data-driven methodology.

7.4.1 W+jets Correction

A correction for W+jets events is obtained in a dedicated control region, denoted as the W Control Region (W+jetsCR). This region is designed to be orthogonal to the signal region, specifically through an inverted jet mass requirement in the hadronic W boson tagging algorithm. The potential biases in W+jets event modeling due to this inversion are analyzed and addressed with a dedicated uncertainty. The W+jetsCR further imposes $900 < S_{\mathrm{T}} < 1900$ GeV to mitigate potential signal contamination. Except for this adjustment, all other selection criteria mirror those of the signal region, as outlined in Table 1.

The requirement of at least one b-tagged jet, akin to the signal region's criteria, ensures the W+jetsCR is significantly influenced by $t\bar{t}$ events. This setup facilitates the validation of the W+jets simulation correction, as the modeling of W+jets events is contingent upon the heavy-flavour tagging [36]. The correction estimate is based on the charge asymmetry observed in W+jets events within the W+jetsCR, stemming from the u- and d-quark content disparity in protons [39]. Defined as $A = N_+ - N_-$, where N_+ and N_- represent the counts of events with positively and negatively charged leptons, respectively, this correction factor is derived by comparing A across data and MC simulations within the W+jetsCR. This method effectively separates the charge-asymmetric W+jets process from potential mis-modeling of the charge-symmetric $t\bar{t}$ process, and is also useful in distinguishing charge-asymmetric events from the charge-symmetric VLQ signal. Contributions from charge-symmetric backgrounds like $t\bar{t}$ and multijet are nullified in A, while minor inputs from other charge-asymmetric sources (e.g., single top, diboson, t-associated production) are adjusted using MC samples. The dependency of the W+jets normalization on S_{T} and W-tagging requirements was scrutinized in the control region sidebands to validate the correction's applicability in the signal domain. The W+jets correction, expressed as a function of S_{T} up to 4 TeV, reveals no significant S_{T}-dependent variation. An extra uncertainty is incorporated to address the discrepancy between normalization corrections observed in the W+jetsCR and those in sidebands with modified W-tag criteria. Furthermore, the normalization's sensitivity to various event and kinematic parameters was evaluated, confirming the absence of notable dependencies. Consequently, a singular normalization factor is applied to the W+jets MC prediction, quantified as $f_{W+\mathrm{jets}} = 0.915 \pm 0.09$ (stat.) $\pm\, 0.54$ (syst.), with major systematic uncertainties stemming from single-top background modeling and the inversion of W-tag selection criteria.

7.4.2 $t\bar{t}$ Correction

The MC simulation's $t\bar{t}$ background estimate is noted to consistently overpredict event counts at elevated t-quark p_T levels [38], adversely affecting the modeling of S_{T}, crucial for signal-background differentiation. A data-driven reweighting is hence applied to $t\bar{t}$ MC events to reconcile the observed discrepancy in the S_{T} distribution between MC predictions and actual data, improving the overall model. The adjustment is derived in the $t\bar{t}$ reweighting region ($t\bar{t}$RWR), as specified in Table 1, characterized by a $t\bar{t}$ purity of 89% and a secondary single-top background contribution of 6%. Distinguishing the $t\bar{t}$RWR from the signal region are criteria such as $\Delta R(W\text{-tag}, b_{\mathrm{had}}) < 1.0$ and $S_{\mathrm{T}} > 800$ GeV, motivated by the reduced angular separation between the W boson and b-quark in high-p_T t-quark decays. To minimize signal event contamination in the $t\bar{t}$RWR, reconstructed VLQ masses, m_T^{lep} and m_T^{had}, are constrained to be less than 700 GeV. Figure 25(a) illustrates the S_{T} distribution within the $t\bar{t}$RWR prior to reweighting implementation.

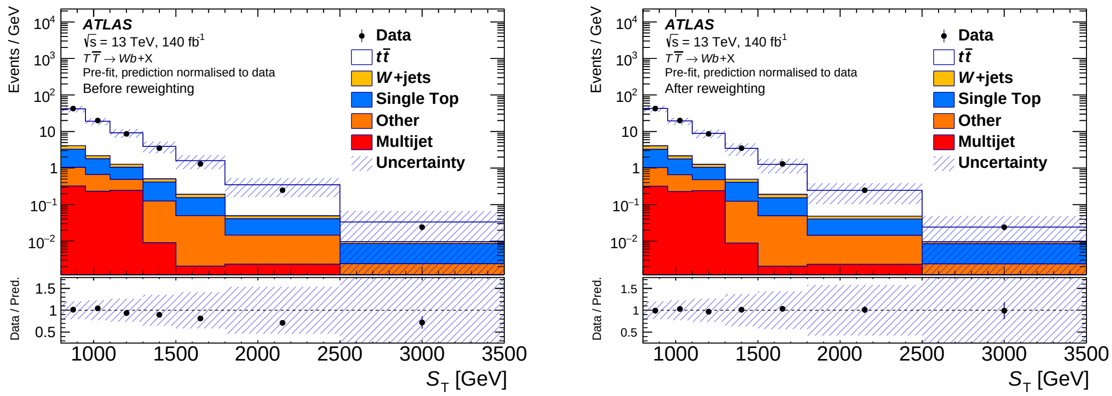

(a) (b)

Figure 25: Plots depicting the distributions of S_{T} for both data (represented by dots) and predictions (shown as histograms in various colors). In (a), the distributions are displayed before applying reweighting, while in (b), they are shown after reweighting (details provided in the text). The prediction is normalized to the data to highlight discrepancies in distribution shape and the impact of S_{T} shape reweighting. Error bars encompass statistical uncertainty, and the shaded band denotes total systematic uncertainty. The last bin incorporates overflow data [34].

The reweighting aims to adjust the S_{T} distribution shape, maintaining the normalization as a free variable in the final likelihood fit, subsequently constrained by the data in the $t\bar{t}$CR. Subtractions of non-$t\bar{t}$ contributions from the data facilitate the calculation of the ratio between the resulting S_{T} distribution and the $t\bar{t}$ prediction. The correction factor is then ascertained through a fit to this ratio using the function:

$$f(S_{\mathrm{T}}) = p_0 \cdot \exp(-p_1 \cdot (S_{\mathrm{T}} - p_2)^2) + p_3, \tag{7.4.1}$$

where p_i (for $i = 0, 1, 2, 3$) represent the fit's free parameters. Alternate functional forms were examined, with the selected equation most accurately depicting the data/MC ratio. This fitting approach proved consistent across various fit intervals and binning strategies.

Given the correlation between S_T and jet multiplicity (N_jets), separate fits were conducted for events with $3 \leq N_\mathrm{jets} \leq 6$ and $N_\mathrm{jets} \geq 7$. Figure 25(b) displays the post-correction S_T distribution in the $t\bar{t}$RWR.

The statistical uncertainty from the fit is propagated as a correction uncertainty, with the single top modeling's impact assessed by altering its contribution by 100% within the $t\bar{t}$RWR. Other process uncertainties exert negligible influence on the correction derivation. The function's offset parameter, p_3, ensures asymptotic behavior towards 0.64 (for $3 \leq N_\mathrm{jets} \leq 6$) and 0.62 (for $N_\mathrm{jets} \geq 7$), at high S_T values, where statistical limitations hinder precise correction scaling. An uncertainty of 58% (for $3 \leq N_\mathrm{jets} \leq 6$) and 38% (for $N_\mathrm{jets} \geq 7$), addressing the statistical ambiguity in the high-S_T extremity, is applied if $S_\mathrm{T} \geq 2.5$ TeV. The S_T correction's efficacy is validated in a dedicated $t\bar{t}$-centric verification region, demonstrating commendable agreement between the adjusted $t\bar{t}$ MC estimate and observational data in all distributions.

7.4.3 Multijet Estimate

Multijet event inclusion in the signal domain arises from either hadronic jets misidentified as leptons or non-prompt leptons emanating from heavy-flavor jets. These processes, collectively termed non-prompt leptons, constitute a minor fraction (5%) of the signal region's events. Estimation of this background leverages a data-driven "Matrix Method" (MM) [42], utilizing lepton categorization into "loose" and "tight" groups for predicting non-prompt lepton counts. "Tight" leptons align with signal criteria, whereas "loose" leptons meet baseline conditions but fail stringent requirements. A "loose region", enriched in non-prompt leptons, is established by substituting the signal region's tight lepton criterion with a loose equivalent. The relationship between events harboring prompt (non-prompt) leptons in the signal and loose regions is governed by their efficiencies to meet tight criteria, termed "real efficiency" ("fake efficiency"). Consequently, determining these efficiencies enables the calculation of the signal region's non-prompt lepton (multijet event) count, as delineated in Ref. [37].

Given the tight lepton criteria's efficacy in minimizing multijet background within signal and control regions, differential distribution shapes estimated via MM are predominantly influenced by statistical fluctuations. Accurate multijet background prediction is crucial for the m_T^{lep} distribution, utilized in the final likelihood fit. Since these background events lack genuine VLQ decays, their reconstructed mass distributions are largely shaped by the selection's kinematic constraints. Consequently, the m_T^{lep} distributions for Z+jets and multijet backgrounds exhibit similarity. Hence, in the fit, the Z+jets prediction models the multijet background's distribution, scaled to the MM-derived total yield. For reconstructed m_T^{lep} values below 200 GeV, the MM's multijet background estimate is sensitive to the subtracted $t\bar{t}$ prediction. An iterative approach is employed for multijet normalization factor determination, initially focusing on reconstructed masses above 200 GeV. Subsequent iterations adjust the $t\bar{t}$ normalization to align Z+jets and multijet predicted yields until the normalization factor's variation falls below 1% across iterations. A comprehensive 100% uncertainty is assigned to the multijet estimate, covering both modeling systematic uncertainties in prompt lepton processes and fake-lepton efficiency. An additional, uncorrelated 100% uncertainty on the distribution shape for reconstructed masses under 200 GeV accommodates the specific sensitivity to $t\bar{t}$ event modeling. For modeling multijet shape across other analytical regions and variables, the MC multijet sample, scaled to the MM estimate, is utilized.

7.5 Systematic Uncertainties

Systematic uncertainties in this analysis are broadly classified into two main categories: experimental uncertainties, which encompass aspects related to detector response modeling and physics object reconstruction, as well as to the estimation of data-driven backgrounds or corrections to simulated backgrounds; and theoretical uncertainties, which pertain to the simulation modeling of physics processes. It is assumed, unless specified otherwise, that uncertainties from a common source are correlated across different processes and analysis regions within the final statistical evaluation. Furthermore, the impact of these uncertainties is subject to constraint by the likelihood fit to the data.

7.5.1 Theory Uncertainties

The most significant systematic uncertainties arise from the modeling of $t\bar{t}$ and single top backgrounds. For $t\bar{t}$ production, theoretical uncertainties include the choice of Monte Carlo (MC) generator, which for this analysis involves NLO accuracy simulations; initial state radiation (ISR), final state radiation (FSR), and parton shower model uncertainties; and the shower matching scheme. Each of these components is assessed by comparing the nominal $t\bar{t}$ prediction against alternative MC samples. Similarly, modeling uncertainties for single top production are evaluated through the examination of alternative samples, focusing on the parton shower choice and the matching between the NLO matrix element and the parton shower. An additional uncertainty related to the $t\bar{t}/Wt$ overlap removal scheme is investigated by contrasting the nominal single top MC generated with the Diagram Removal (DR) scheme against an alternative Diagram Subtraction (DS) scheme [41]. To address the extrapolation of uncertainties from low to high S_{T} regions, this particular uncertainty is bifurcated into components applicable to high-S_{T} ($S_{\mathrm{T}} > 1.9$ TeV) and low-S_{T} ($1.4 < S_{\mathrm{T}} < 1.9$ TeV) domains. Uncertainties in the parton distribution functions (PDF) for both $t\bar{t}$ and single top productions are derived using the `PDF4LHC15` combined set [48]. The influence of QCD scale uncertainties is gauged by varying the renormalisation and factorization scales up and down independently, with the variation imparting the greatest impact on the discriminant (m_T^{lep}) being adopted.

For simplification purposes, all minor backgrounds including $t\bar{t}V$, Z+jets, rare top processes, and diboson production are amalgamated into a single "other" category, to which a uniform normalization uncertainty of 50% is applied. This 50% uncertainty is primarily informed by the relative uncertainty in the Z+jets process, identified as having the largest uncertainty within the "other" category, as determined in a preceding analysis [40].

7.5.2 Experimental Uncertainties

Experimental uncertainties encompass a 0.83% uncertainty in the integrated luminosity for the combined 2015–2018 data period [31], ascertained using the LUCID-2 detector for primary luminosity measurements. Lepton-related uncertainties include potential mis-modeling of electron and muon energy scales and resolutions [21, 11], alongside uncertainties in electron and muon trigger, reconstruction, identification, and isolation efficiency correction factors [24, 21].

Uncertainties associated with small-radius jets encompass those in the jet energy scale (JES), jet energy resolution (JER) [23], and on the jet mass scale (JMS) [22]. Additionally, uncertainties in the jet vertex tagger (JVT) selection efficiency and Pile-up reweighting factors are accounted for. Large-radius jets are subject to JES, JER [22], JMS, and jet mass resolution (JMR) [29] uncertainties. The scale and resolution of the track soft term in the $E_{\mathrm{T}}^{\mathrm{miss}}$ calculation also contribute to systematic uncertainties [15].

For b-tagging, uncertainties include those in b-jet selection efficiency, c-jet and light jet mistag rates, and extrapolation of calibrations to high p_T and from c-jets to τ leptons [20, 30, 32]. The W boson tagging algorithm efficiency correction also incurs uncertainties [27, 25].

Data-driven corrections for simulated backgrounds and the multijet event estimate entail specific uncertainties. The W+jets event simulation correction uncertainty is set at 60%. The $t\bar{t}$ S_{T} shape reweighting uncertainty encompasses statistical and systematic components, the latter stemming from the uncertainty in the single top contribution within the $t\bar{t}$RWR. Multijet background estimation involves a 100% uncertainty in the Matrix Method estimate and an additional 100% uncertainty for reconstructed VLQ invariant masses (m_T^{lep}) below 200 GeV as described previously.

7.6 Statistical Analysis and Results

The investigation for the presence of a VLQ signal employs a fit to the reconstructed mass distributions of the leptonically decaying T-quark candidate (m_T^{lep}) from both the signal regions (SR1 and SR2) and the control regions ($t\bar{t}$CR, $S_{\text{T}}^{\text{Low}}\Delta m$CR, and $S_{\text{T}}^{\text{High}}\Delta m$CR), collectively referred to as the fit regions. The m_T^{lep}'s selection is predicated on its superior resolution and sensitivity relative to that of the hadronically decaying T-quark counterpart$m_{\text{T}}^{\text{had}}$. The fitting process utilizes a binned likelihood function, $\mathcal{L}(\mu, \boldsymbol{\theta})$, formulated from the Poisson probabilities across all bins in the analysis. This function is dependent on the signal strength parameter of interest, $\mu = \sigma^{\text{test}}/\sigma^{\text{theory}}$, alongside a vector of nuisance parameters (NP), $\boldsymbol{\theta}$, where σ^{test} and σ^{theory} represent the tested VLQ cross-section and its theoretical prediction, respectively. Each NP, θ_i, encapsulates a systematic uncertainty using a Gaussian prior, excluding the normalization of the $t\bar{t}$ and single top backgrounds, which remain unconstrained, and the statistical uncertainties from the limited MC sample sizes, each represented by an additional NP per bin to cover the total estimated yield's statistical uncertainty within that bin. NPs affecting a process's normalization or shape by less than 1% are excluded from the fit for that process. The test statistic, q_μ, is defined via the profile likelihood ratio, $q_\mu = -2\ln(\mathcal{L}(\mu, \hat{\hat{\boldsymbol{\theta}}}_\mu)/\mathcal{L}(\hat{\mu}, \hat{\boldsymbol{\theta}}))$, where $\hat{\mu}$ and $\hat{\boldsymbol{\theta}}$ denote the parameters maximizing the likelihood, subject to $0 \leq \hat{\mu} \leq \mu$, and $\hat{\hat{\boldsymbol{\theta}}}_\mu$ are the NPs maximizing the likelihood for a fixed μ. Testing against the background-only hypothesis ($\mu = 0$) evaluates the observed data's compatibility. The cross-section times branching ratio limits for potential signals are determined using q_μ in conjunction with the modified frequentist CL_s approach [77, 69], employing asymptotic formulae for approximation [53]. A signal is excluded at $\geq 95\%$ confidence level (CL) if $\text{CL}_\text{s} < 0.05$.

Figure 26 illustrates the post-fit m_T^{lep} distributions across the five fit regions under the background-only hypothesis. The SM background m_T^{lep} distributions display a rapid falloff at higher m_T^{lep} values, in contrast to the expected signal distribution which peaks near the simulated m_{VLQ}, particularly in SR1 and SR2, facilitating its distinction from SM backgrounds. The associated event yields are tabulated in Table 2, where the total prediction's uncertainty doesn't linearly sum due to parameter correlations within the fit. Expected $T\bar{T}$ signal event counts for various VLQ models are detailed in Table 3 across all fit regions. The background-only hypothesis compatibility is quantified by integrating the test statistic's distribution beyond the observed q_0 value, computed for each considered signal scenario defined by the T-quark's mass and decay branching ratios, assuming a narrow T-quark width.

Table 2: Yields of events in the five fit regions subsequent to fitting the data under the background-only hypothesis. The uncertainties encompass both statistical and systematic uncertainties. It's worth noting that uncertainties in individual background components may exceed the uncertainty in the sum of backgrounds due to correlations [34].

	SR1	SR2	$S_{\mathrm{T}}^{\mathrm{High}}\Delta m$CR	$t\bar{t}$CR	$S_{\mathrm{T}}^{\mathrm{Low}}\Delta m$CR
$t\bar{t}$	257(33)	74(14)	46(9)	1513(150)	127(18)
W+jets	61(25)	17(7)	12(5)	213(90)	24(10)
Single Top	53(19)	40(14)	23(10)	340(120)	60(20)
Other	48(21)	15(7)	7.5(34)	160(70)	14(6)
Multijet	3(11)	0.9(31)	0.7(24)	10(40)	1(5)
Total	422(21)	146(11)	89(8)	2240(60)	226(13)
Data	430	142	83	2235	232

Table 3: Projected $T\bar{T}$ event yields in the five fit regions for different VLQ scenarios. Uncertainties encompass both statistical and systematic uncertainties [34].

Yields for $\mathcal{B}(T \to Wb) = 1$:					
m_{VLQ}/GeV	SR1	SR2	$S_{\mathrm{T}}^{\mathrm{High}}\Delta m$CR	$t\bar{t}$CR	$S_{\mathrm{T}}^{\mathrm{Low}}\Delta m$CR
1200	83(4)	26.9(13)	9.5(6)	18.7(6)	1.65(11)
1400	27.6(17)	10.6(7)	4.6(4)	2.41(10)	0.24(4)
1600	8.6(6)	3.59(24)	1.87(14)	0.273(17)	0.066(9)
1800	2.69(23)	1.47(11)	0.81(6)	0.057(6)	0.0076(15)
Yields for SU(2) singlet T :					
m_{VLQ}/GeV	SR1	SR2	$S_{\mathrm{T}}^{\mathrm{High}}\Delta m$CR	$t\bar{t}$CR	$S_{\mathrm{T}}^{\mathrm{Low}}\Delta m$CR
1200	42.9(21)	20.4(12)	9.8(8)	12.5(5)	1.49(8)
1400	14.8(9)	7.7(5)	4.2(4)	1.71(8)	0.267(24)
1600	4.66(32)	2.58(18)	1.82(16)	0.246(13)	0.057(4)
1800	1.53(13)	0.94(7)	0.75(6)	0.0526(23)	0.0101(7)

No significant excess over the background expectation is identified. Upper limits at the 95% confidence level (CL) on the $T\bar{T}$ production cross-section are established for two benchmark scenarios as a function of the T-quark mass (m_{VLQ}) combined with theoretical predictions from `TOP++2.0` (refer to Figure 27). The lower limit on m_{VLQ} is inferred from the central value of the theoretical cross-section prediction. For the scenario where $\mathcal{B}(T \rightarrow Wb) = 1$, T-quark masses ranging from 1000 GeV to 2000 GeV are excluded with cross-sections exceeding 10.1 fb to 0.27 fb at 95% CL. Relative to the theoretical cross-section, this translates to an observed (expected) lower mass limit for the T-quark of m_{VLQ} >1700 GeV (1570 GeV). For the SU(2) singlet T scenario, the observed (expected) 95% CL lower mass limit is m_{VLQ} >1360 GeV (1360 GeV). The analysis's sensitivity is chiefly constrained by the statistical uncertainty associated with the data sample size. Integrating all systematic uncertainties for the $\mathcal{B}(T \rightarrow Wb) = 1$ scenario results in a degradation of the expected cross-section limit by less than 3.7% across all tested masses, with a mere 10 GeV reduction in the expected mass limit. In the signal region, data slightly overshoots the prediction in the signal-sensitive high mass tail of the m_T^{lep} distribution, thus rendering the observed limits on both the signal cross-section and m_{VLQ} generally more stringent than anticipated. In SR1, notable bin-to-bin fluctuations are observed between 1000 to 1600 GeV in the m_T^{lep} distribution, marked by an excess in one bin and deficits in three bins relative to the prediction. However, no signal model aligns with the narrow excess observed in SR1, given the broader width of the m_T^{lep} distributions than the one-bin excess. Furthermore, SR2 does not exhibit such an excess or significant bin-to-bin data variations. The isolated excess in SR1 leads to somewhat attenuated observed cross-section limits within an m_{VLQ} interval of approximately 1250 GeV to 1500 GeV compared to the rest of the m_{VLQ} spectrum. A prior search by ATLAS, utilizing a fraction of this dataset with an integrated luminosity of $36\,\text{fb}^{-1}$, established observed (expected) 95% CL mass limits of 1350 GeV (1310 GeV) for the $\mathcal{B}(T \rightarrow Wb) = 1$ scenario and 1170 GeV (1080 GeV) for a singlet T. Hence, the current search extends the observed mass limits by 350 GeV and 190 GeV for the $\mathcal{B}(T \rightarrow Wb) = 1$ and singlet T scenarios, respectively. This enhancement in mass limits is predominantly attributable to the expanded data sample size from $36\,\text{fb}^{-1}$ to $140\,\text{fb}^{-1}$, with approximately 15% (20%) of the improvement for the $\mathcal{B}(T \to Wb) = 1$ (singlet T) scenario stemming from modifications in the analysis strategy, particularly the advancements in W boson tagging and the bifurcation of the signal region into SR1 and SR2 based on Δm_{VLQ}. To affirm that the outcomes are independent of the simulated signal events' weak-isospin, an analysis was conducted between $T\bar{T}$ events with a 1.2 TeV mass for an SU(2) doublet T-quark and the nominal SU(2) singlet T-quark sample. Both the expected event counts and excluded cross-sections align across the two samples, indicating the applicability of the derived limits to VLQ models with non-null weak-isospin. Given the absence of explicit charge identification, the $\mathcal{B}(T \to Wb) = 1$ limits extend to the pair-production of vector-like Y-quarks with a $-4/3$ charge, decaying exclusively into Wb. Conversely, the $\mathcal{B}(B \to Wt) = 1$ constraints apply to vector-like X-quark pair-production. Beyond the benchmark scenarios, alternative combinations of T-quark branching ratios were examined by adjusting the three decay modes' relative contributions. Figure 28 shows both the expected and observed lower mass limits on the T-quark as a function of its branching ratios to Wb and Ht, with the Zt decay branching ratio computed to maintain the sum of branching ratios at unity. While the primary focus is on $T\bar{T}$ production, the analysis also includes $B\bar{B}$ production sensitivity. Figure 29 showcases the expected and observed lower mass limits on the B-quark contingent on its branching ratios to Wt and Hb, with the Zb decay branching ratio adjusted accordingly. Similar to the $\mathcal{B}(T \to Wb) = 1$ case, the $\mathcal{B}(B \to Wt) = 1$ limits are relevant to vector-like X-quark pair-production.

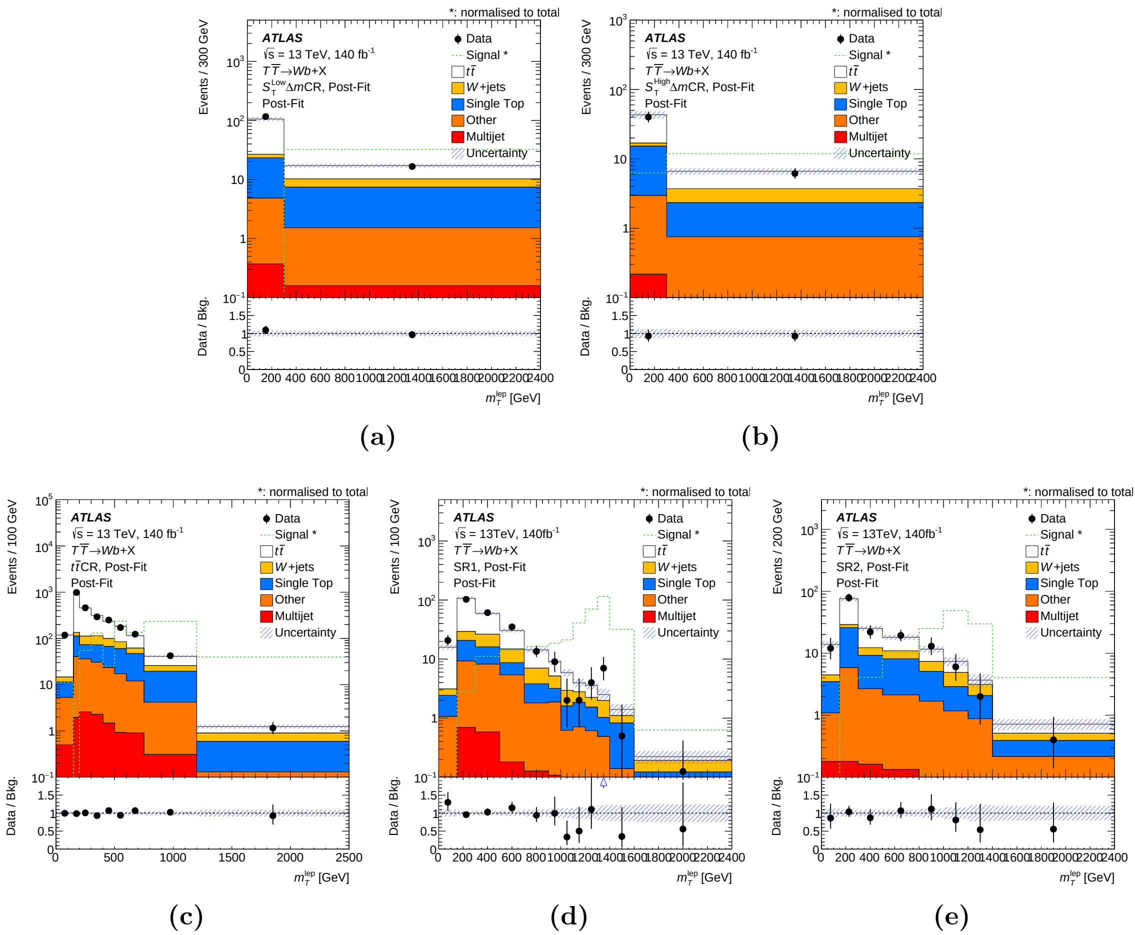

Figure 26: Distribution of m_T^{lep} showcasing data (represented by dots) and predictions (depicted as histograms in various colors) across five fit regions ((a) $S_{\text{T}}^{\text{Low}}\Delta m$CR, (b) $S_{\text{T}}^{\text{High}}\Delta m$CR, (c) $t\bar{t}$CR, (d) SR1, and (e) SR2, respectively) following the simultaneous fit to data under the background-only hypothesis (post-fit). The binning in m_T^{lep} was optimized to enhance sensitivity to the signal in signal regions while ensuring each fit region bin contains a reasonable number of data events for robust fitting behavior. The lower panels of each plot display the ratio of data to predicted background yields, with an arrow indicating points where the ratio extends beyond the ordinate range. Overflow events are included in the last bin. Error bars encompass statistical uncertainty, while shaded bands represent systematic uncertainty post-likelihood fit (details in text). In (d) SR1 and (e) SR2, dashed green histograms illustrate the signal shape with $m_{\text{VLQ}} =$ 1400 GeV and $\mathcal{B}(T \to Wb) = 1$, scaled to total background prediction. Expected signal event yields in each fit region are presented in Table 3. [34]

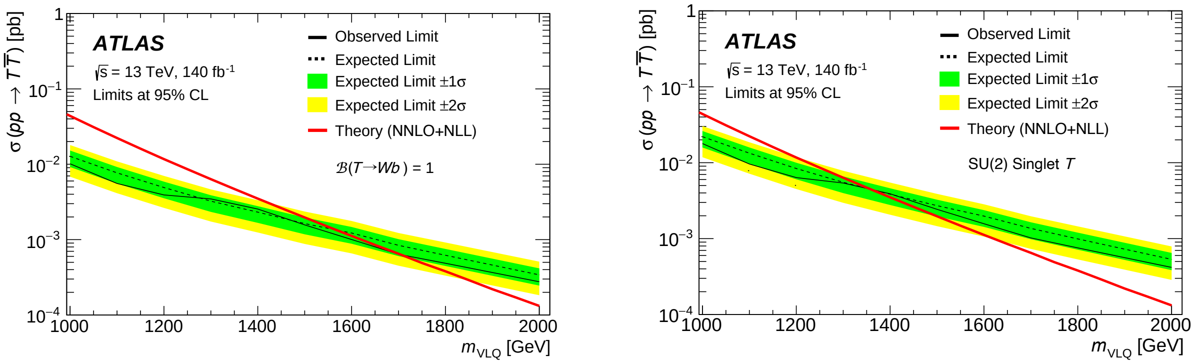

(a) **(b)**

Figure 27: Graphs depicting the expected (dashed black line) and observed (solid black line) upper limits at the 95% confidence level (CL) on the $T\bar{T}$ cross-section as a function of T-quark mass for (a) the $\mathcal{B}(T \to Wb) = 1$ scenario and (b) the SU(2) singlet T scenario. The green and yellow bands indicate ± 1 and ± 2 standard deviations around the expected limit, respectively. The thin red line represents the theoretical prediction [34].

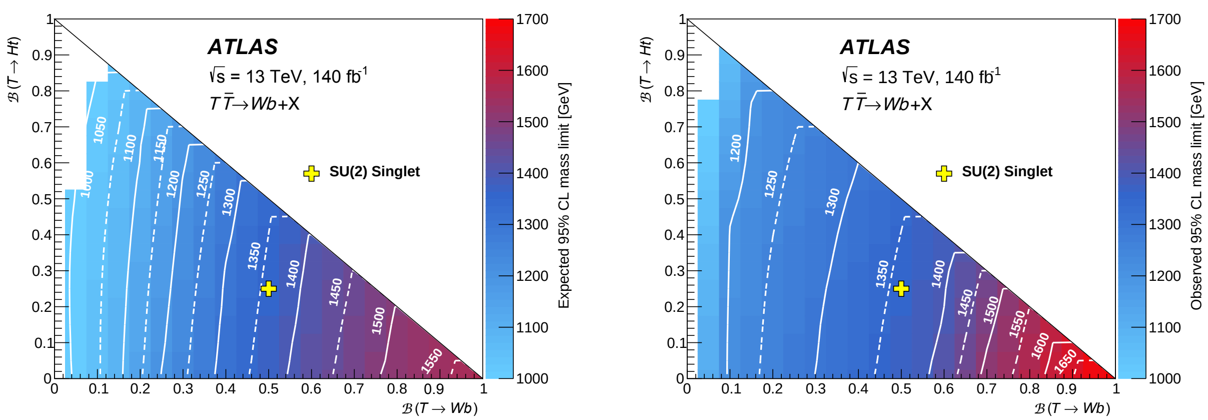

(a) **(b)**

Figure 28: (a) Expected and (b) observed 95% confidence level lower limits on the mass of the T-quark in the branching-ratio plane of $\mathcal{B}(T \to Wb)$ versus $\mathcal{B}(T \to Ht)$. Contour lines are included to aid visualization. The white region denotes where the lower mass limit falls below 1000 GeV, the lowest signal mass considered in this search. The yellow marker highlights the branching ratio for the SU(2) singlet T scenario [34].

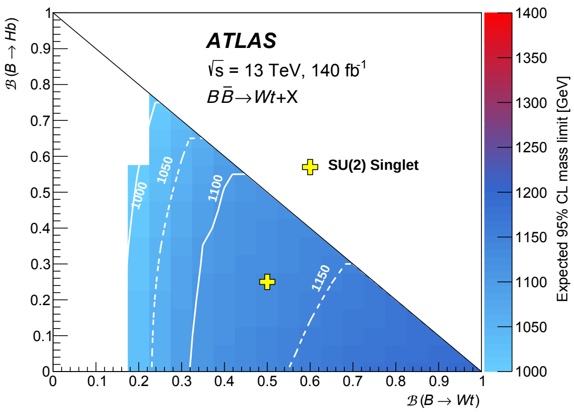

(a)

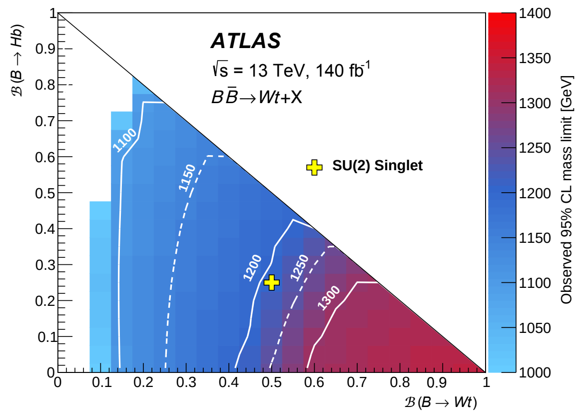

(b)

Figure 29: (a) Expected and (b) observed 95% confidence level lower limits on the mass of the B-quark in the branching-ratio plane of $\mathcal{B}(B \rightarrow Wt)$ versus $\mathcal{B}(B \rightarrow Hb)$. Contour lines are included for clarity. The white region signifies where the lower mass limit falls below 1000 GeV, the minimum signal mass considered in this search. The yellow marker denotes the branching ratio for the SU(2) singlet B scenario [34].

CHAPTER VIII

SINGLE VLQ

We begin by elucidating the criteria for selecting events, considering the expected final states resulting from the singly produced VLQs. Subsequently, we rely on our comprehension of the predominant background processes to delineate regions for signal, control, and validation in our analysis. We then present the results of a background-only fit to the control regions, validating the accuracy of the background sample modeling.

For this analysis, we utilize pp collision data collected by the ATLAS detector between 2015 and 2018, accumulating a total integrated luminosity of 139 fb^{-1}.

8.1 Event Selection

The initial step in event selection for this analysis begins immediately after the collision events occur. The ATLAS trigger system functions by capturing only those events that meet specific criteria. In the context of this analysis, which concentrates on events resulting in a leptonic final state, the triggers relevant to our investigation exclusively consider events where electrons or muons surpass a particular energy threshold and meet stringent data quality standards. Given that different trigger chains were employed during various data collection periods, the energy requirement for leptons ranged between 24 and 26 GeV, depending on the data acquisition time. To maintain uniformity, we chose to include only events featuring electrons or muons with transverse momenta p_T exceeding 27 GeV.

Figure 30 provides a comprehensive list of the triggers employed in this analysis. We exclusively utilized events that satisfied the trigger criteria shown in Figure 30, and the specific triggers were selected based on the recommendations of the ATLAS trigger group.

Run periods	Trigger Type	Trigger Name
2015	Electron	e24_lhmedium_L1EM20VH OR e60_lhmedium OR e120_lhloose
2015	Muon	mu20_iloose_L1MU15 OR mu50
2016	Electron	e26_lhtight_nod0_ivarloose OR e60_lhmedium_nod0 OR e140_lhloose_nod0
2016	Muon	mu26_ivarmedium OR mu50
2017	Electron	e26_lhtight_nod0_ivarloose OR e60_lhmedium_nod0 OR e140_lhloose_nod0
2017	Muon	mu26_ivarmedium OR mu50 OR mu60_0eta105_msonly
2018	Electron	e26_lhtight_nod0_ivarloose OR e60_lhmedium_nod0 OR e140_lhloose_nod0
2018	Muon	mu26_ivarmedium OR mu50 OR mu60_0eta105_msonly

Figure 30: Triggers used in the analysis, broken down by run period.

As explained in Chapter 6, we are unable to directly observe the VLQs under investigation; instead, we must detect their decay products. In this analysis, our focus is solely on the decay of the $T^{\frac{2}{3}}$ and $Y^{-\frac{4}{3}}$ quarks into a W-boson and a b-quark. The detector captures these decay products, converting them into physics objects. Subsequently, we utilize information about the momenta carried by these physics objects to reconstruct an invariant mass for the VLQ, denoted as m_{VLQ}. This parameter serves as the key discriminant used to assess the agreement between our theoretical predictions and the observed data.

It's worth noting that the T and Y quarks possess different charges, leading to distinct final states: $W+$ and b for the T (or $W-$ and $\bar{b}$ for the $\bar{T}$), and $W-$ and b for the Y ($W+$

and $\bar{b}$ for the $\bar{Y}$). However, this difference cannot be directly exploited due to the inability to experimentally distinguish between a b and a $\bar{b}$ in the ATLAS detector. Consequently, this distinction becomes relevant solely in the interpretation of our results. Furthermore, the W-boson, being short-lived, follows various decay paths, with this work specifically considering the leptonic decay of the W-boson.

Looking at Figure 31, it can be seen that our process will result in a specific set of particles, namely:

- one light quark
- two b-quarks
- one lepton
- one neutrino

As mentioned in Chapter 6, these particles will ideally result in the following reconstructed objects:

- one light jet
- two b-jets
- one lepton
- a significant amount of missing transverse energy (E_T^{miss})

By examining the distributions in our signal MC simulations, it becomes evident that, in most cases, only the b-jet originating from the decay of T/Y quarks can be reliably detected. The b-jet arising from gluon splitting tends to be too forward within the detector for effective b-tagging, as the ATLAS detector's tracking capability is limited to particles with pseudo-rapidity $\eta < 2.5$. Moreover, since the leading b-tagged jet corresponds to a massive resonance (the VLQ in this instance), we impose a requirement that the leading b-tagged jet possesses a transverse momentum (p_T) of at least 200 GeV.

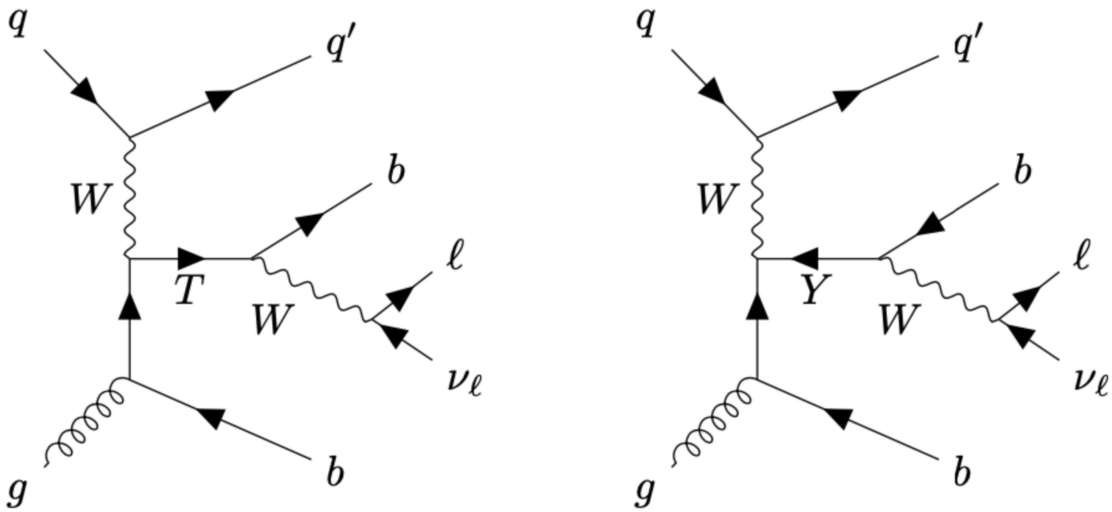

(A) A tree-level example of a T Vector Like Quark produced from Wb-fusion

(B) A tree-level example of a Y Vector Like Quark produced from Wb-fusion

Figure 31: The two main processes responsible for producing the T and Y vector-like quarks of interest to this analysis.

Based on this information, we can conclude that the following selection criteria are suitable:

- At least two jets
- The leading jet in terms of p_T must be b-tagged
- The leading jet's p_T should be $\geq$ 200 GeV
- Detection of either one electron or muon
- A minimum of 120 GeV of missing transverse energy (E_T^{miss})

This combination of criteria constitutes our "pre-selection." It serves as the fundamental set of selection requirements to capture the relevant data for our analysis, with the actual analysis regions being defined as subsets of this pre-selection region.

After applying this selection criteria, we are left with a manageable dataset that enables us to conduct our analysis. We can now proceed to assess the initial agreement between our predictions, derived from the MC simulation, and the actual experimental data, as illustrated in Figure 32.

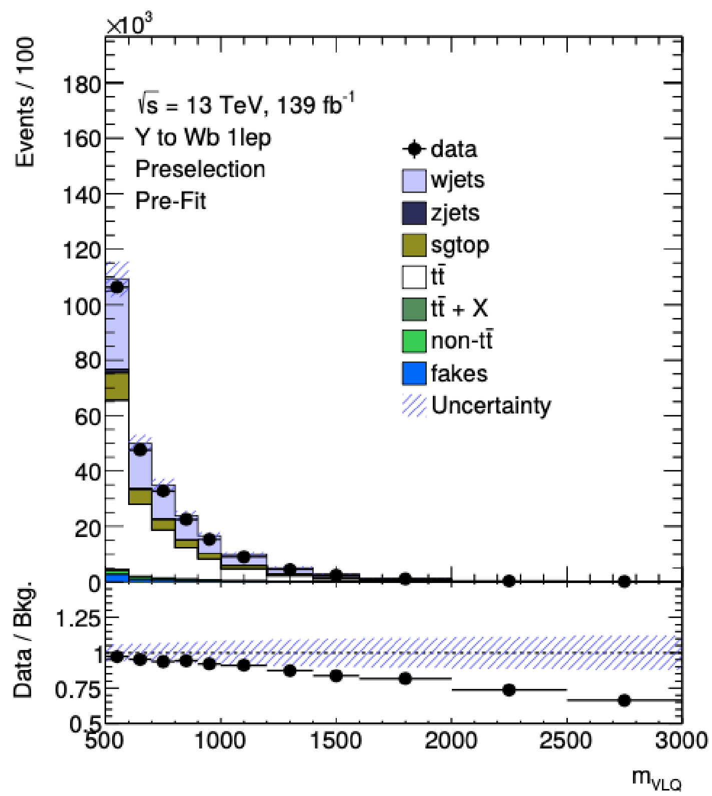

Figure 32: The m_{VLQ} distribution of the events passing the pre-selection criteria. As can be observed, there is a large overestimation of MC events at high m_{VLQ} values

As observed in Figure 33, while we anticipate capturing a significant portion of our intended signal process, the dataset is still predominantly composed of events from other processes. Notably, events stemming from W+jets, $t\bar{t}$, and single top quark-mediated processes dominate the dataset.

This insight guides us in determining the need for control regions and helps us formulate selection criteria to isolate regions rich in or devoid of these background processes.

8.2 Modeling Uncertainties

While strenuous efforts are invested in accurately representing both the signal and background samples, achieving a flawless depiction of the underlying processes remains unattain-

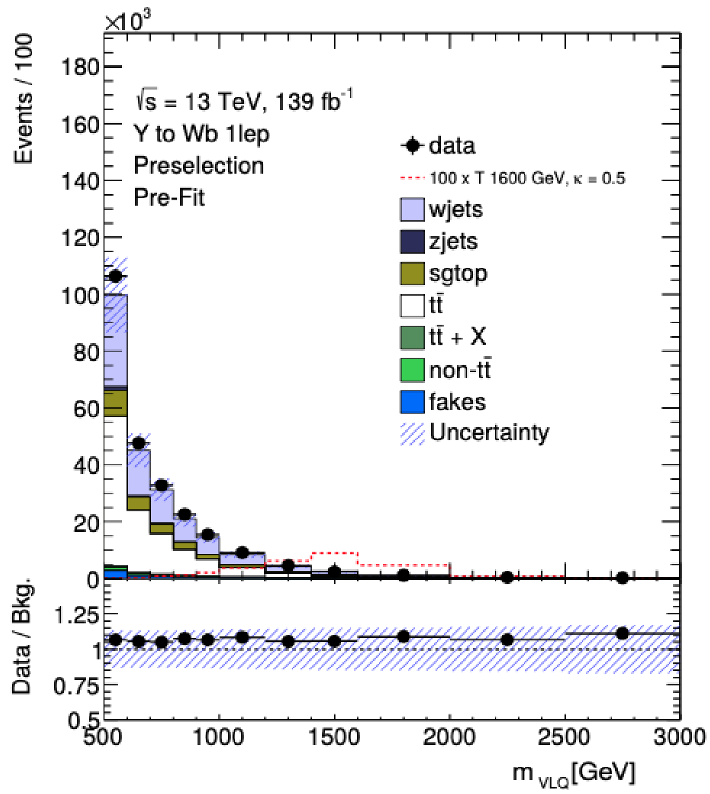

Figure 33: Reweighted m_{VLQ} distribution of the events passing the pre-selection criteria. For illustration, an example signal of a T VLQ with a mass of 1600 GeV and κ of 0.5 is shown at 100 times the expected cross-section.

able. Consequently, it becomes imperative to incorporate uncertainties that gauge our comprehension of the modeling of these processes employed in this analysis. A prevalent approach for assessing uncertainties associated with modeling involves iteratively performing the modeling process with alterations, such as employing different Monte Carlo (MC) generators, varying the showering algorithm, or adjusting model parameters.

8.2.1 W+jets Uncertainties

Six internal scale variations pertaining to the normalization and factorization scale underwent variation and were amalgamated within an envelope.

To assess uncertainties associated with the choice of PDF, the methodology delineated in [1] was followed, leveraging the NNPDF3.0NNLO [73], CT14 [44], and MMHT14 [3] PDF sets combined via reduction methods expounded in [1, 21].

Five uncertainties linked to the W+jets reweighting were applied to the W+jets MC samples, with one uncertainty corresponding to each jet multiplicity utilized in the reweighting process. These uncertainties were prudently selected to mirror the shape and magnitude of the reweighting weights applied to the W+jets MC sample.

8.2.2 $t\bar{t}$ Uncertainties

Systematic effects arising from the modeling of the hard-scatter process and parton showering were examined by comparing the MC sample utilized with alternative $t\bar{t}$ samples generated using the MadGraph5_aMC@NLO generator and showered with Pythia8.

The uncertainty stemming from the selection of the fragmentation and hadronization model was assessed by comparing it to a sample generated with the same Powheg generator as the nominal sample but showered with Herwig7 [3].

Uncertainties associated with the modeling of initial-state radiation (ISR) and final-state radiation (FSR) were evaluated by varying parameters related to additional radiation, such as h_{damp}, μ_F, and μ_R, scaling these values by a factor of two and a factor of one-half to obtain upper and lower variations, respectively. These values represent different settings of the Var3c parameter tune for Pythia8 as described in Ref [1].

Similar to the W+jets PDF uncertainties, 30 PDF sets were combined, as outlined in [3], to quantify the uncertainty related to the choice of PDF set on the $t\bar{t}$ MC sample.

An uncertainty associated with the $t\bar{t}$ reweighting is applied to the $t\bar{t}$ MC samples. This uncertainty is conservatively selected to mirror the shape and magnitude of the reweighting weights applied to the $t\bar{t}$ MC sample.

8.2.3 Single Top Uncertainties

The modeling process for single top production bears resemblance to that of $t\bar{t}$, and therefore, the estimation procedures for uncertainties related to initial-state radiation (ISR), final-state radiation (FSR), PDF, generator, and showering are analogous to those for $t\bar{t}$. Additionally, a flat 5% uncertainty on the cross-section was incorporated.

An uncertainty pertaining to the significant interference between the $t\bar{t}$ and single top Wt processes was applied to the Wt MC sample. This uncertainty accounted for variations in the next-to-leading order (NLO) predictions of these two processes under the Diagram Subtraction (DS) and Diagram Removal (DR) schemes, as detailed in [3, 21].

An uncertainty associated with the single top Wt reweighting was imposed on the Wt MC samples. This uncertainty was prudently chosen to mirror the shape and magnitude of the reweighting weights applied to the Wt MC sample.

8.2.4 Minor Sample Uncertainties

For the Z+jets and diboson samples, a 5% cross-section uncertainty was accounted for, whereas for the $t\bar{t}V$, $t\bar{t}H$, and other top processes, a 10% cross-section uncertainty was taken into consideration. Given the negligible contribution of fake leptons to this analysis, a straightforward yet cautious 50% uncertainty on the fake normalization was applied.

8.2.5 Lepton Dependence Correction

It was discovered that there is a non-negligible difference in the reconstructed variables when considering events with different lepton flavors. This must come from a deficiency in the construction of the high level variable so it must be addressed with an additional uncertainty. See Figure 34

To rectify this, an e/μ uncertainty is introduced that considers the reweighting factors in the pre-selection region with only one lepton flavor. Refer to Figure 35. The two different weights are then used as the systematic shifts to allow TRExFitter to converge on the best circumstance. To be most specific, the weight calculated from the events containing an electron is used as the "up" variation, and the events containing a muon are used as the "down" variation. See Figure 36.

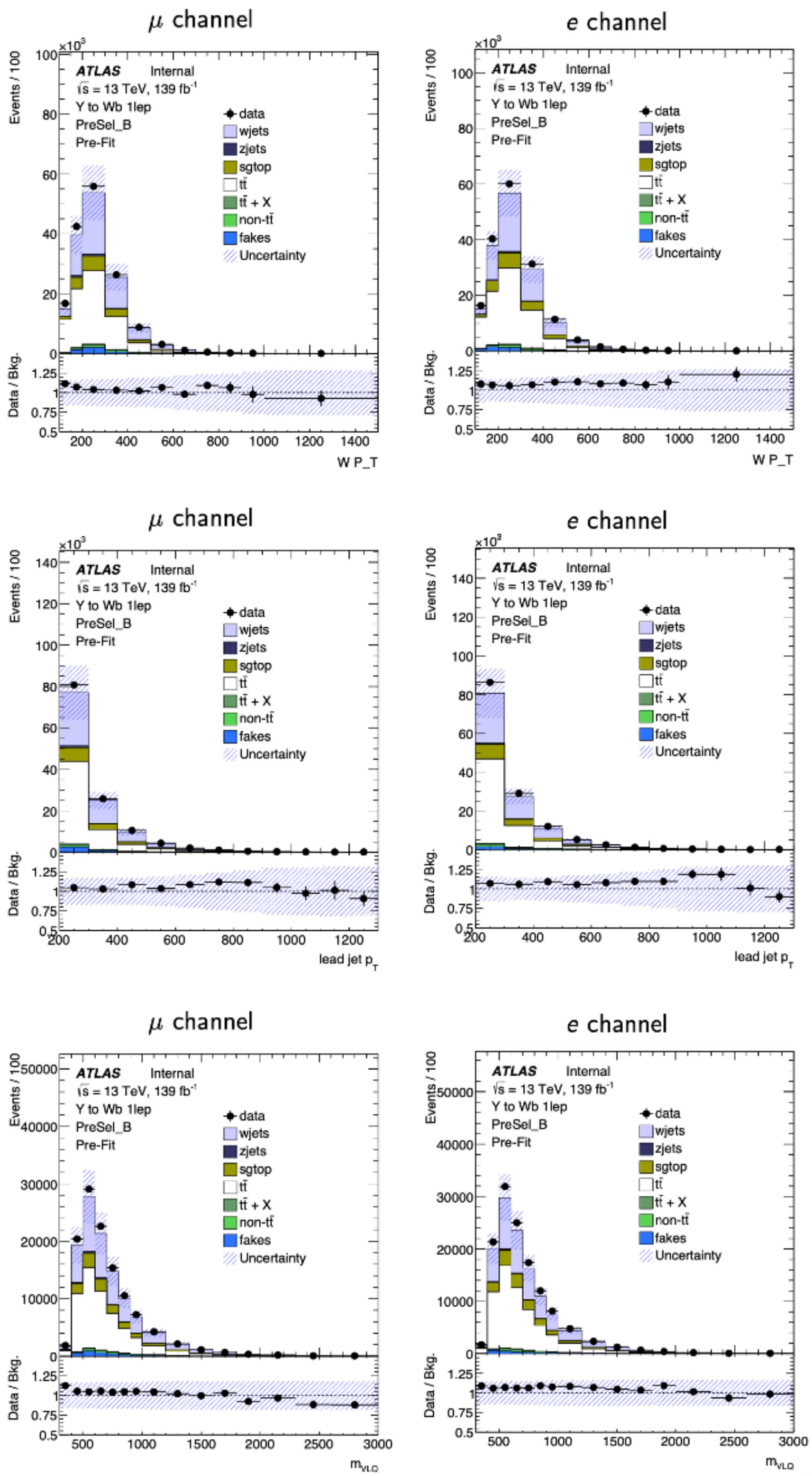

Figure 34: Reconstructed variables separated by lepton flavor.

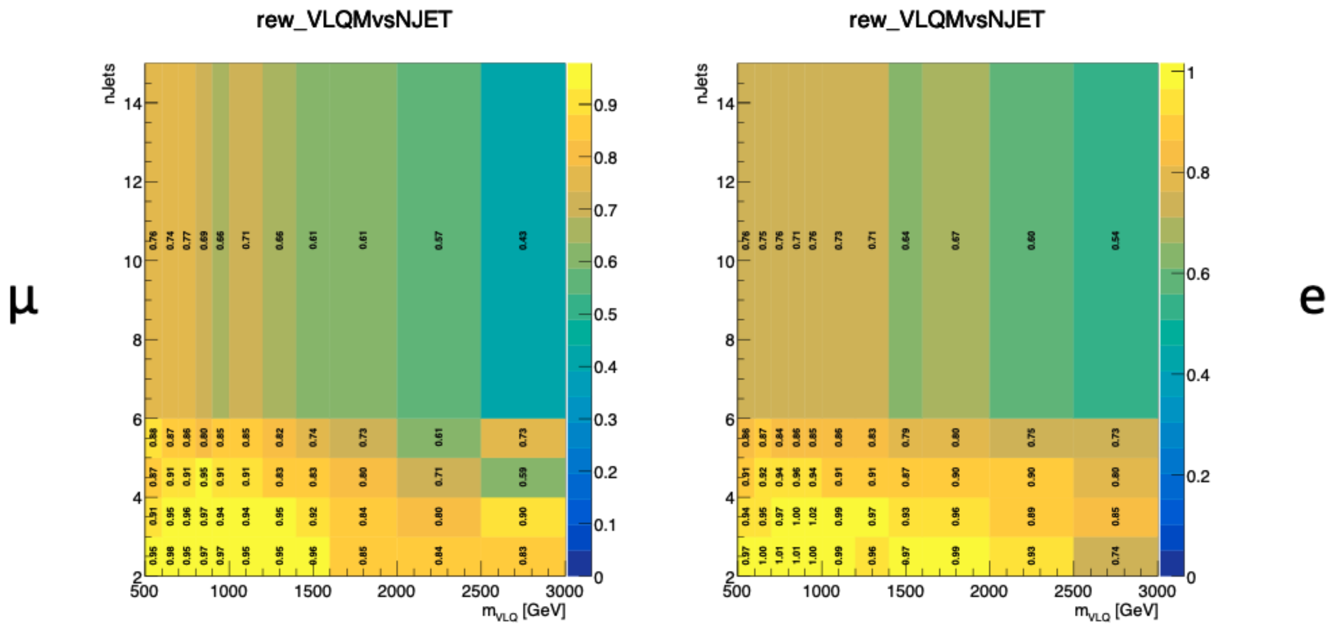

Figure 35: Reweighting factors split between lepton flavor.

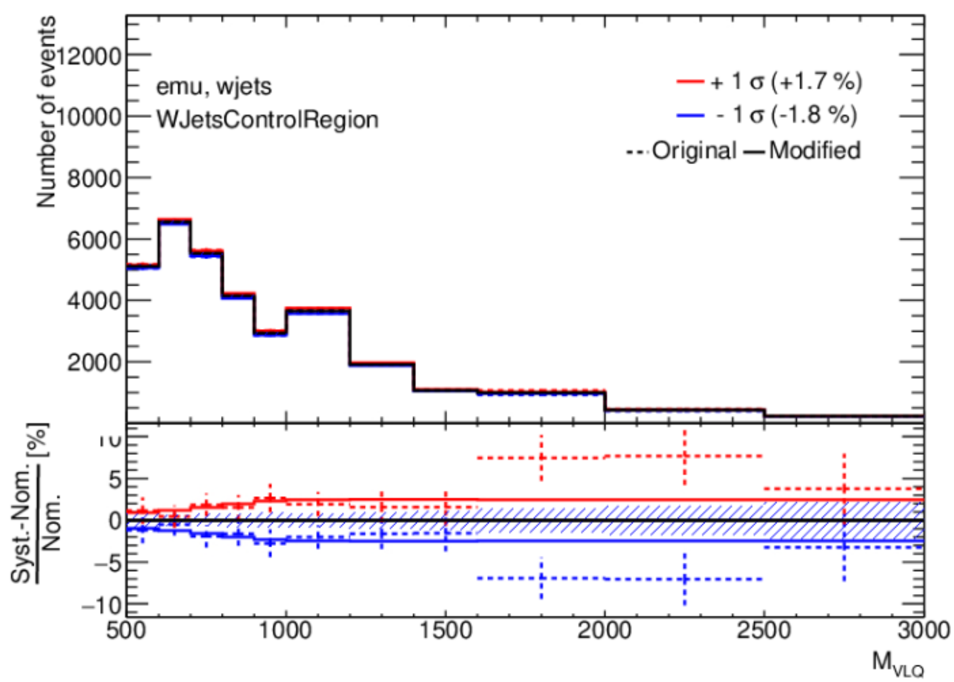

Figure 36: Sytematic variations of the m_{VLQ} distribution with lepton flavor reweighting considered.

8.3 Invariant Mass Calculation

The primary observable employed in this analysis is the invariant mass (m_{VLQ}) of the reconstructed candidate VLQ. This mass is calculated using the decay products of the proposed VLQ, specifically the b-quark and the W-boson generated during the VLQ decay.

The four-momentum of the b-quark is reconstructed as described in appendix M. However, the reconstruction of the W-boson is more intricate due to one of its decay products, the neutrino, being undetectable by the ATLAS detector within the selected channel. Nonetheless, assuming the presence of only one high-momentum neutrino in the event, the missing transverse energy (E_T^{miss}) measured in the T event should correspond to the transverse component of the neutrino's four-momentum.

The four-momenta of the neutrino and the lepton are combined and squared, with the square root of this sum equated to the mass of the W-boson. This equation yields a quadratic equation that can be solved for the z-component of the neutrino's four-momentum. In cases where no real-valued solution exists, the E_T^{miss} is adjusted by the smallest amount necessary to obtain a real-valued solution. This method, previously studied in [3], has been found to yield accurate results.

8.3.1 W+jets, $t\bar{t}$, and single top Wt reweighting

During the analysis, it became evident that there was a notable discrepancy in the modeling of background processes at high m_{VLQ} values, as evident in Figure 32. To rectify this issue and enhance the modeling in this region, reweighting factors were derived and applied to correct the modeling of W+jets, $t\bar{t}$, and single top Wt background processes within this kinematic range. The reweighting process consists of a sequential, binned 2D reweighting for W+jets events, followed by a similar procedure applied to the $t\bar{t}$ and Wt backgrounds.

The reweighting for W+jets events is obtained from a W+jets-enriched region that closely resembles the analysis pre-selection region, but with a b-tagged jet veto instead of the requirement for at least one b-tagged jet. This region primarily comprises W+jets events, ensuring that any observed discrepancies primarily stem from the misrepresentation of the W+jets background samples. The reweighting is parameterized as binned 2D scaling factors based on jet multiplicity versus m_{VLQ}.

Subsequently, the weights derived from the above step are applied on an event-by-event basis to the W+jets sample in the primary analysis region. This allows the remaining modeling discrepancies to be attributed to the misrepresentation of $t\bar{t}$ and Wt events. Given the similarities between the $t\bar{t}$ and Wt final states, they are treated together in the subsequent reweighting step. Reweighting scale factors are derived, parameterized in terms of leading jet p_T versus W p_T, using the analysis pre-selection region.

These reweighting factors effectively improve the modeling of the primary observable, m_{VLQ}, as well as other observables such as E_T^{miss}, lepton p_T, leading jet p_T, and W p_T, both at the pre-selection level and in the control and validation regions. For additional details about the procedure, please refer to Appendix R. An additional 100% uncertainty is added to this reweighting on each of the samples to ensure a conservative approach.

An updated plot of m_{VLQ} is presented in Figure 33. A clear improvement in modeling can be observed when compared to Figure 32. All plots and tables going forward in the analysis will show background samples with the reweighting applied.

8.4 Analysis Selection

As highlighted in Chapter 6, our approach involves applying specific selection criteria to distinguish between signal and background processes more effectively. This step segments the data, which has already met preliminary selection criteria, into distinct subsets, referred to as regions, for detailed analysis. Our objective is to establish a signal region predominantly composed of the signal, and based on its background characteristics, to also define control and validation regions. These latter regions aim to be enriched with the primary backgrounds identified in the signal region while minimizing signal presence.

8.4.1 b-tag multiplicity

Referring to Figure 37, it is evident that there is a substantial signal presence in both the 1 and ≥ 2 b-jet bins. However, there is a notable disparity in the background composition within these bins. The 1 b-tag bin is primarily influenced by W+jets events, whereas the ≥ 2 bin is dominated by $t\bar{t}$, with a notable contribution from single top events. Consequently, the b-tag multiplicity provides an effective means to distinguish between these backgrounds, allowing us to define control and validation regions.

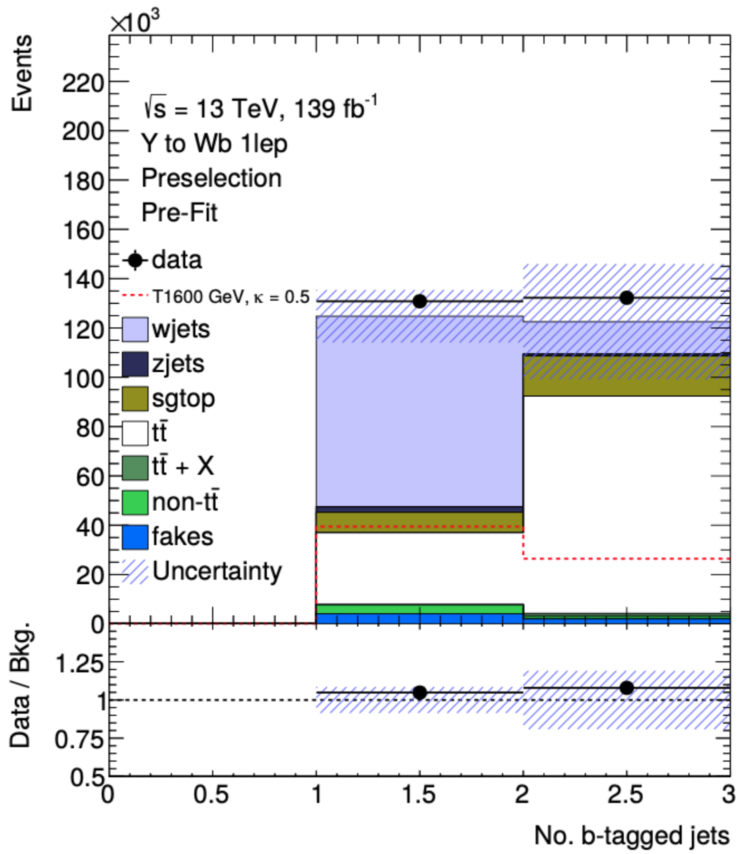

Figure 37: pre-selection level b-tag multiplicity

8.4.2 Leading Jet p_T

In the case of our heavy resonance signal, we anticipate that the leading jet originating from the decay of the VLQ will carry a substantial amount of momentum. Referencing Figure 38, it becomes evident that, unlike the backgrounds which decrease solely as the transverse momentum (p_T) increases, our signal exhibits a peak at several hundred GeV (depending on the mass of the considered VLQ candidate). Therefore, by imposing stricter requirements on the leading jet p_T, we can enhance the purity of our signal sample.

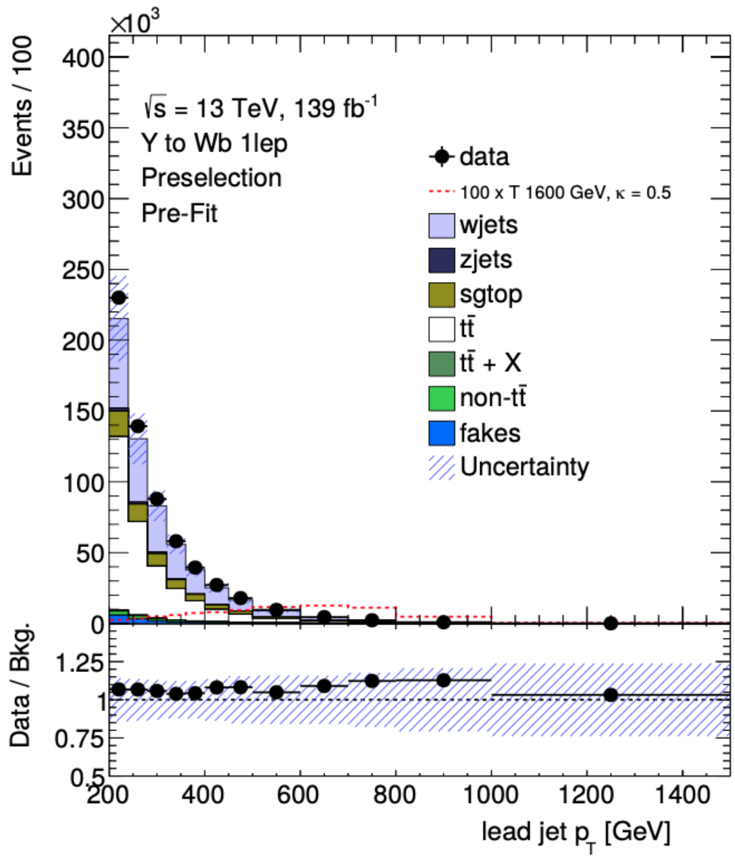

Figure 38: pre-selection level leading jet p_T

8.4.3 $|\Delta\phi(\mathbf{lepton}, \mathbf{lead\ b\text{-}jet})|$

Considering that the W-boson and the b-quark constitute the sole decay products of the VLQ, the motion of these decaying particles in the VLQ rest frame must be in opposite directions to conserve momentum. As a result, we anticipate a significant angular separation between them. As depicted in Figure 39, this separation is evident in the signal events and is also observed in the majority of our background events.

By specifically selecting events with a substantial angular separation between the lepton (the observable daughter product of the W decay) and the leading b-tagged jet, we can effectively filter out many events that do not resemble the signal. Furthermore, by choosing events with a low $|\Delta\phi(\text{lepton}, \text{lead b-jet})|$, we can establish control regions with minimal signal contamination.

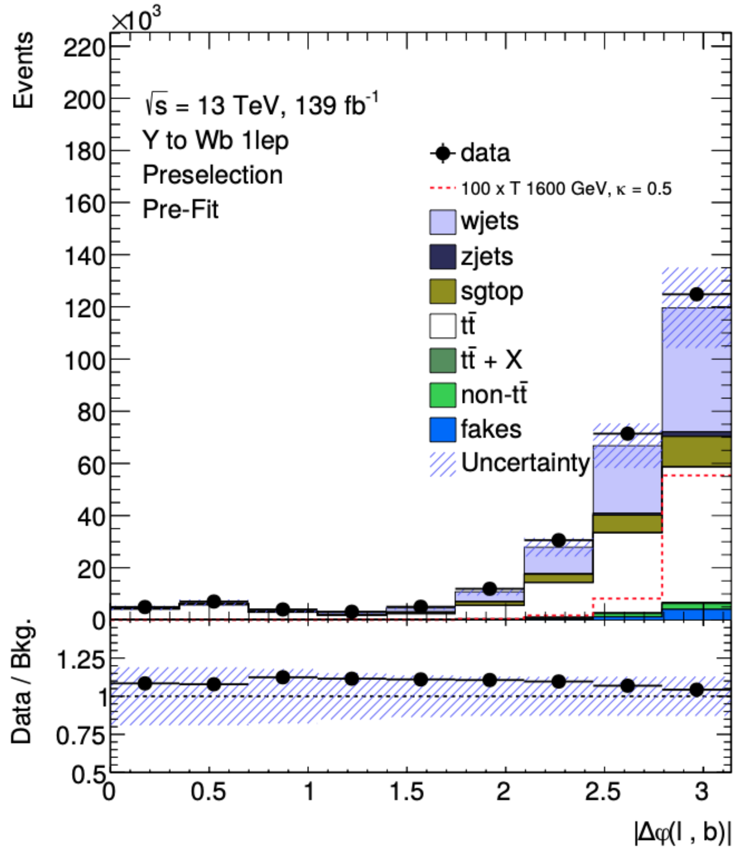

Figure 39: pre-selection level $|\Delta\phi(\text{lepton}, \text{lead b-jet})|$

8.4.4 Number of Additional Hard Central Jets

An anticipated characteristic of our signal is the likelihood of having only one jet with a substantial transverse momentum (p_T) in the event. This is distinct from certain background processes, notably $t\bar{t}$, where we might expect more hadronic activity due to the decay of two top quarks. Therefore, by tallying the number of jets with p_T greater than 75 GeV within a specified distance of our leading jet, we can effectively discriminate against a significant portion of $t\bar{t}$ events.

Figure 40 illustrates this phenomenon, with $t\bar{t}$ events peaking at one additional jet and exhibiting a gradual decline. In contrast, W+jets and our signal are more likely to have no additional jets.

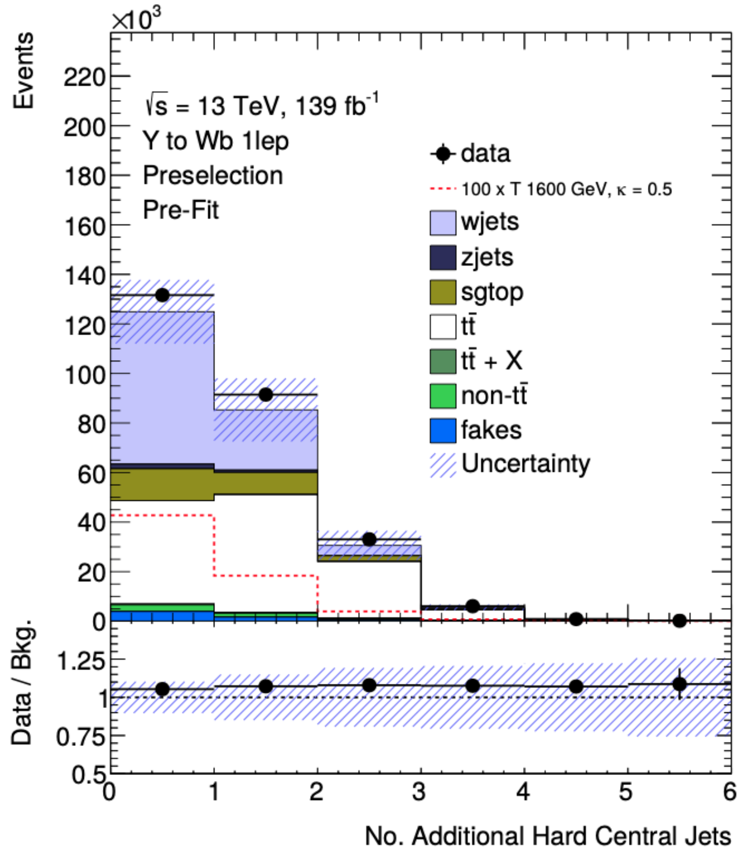

Figure 40: pre-selection level number of hard central jets

8.4.5 Forward Jets

Since our process involves two jets not originating from the decay of our VLQ, it has been observed that these jets tend to be located in the forward region of the detector, characterized by $|\eta| > 2.5$. This tendency is a distinctive feature of VLQ single production processes. By applying a selection criterion requiring at least one forward jet with $p_T \geq 40$, we can effectively reduce the presence of numerous background events.

As depicted in Figure 41, the majority of signal events exhibit at least one forward jet, while our primary background events are more likely to lack forward jets.

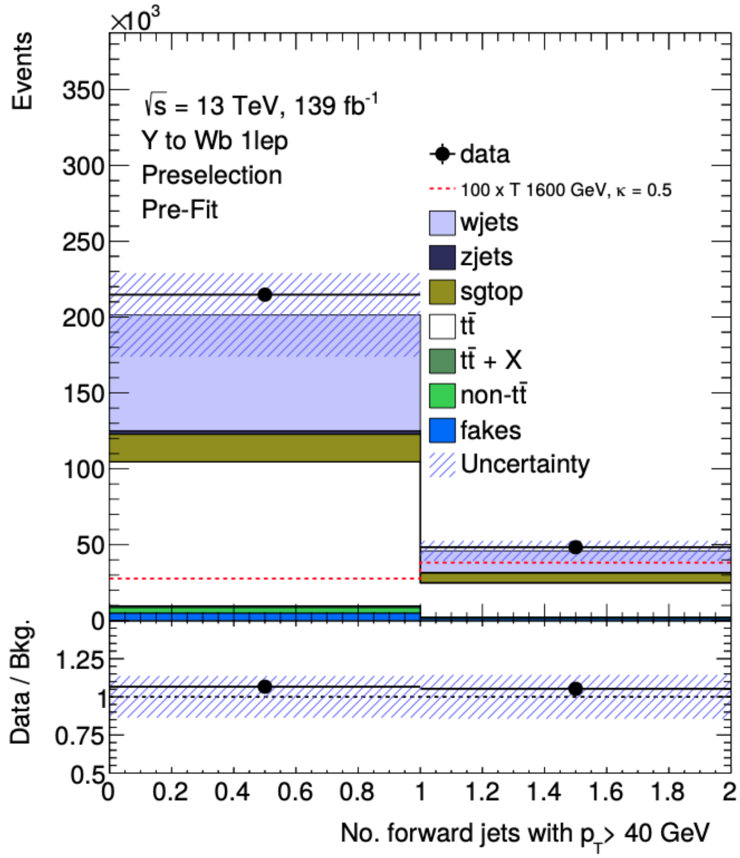

Figure 41: pre-selection level number of forward jets with $p_T \geq 40$ GeV

8.5 Region Definitions

Utilizing the aforementioned properties of our signal and background processes, we have established a set of signal, control, and validation regions. In our analysis, we applied selection criteria resulting in the creation of one signal region, two $t\bar{t}$ control regions, one W+jets control region, and two W+jets validation regions. Figure 42 outlines how the observables mentioned in previous section were employed to partition the pre-selection region into these six orthogonal regions, which are essential for this study.

The outcomes of these selection criteria are summarized in Figure 43. It is evident that the signal region is predominantly populated by W+jets events, with substantial contributions from $t\bar{t}$ and single top processes. Notably absent is a control region specifically designed for single top events. Due to the similarity in the final state of the proposed VLQ and single top

Requirement \ Region	SR	$t\bar{t}$ CR 1	$t\bar{t}$ CR 2	W+jets CR	W+jets VR 1	W+jets VR 2
Preselection						
Leptons ($p_T \geq 27$ GeV)	1					
E_T^{miss}	> 120 GeV					
Jets ($p_T > 25$ GeV)	≥ 2					
Leading jet is b-tagged	Yes					
Leading jet p_T	> 200 GeV					
Selection						
b-tagged jets	≥ 1	≥ 1	≥ 2	1	1	1
Leading jet p_T	> 350 GeV	> 200 GeV	> 200 GeV	> 250 GeV	> 250 GeV	> 250 GeV
$\lvert\Delta\phi(\text{lepton, leading jet})\rvert$	> 2.5	> 2.5	> 2.5	> 2.5	[1.5, 2.5]	[1.5, 2.5]
Jets ($p_T > 75$ GeV) with ΔR (jet, leading jet) < 1.2 or ΔR (jet, leading jet) > 2.7	0	≥ 1	0	–	–	–
Forward jets ($p_T > 40$ GeV)	≥ 1	≥ 1	0	0	≥ 1	0

Figure 42: Summary of selection requirements for all the regions considered in this analysis

production, it is challenging to establish a single top control region with similar kinematics that is depleted of signal events. While this presents a challenge, it is important to note that the single top contribution follows a decreasing distribution with respect to increasing m_{VLQ} and does not exhibit a peaked resonance feature as expected in the VLQ signal.

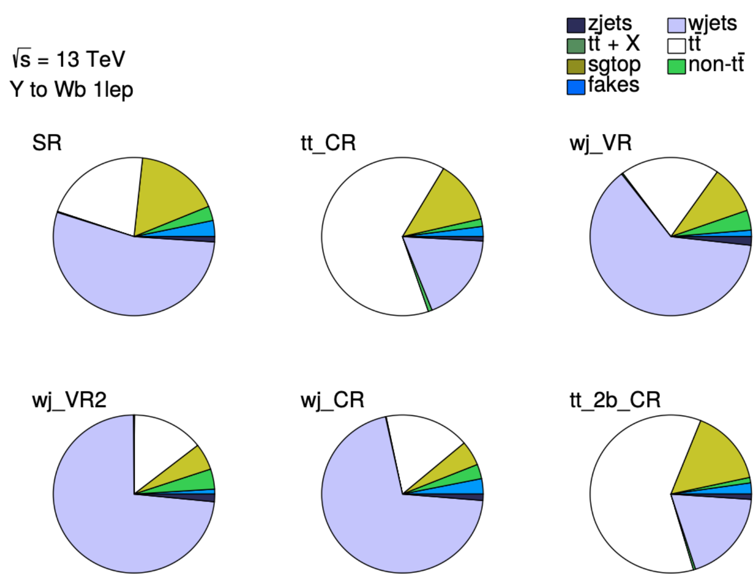

Figure 43: Relative amounts of background processes in various regions

Figure 44 illustrates the pre-fit yields for each of the control and validation regions before any fitting procedure has been applied. As shown, the predicted and observed yields in these regions are in agreement within the associated uncertainties.

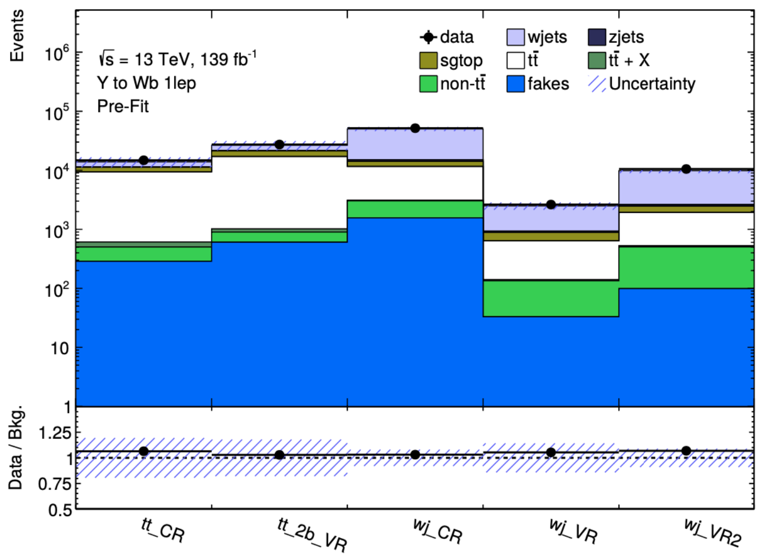

Figure 44: Predicted vs. observed yields for each control and validation region

Figure 45 presents the primary observable, m_{VLQ}, in the control and validation regions prior to performing any fitting.

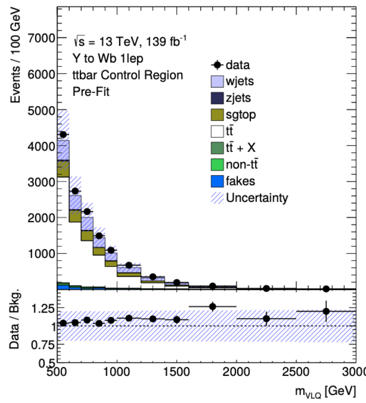

(A) m_{VLQ} in the $t\bar{t}$ CR 1

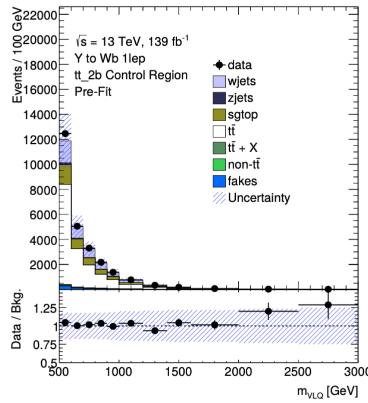

(B) m_{VLQ} in the $t\bar{t}$ CR 2

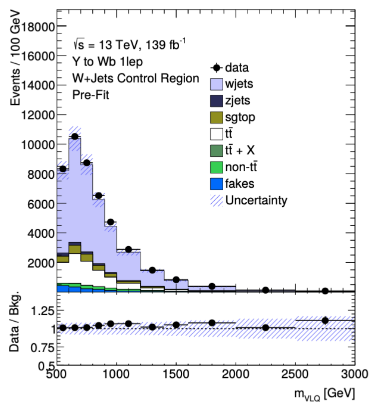

(C) m_{VLQ} in the W+jets CR

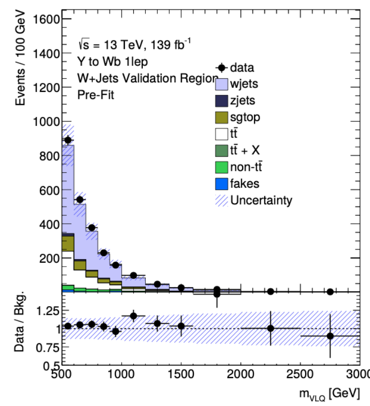

(D) m_{VLQ} in the W+jets VR 1

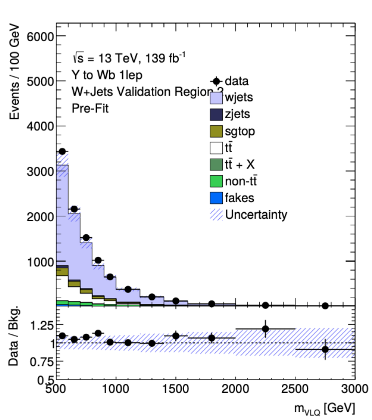

(E) m_{VLQ} in the W+jets VR 2

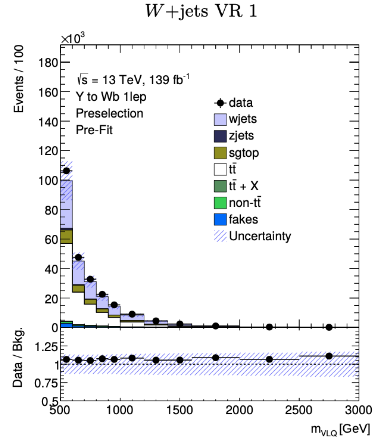

(F) m_{VLQ} in the preselection region (used as validation region)

Figure 45: Relative amounts of background processes in various regions

CHAPTER IX

THE HIGH LUMINOSITY LHC

The Large Hadron Collider (LHC) at CERN has been at the forefront of particle physics research since its inception. Its successor, the High Luminosity Large Hadron Collider (HL-LHC), represents a significant technological leap forward, aiming to increase the amount of data by a factor of ten. This section explores the HL-LHC's enhanced capabilities, emphasizing the role and impact of the newly developed Inner Tracker (ITk). The aim is to illustrate how these advancements position the HL-LHC as a superior successor to the LHC in exploring the frontiers of particle physics.

9.1 Overview of the HL-LHC

The HL-LHC is a major upgrade that will significantly increase the collider's luminosity, thereby enhancing its potential for new discoveries. For the HL-LHC, the goal is to increase the instantaneous luminosity by a factor of about 5 to 7 times compared to the original LHC. Specifically, the HL-LHC aims to achieve an instantaneous luminosity of up to 5×10^{34} to 7.5×10^{34} cm^{-2}s^{-1}. In contrast, the original design luminosity of the LHC was 1×10^{34} cm^{-2}s^{-1}, and it has been operating at around this value.

This increase in luminosity will enable physicists to observe rare processes that were previously undetectable. The HL-LHC will achieve higher luminosity through a series of technical enhancements, including high-field superconducting magnets and advanced beam optics. These improvements are not just evolutionary; they represent a transformative step in high-energy particle physics.

9.2 The Inner Tracker (ITk)

The High Luminosity era of the LHC presents unique challenges, such as increased collision rates leading to an anticipated peak luminosity of up to 7.5×10^{34} cm^{-2}s^{-1}. These conditions necessitate the upgrade of the ATLAS ID to an all-silicon Inner Tracker (ITk) to ensure continued effective operation.

9.2.1 Necessity of the ATLAS Inner Tracker Upgrade

The ITk is necessitated by the need for higher granularity and radiation tolerance. Current pixel detectors are not sufficient to handle the expected influx of up to 1×10^{16} $\mathrm{n_{eq}/cm^2}$. The ITk will feature enhanced pixel sizes, particularly in the innermost layers, to maintain performance under these extreme conditions [74].

In addition to the new radiation hardness, the ITk design incorporates a higher number of readout channels, with an increase from the current 80 million to over 1 billion. This upgrade is crucial for maintaining track reconstruction capabilities in the high-density environment expected in the HL-LHC.

9.2.2 Improvements over the ID

Sensor Upgrades

- **3D Sensors:** In the innermost layers, 3D silicon sensors are employed for their superior radiation hardness. These sensors feature columnar electrodes penetrating through the silicon substrate, allowing for efficient charge collection even after significant radiation damage [74].

- **Planar Sensors:** The outer layers will use planar sensors, which are thinner (150-200 microns) compared to the current sensors. This reduction in thickness results in lower operating voltages and power consumption, while still achieving high charge collection efficiency [74].

The ITk utilizes the ITkPixV4 readout chip, designed for high data throughput and radiation tolerance. This chip supports a pixel pitch down to $50 \times 50 \mu$m [74] and includes features like in-pixel discrimination, time-over-threshold measurement, and data sparsification to handle the high data rates. In order for these readout chips to funcation more efficiently, they are powered in series rather than in parallel. This preprocess problems such as how to handle the loss of one chip in the series, which is why the shunt mode for the front end chip was designed, allowing the power to skip over the bad chip. Further solutions are required however, such as maintaining a constant voltage after a chip has entered into shunt mode. This is handled with the series power program that is supplied to the chip chain.

Volumetric Efficiency and Data Rates

- **Serial Powering:** The ITk adopts a serial powering scheme for the pixel modules, significantly reducing cable mass and improving material budget inside the detector [74].

- **Data Transmission:** Upgraded data links support higher bandwidths (up to 5 Gbps) to handle the increased data volume. The use of optical links for data transmission ensures fast and reliable data handling.

The pixel modules in the ITk are designed for easier assembly and maintenance. The staves, which hold multiple modules, are constructed using lightweight carbon fiber and feature integrated cooling and electrical services. This design minimizes material in the tracking volume and optimizes detector performance. The staves are responsible for module security in the barrel section, while 17 ring like structures are placed in the end-caps to ensure full solid angle coverage (see Figure 46). The ITk's mechanical structure is optimized for stability and minimal material usage. Extensive system tests done at SLAC, which will be mentioned in the next chapter, demonstrate the robustness of the modules and the integrated cooling and electrical systems, ensuring the ITk's readiness for the challenging conditions of the HL-LHC.

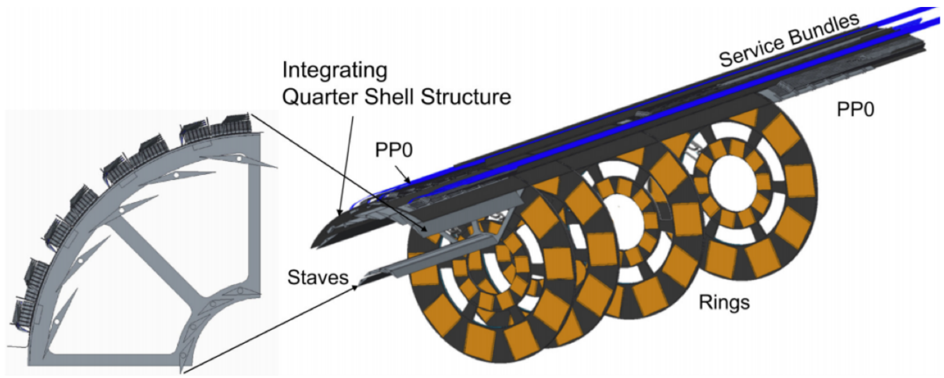

Figure 46: The ITk quarter shell, outlining the geometry of the local support structures and the modules

CHAPTER X

MODULE PLACEMENT QUALITY ASSURANCE

10.1 Specifications and Procedures

10.1.1 Thermal Conductivity

To ensure the RD53A module operates within its designated temperature range, providing a consistent thermal bond for thermal conduction is paramount. The cooling properties of the supporting structure serve as the primary means to achieve high efffeciency thermal conduction. Employing SE4445 adhesive as the interface between the module and the local support, we rely on its thermal conductivity to facilitate effective heat dissipation. Though direct measurement of thermal conductivity is challenging, we can assess two key indicators closely associated with it: glue coverage and thickness.

Unfortunately, direct observation of glue patterns on the local support Ring with loaded modules is unfeasible. The procedural guidelines provided are tailored for pre-construction adjustments to optimize performance. These adjustments serve as a basis for the subsequent loading procedure of the Ring. While minor deviations may occur, we anticipate minimal variance in outcomes.

10.1.2 Translational Placement

Commonly known as "X-Y" placement, this term denotes the precise positioning of modules relative to the supporting structure. This alignment is crucial to the role of pixels as a tracking system within the detector. Any deviation from the correct placement could result in gaps within the tracking system, compromising the intended 100% coverage.

10.1.3 Glue Thickness: $100\mu m^{+100\mu m}_{-50\mu m}$

Ensuring consistent heat dissipation from the RD53A module necessitates the presence of a uniformly thick adhesive layer. To achieve this, 106μm $\pm 6\%$ Mosci Soda Lime Glass Spheres (illustrated in Figure 47) are incorporated during the mixing of the two-part adhesive. This inclusion serves to regulate the bond line between the sensor and the carbon fiber local support. The adherence to the desired thickness is confirmed through measurements using a bench-top micrometer (refer to Figure 48).

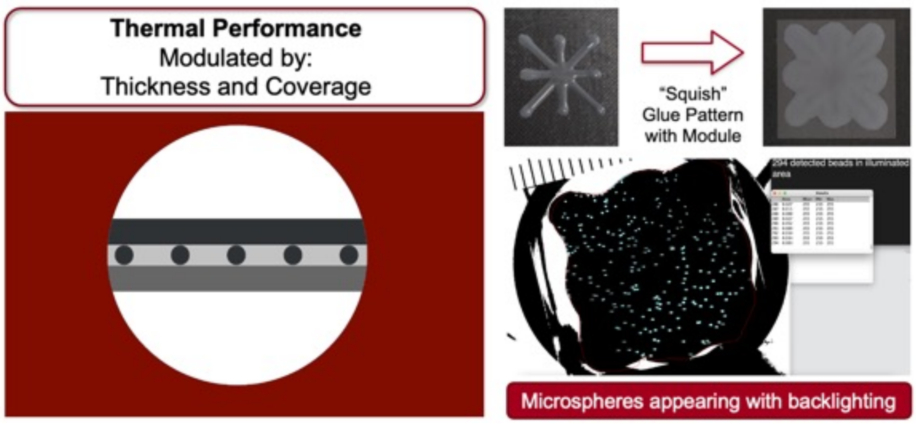

Figure 47: Bond line control with Mosci microspheres

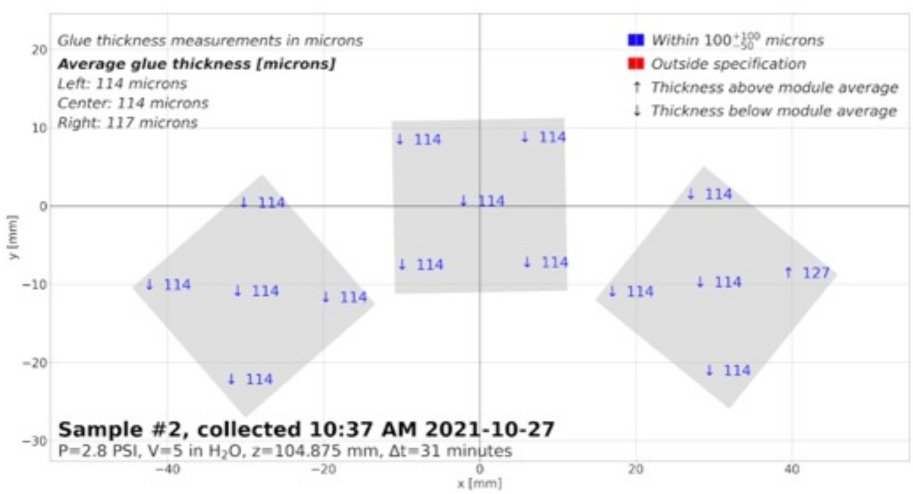

Figure 48: Glue thickness measurements for the triplet configuration

Procedure

During the mixing process, beads are added to adhesive by weight, as outlined in the mixing procedure. To ensure uniform distribution of beads, verification is conducted, as depicted in Figure 47. This verification occurs during the glass on Kapton Ring stages, before the module is positioned. Tooling adjustments are necessary to facilitate proper landing height, with specifications provided in the additional resources section. The bridge incorporates 3 micrometers that establish the height, contacting the Ring baseplate. To set the micrometers accurately, a module is placed without glue, and a 100μm shim is inserted between the module and the Ring. This slight difference in thickness compared to the microbeads guarantees a positive landing onto the beads. It is crucial to execute this dry setting with caution to prevent excessive pressure on the beads, which could lead to a “teeter-totter” effect. Finally, thickness measurement is conducted using a dial gauge, as illustrated in the following Figure 49.

Figure 49: Benchtop dial gauge accurate to 0.006μm

10.1.4 Glue Coverage: 75% to 85%

The selection of the minimum percent coverage was guided by the necessity for optimal thermal conductivity surface area exposure. However, determining the maximum percent coverage is not as straightforward. While 100% coverage may initially appear ideal as it would facilitate the highest thermal energy transfer, it introduces the risk of glue squeeze-out along the edges of the module, as depicted in Figure 50.

Figure 50: Glue squeeze-out observed when too much glue is dispensed.

The occurrence of glue squeeze-out presents a significant challenge due to the proximity of the wire bonds to the edges of the modules, rendering them highly susceptible to damage. Consequently, ensuring the exclusion of glue (and any other substances) from this critical region is paramount.

Procedure

Thickness is intricately linked to glue coverage, with detailed instructions provided in the glue thickness procedure. Another crucial parameter under our control is the volume of glue, which we adjust to achieve the desired coverage. Mass samples are extracted from the robot, with detailed information available in the additional resources section. The robot executes a program to create a star pattern without descending to meet the baseplate in the Z component. We then collect the dispensed glue amount and record its mass. Based on this data, we determine the mass required for corresponding coverages after tuning the thickness. It's important to note that the amount of glue needed varies depending on the substrate, such as glass on Kapton versus glass on carbon fiber. Subsequently, the star pattern is dispensed under the glass cover sheet, and photos are taken with a scale included, which is vital for accurate measurement. These photos are then converted into binary colors and the scale is set. Utilizing Image J particle detection, as depicted in Figure 51, the coverage area is divided by the module area. An Image J script in .txt format is employed for calculation, where the percentage of coverage is determined by the area divided by the product of the length and width of the module sides. This basic script is uploaded to the Analysis frame of the Image J program to display the percentage for each sample, offering convenience especially for large samples like entire Kapton ring trials.

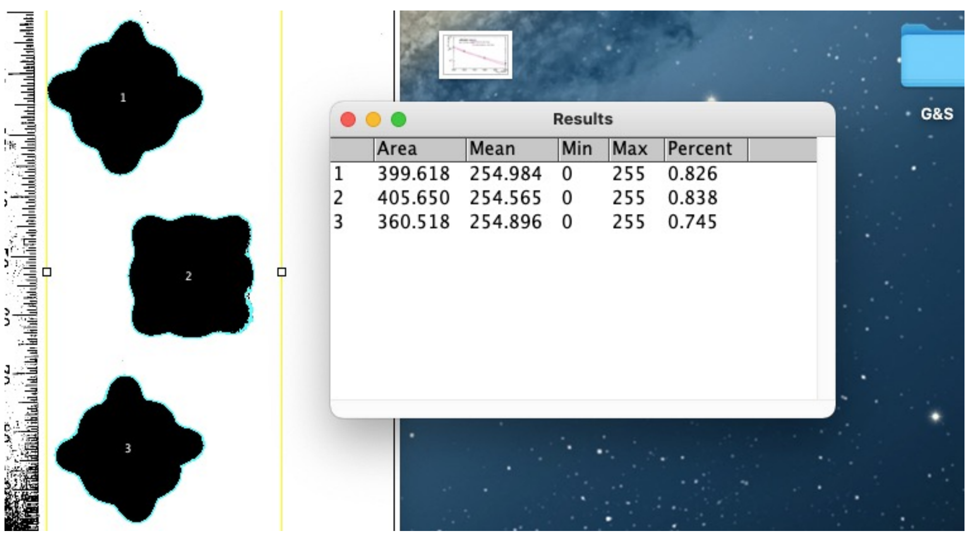

	Area	Mean	Min	Max	Percent
1	399.618	254.984	0	255	0.826
2	405.650	254.565	0	255	0.838
3	360.518	254.896	0	255	0.745

Figure 51: Image J area calculation example.

10.1.5 X-Y Placement: $\pm$ 250μm

While the tooling effectively addresses issue of translational placement, attention to detail is imperative to guarantee precision. Furthermore, the lifespan of the glue imposes constraints on the number of modules that can be placed per day (see Figure 52). It is crucial to conduct measurements on modules loaded together, meaning that the tooling baseplate remains stationary between loadings. This practice serves as an indicator of the tooling's performance. Final measurements should encompass all modules to confirm that the baseplate movements adhere to specifications.

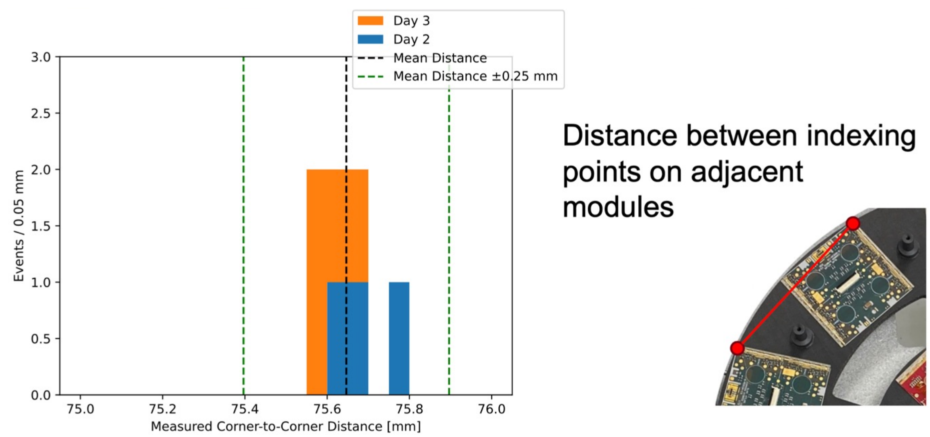

Figure 52: Average corner-to-corner distance (measurements from CMM) with 250μm tolerance band.

Procedure

Indexing the corner of the module in the pickup plate is a critical step, as illustrated in Figure 53, requiring attention to ensure the module aligns precisely against both locating edges. To avoid over-constraining the tooling, the pin and slot constraint method is employed. After the glue is dispensed, the bridge is carefully placed onto the ring baseplate, as demonstrated in Figure 54. Subsequently, the assembly is allowed to sit for 10 seconds before the vacuum is cut off, and the tool is lifted off, with tuning details outlined in the glue thickness procedure.

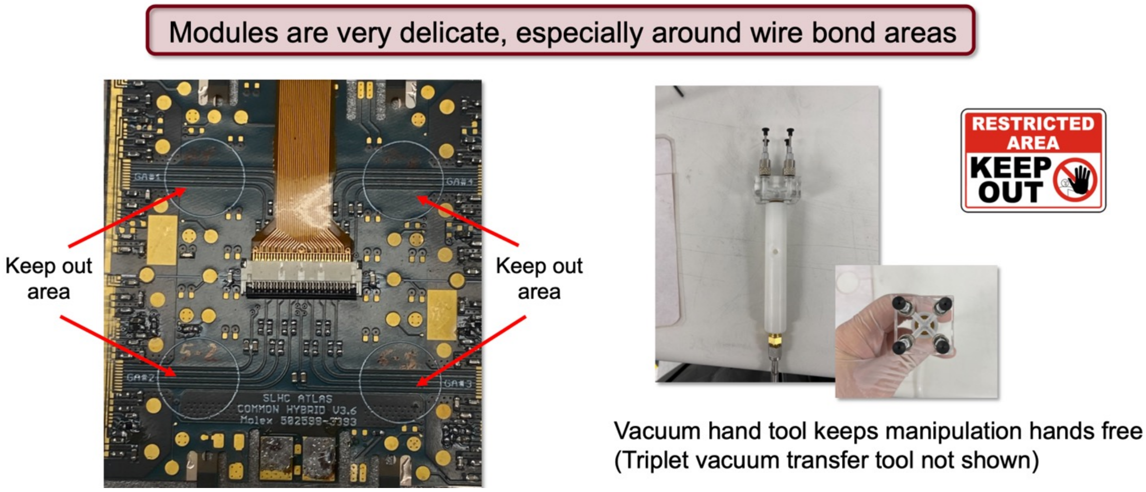

Figure 53: Placing the module into the indexing plate with pickup tool.

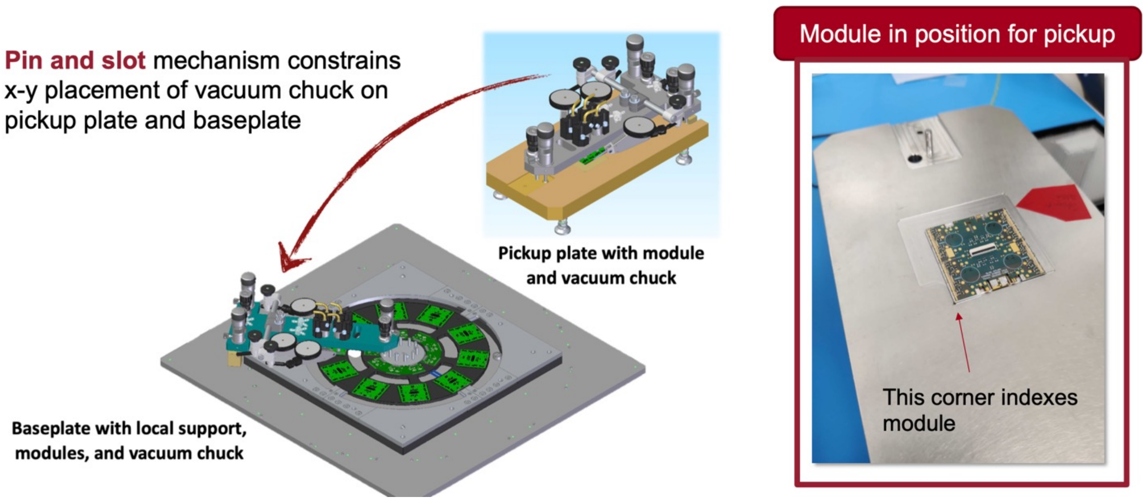

Figure 54: The vacuum bridge transporting the module from the pickup plate to the ring base plate.

10.2 Additional Activities

10.2.1 Flex Tab Cutting

To ensure safe and effective handling, modules are delivered in gel packs with flexible PCB substrate material handling frames still intact. It's imperative to free the modules from these frames using a reliable method. At SLAC, a gear-reduced mechanically actuated cutting table equipped with specialized lighting and microscope positioning was utilized for this purpose. This sophisticated setup allows for precise maneuvering during the separation process. The chisel tip, depicted in Figure 55, is employed to press down on the cutting point, which is backed with a soft material to facilitate a crisp and clean cut without damaging the module. This design boasts robustness and versatility, making it adaptable to various module configurations. Its effectiveness in safely freeing modules from their handling frames underscores its importance in the overall assembly process.

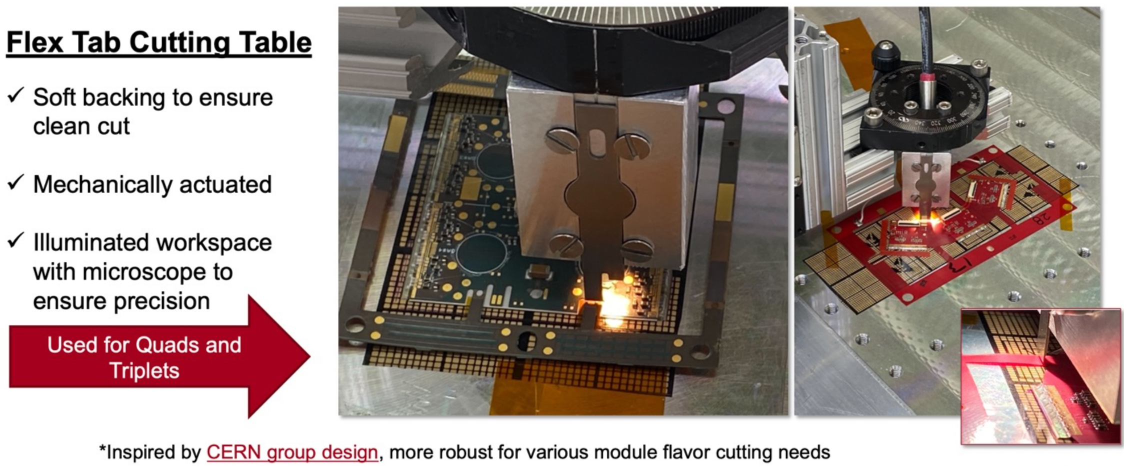

Figure 55: Flex tab cutting table.

10.2.2 Glue Mixing

Dow Corning SE4445 is received in a 2-part container which requires extraction, and combination (and the addition of glass microspheres). The eventual goal is to put the glue into the dispensing syringes seen in Figure 56.

The extraction of glue from the large container is executed using a custom piston while ensuring the components remain cold throughout the process. To streamline operations, the container is split in half, allowing each part to be handled separately, as illustrated in Figure 57. Once extracted, microspheres, depicted in Figure 58, are added to the white component based on weight. The target ratio of microspheres to glue is set at 0.7% by weight. For the specific mixing iteration described, the glue component weighed 7 grams, with 0.047 grams of microspheres added prior to mixing.

Figure 56: SE4445 as delivered to SLAC, and the filled dispensing syringes.

Mixing of the components is carried out in an orbital mixer for brief 30-second intervals, interspersed with 30-second defoaming runs to prevent heat buildup. To maintain optimal temperature conditions, the mixture is promptly returned to a freezer, where chilled steel pucks serve as effective heat sinks. Meanwhile, preparations are made at the syringe loading station. Once everything is set, the viscous mixture is carefully transferred into a sizable filling syringe, navigated through a manifold, and ultimately distributed into the dispensing syringes designed to fit snugly into the robot fixture, as depicted in Figures 59 and 60. This process ensures precise and consistent application of the adhesive mixture in subsequent assembly steps.

10.2.3 Glue Dispensing

The glue syringes are carefully retrieved from the freezer and allowed to gradually acclimate to room temperature, a crucial step to prepare them for the dispensing process. Once ready, the syringe is loaded into the robot, as illustrated in Figure 61, utilizing a 16-gauge needle for precise application. The most important part in this process is controlling the rate at which the glue is pushed from the syringe. This rate directly influences the total amount of glue dispensed in each star pattern, as the robot's program can only regulate the flow for a

Figure 57: Split glue container before extraction.

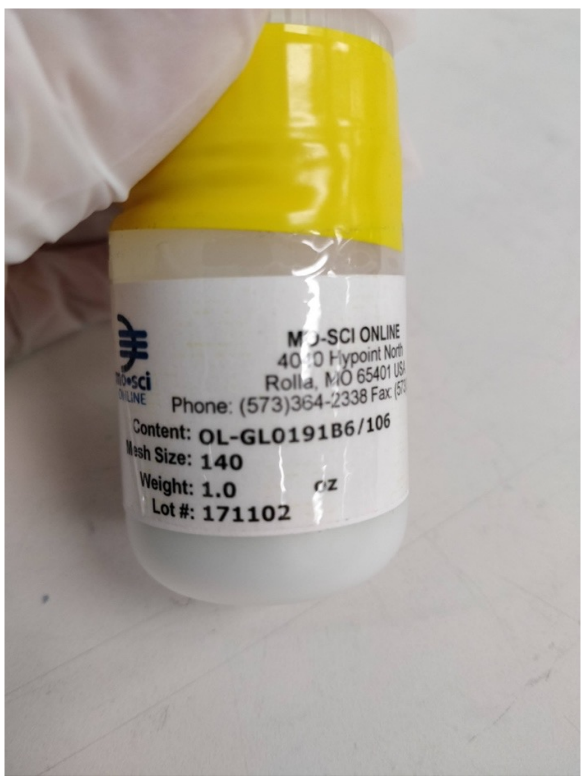

Figure 58: Glass beads in storage container.

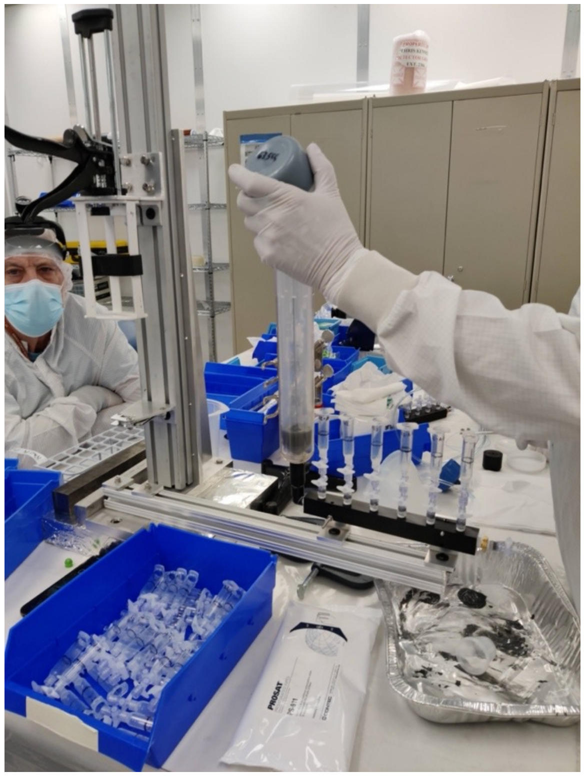

Figure 59: Transferring homogenous glue mixture into large syringe.

Figure 60: Purging the air out of the manifold prior to pneumatically filling the dispensing syringes.

predetermined duration. It's essential to note that the program controlling the robot does not directly manage the mass of glue delivered.

The air pressure exerted on the top side of the glue within the syringe plays a pivotal role in determining the dispensing rate. To ensure accuracy, mass tests are conducted, during which technicians manually adjust the pressure on the air actuating pump, as depicted in

Figure 62. This fine-tuning process allows for precise control over the amount of glue dispensed per star pattern, as demonstrated in Figure 63. This approach guarantees consistent and reliable results in the adhesive application phase of the assembly process.

Figure 61: 4D Gantry robot adapted for glue dispensing with stave baseplate loaded.

Figure 62: Air actuating pump used for providing back-pressure to dispensing syringes.

Figure 63: Star pattern being dispensed onto local support ring.

CHAPTER XI

CONCLUSION

Based on the comprehensive analyses and findings presented in this paper, the searches for Vector-Like Quarks has yielded significant insights, contributing to the ongoing quest for new particles that could uncover the fundamental structure of matter and the forces that govern the universe. The Wb+X analysis extended the previously set maximum excluded mass limits by 15% and 20% for the pair production of VLTs and VLBs to 1350 GeV and 1170 GeV respectively.

As outlined in body of the paper, there are many details that must be done meticulously in order to retain an acceptable level of sensitivity. This is exemplified in the Single VLQ analysis, where the unblinding is on the horizon.

The efforts in module placement for the ATLAS ITk upgrade highlight the importance of precision and reliability in experimental physics. The enhancements in detector technology and the implementation of rigorous quality control measures are essential for the success of future experiments, especially in the high-luminosity environment of the LHC. These advancements not only improve the accuracy of data collection but also ensure the robustness and longevity of the experimental apparatus.

Looking forward, the findings from this research pave the way for future explorations at the High Luminosity LHC. The enhanced capabilities of the upgraded ATLAS detector will enable more sensitive searches for new particles and interactions, potentially uncovering phenomena that challenge the current paradigms of particle physics. The continued pursuit of VLQs and other beyond the Standard Model candidates will require innovative approaches, collaborative efforts, and the integration of advanced technologies.

In conclusion, this paper contributes valuable knowledge to the field of high-energy physics, offering new directions for research and emphasizing the importance of technological advancements in experimental setups. As we stand on the brink of potentially transformative discoveries, the work presented here serves as a testament to the relentless pursuit of understanding the fundamental constituents of our universe.

REFERENCES

[1] Morad Aaboud et al., *Search for single production of vector-like quarks decaying into wb in pp collisions at* $\sqrt{s} = 13$ *tev with the atlas detector*, Journal of High Energy Physics **2019** (2019), 82.

[2] G. Aad, J. Butterworth, J. Thion, U. Bratzler, P. Ratoff, R. Nickerson, J. Seixas, I. Grabowska-Bold, F. Meisel, S. Lokwitz, et al., *The atlas experiment at the cern large hadron collider*, (2008).

[3] Georges Aad et al., *Search for single production of vector-like quarks decaying into wb in pp collisions at* $\sqrt{s} = 8$ *tev with the atlas detector*, Physical Review D **93** (2016), 052008.

[4] S. Agostinelli et al., *Geant4—a simulation toolkit*, Nucl. Instrum. Meth. A **506** (2003), 250–303.

[5] J. A. Aguilar-Saavedra, *Identifying top partners at lhc.*

[6] N. Arkani-Hamed, S. Dimopoulos, and G. R. Dvali, *The hierarchy problem and new dimensions at a millimeter.*

[7] ATLAS Collaboration, *Atlas flavour-tagging algorithms for the lhc run 2 pp collision dataset.*

[8] ———, *Characterization of interaction-point beam parameters using the pp event-vertex distribution reconstructed in the atlas detector at the lhc*, (2010).

[9] ———, *Observation of a new particle in the search for the standard model higgs boson with the atlas detector at the lhc*, (2012).

[10] ———, *Tagging and suppression of pileup jets with the atlas detector*, (2014).

[11] ———, *Muon reconstruction performance of the ATLAS detector in proton–proton collision data at $\sqrt{s} = 13$ TeV*, (2015).

[12] ———, *Vertex reconstruction performance of the atlas detector at $\sqrt{s} = 13$ tev*, (2015).

[13] ———, *Electron efficiency measurements with the atlas detector using the 2015 lhc proton–proton collision data*, (2016).

[14] ———, *Muon reconstruction performance of the atlas detector in proton–proton collision data at $\sqrt{s}$ = 13tev*, (2016).

[15] ———, *Performance of missing transverse momentum reconstruction with the ATLAS detector using proton–proton collisions at $\sqrt{s} = 13$ TeV*, (2016).

[16] ———, *Jet energy scale measurements and their systematic uncertainties in proton–proton collisions at $\sqrt{s}$ = 13tev with the atlas detector*, (2017).

[17] ———, *Performance of the atlas trigger system in 2015*, Eur. Phys. J. C **77** (2017), 317.

[18] ———, *Reconstruction of primary vertices at the atlas experiment in run 1 proton–proton collisions at the lhc*, (2017).

[19] ———, *Topological cell clustering in the atlas calorimeters and its performance in lhc run 1*, (2017).

[20] ———, *ATLAS b-jet identification performance and efficiency measurement with $t\bar{t}$ events in pp collisions at $\sqrt{s} = 13$ TeV*, (2018).

[21] ———, *Electron and photon performance measurements with the atlas detector using the 2015–2017 lhc proton–proton collision data*, ATL-PHYS-PUB (2018), no. 2018-01.

[22] ———, *In situ calibration of large-radius jet energy and mass in* 13 *TeV proton-proton collisions with the ATLAS detector*, (2018).

[23] ———, *Jet energy scale and resolution measured in proton–proton collisions at* $\sqrt{s}=$ 13 *TeV with the ATLAS detector*, (2018).

[24] ———, *Muon reconstruction and identification efficiency in ATLAS using the full Run 2 pp collision data set at* $\sqrt{s}=13$ *TeV*, (2018).

[25] ———, *Performance of top-quark and w-boson tagging with atlas in run 2 of the lhc*, ATL-PHYS-PUB (2018), no. 2018-03.

[26] ———, *Electron and photon performance measurements with the atlas detector using the 2015–2017 lhc proton–proton collision data*, (2019).

[27] ———, *Boosted hadronic vector boson and top quark tagging with atlas using run 2 data*, ATL-PHYS-PUB (2020), no. 2020-017.

[28] ———, *Determination of jet calibration and energy resolution in proton–proton collisions at* $\sqrt{s}$ *= 8tev using the atlas detector*, (2020).

[29] ———, *Measurement of the ATLAS Detector Jet Mass Response using Forward Folding with* 80 fb^{-1} *of* $\sqrt{s}=13$ *TeV pp data*, (2020), ATLAS-CONF-2020-022.

[30] ———, *Measurement of the c-jet mistagging efficiency in* $t\bar{t}$ *events using pp collision data at* $\sqrt{s}=13$ *TeV collected with the ATLAS detector*, (2020).

[31] ———, *Luminosity determination in pp collisions at* $\sqrt{s}=13$ *TeV using the ATLAS detector at the LHC*, (2022).

[32] ———, *Calibration of the light-flavour jet mistagging efficiency of the b-tagging algorithms with z+jets events using 139* fb^{-1}, Eur. Phys. J. C **83** (2023), 728.

[33] ———, *Search for singly produced vector-like top partners in multilepton final states with* 139 fb^{-1}, (2023).

[34] ———, *Search for pair-production of vector-like quarks in lepton+jets final states containing at least one b-jet using the run 2 data from the atlas experiment*, (2024).

[35] Atlas Collaboration et al., *Performance of the atlas transition radiation tracker in run 1 of the lhc: tracker properties*, (2017).

[36] ATLAS Collabortaion, *Atlas simulation of boson plus jets processes in run 2*, Tech. report.

[37] ———, *Estimation of non-prompt and fake lepton backgrounds in final states with top quarks produced in proton-proton collisions at $\sqrt{s} = 8$ tev with the atlas detector.*

[38] ———, *Measurements of top-quark pair differential cross-sections in the $e\mu$ channel in pp collisions at $\sqrt{s} = 13$ TeV using the atlas detector.*

[39] ———, *Parton distributions for the lhc*, Tech. report.

[40] ———, *Search for pair production of heavy vector-like quarks decaying to high-p_t w bosons and b quarks in the lepton-plus-jets final state in pp collisions at $\sqrt{s} = 13$ TeV with the atlas detector.*

[41] ———, *Studies of $t\bar{t}/tw$ interference effects in $b\bar{b}\ell^+\ell^{-'}\nu\bar{\nu}'$ final states with* Powheg *and* MadGraph5_aMC@NLO *setups*, Tech. report.

[42] ———, *Tools for estimating fake/non-prompt lepton backgrounds with the atlas detector at the lhc.*

[43] G. Avoni, *The new lucid-2 detector for luminosity measurement and monitoring in atlas*, JINST **13** (2018), P07017.

[44] Dustin Biedermann, *Search for single production of vector-like quarks decaying into wb in pp collisions at $\sqrt{s} = 13$ tev with the atlas detector*, ATL-PHYS-PUB (2020), no. 2020-017.

[45] P. Billoir, *Progressive track recognition with a kalman like fitting procedure*, (1989).

[46] R. Brout and F. Englert, *Broken symmetry and the mass of gauge vector mesons*, (1964).

[47] J. Butterworth, *Smashing physics: The inside story of the hunt for the higgs*, Headline, 2014.

[48] Jon et al. Butterworth, *Pdf*, J. Phys. G **43** (2016), 023001.

[49] M. Cacciari, G. P. Salam, and G. Soyez, *The anti-k(t) jet clustering algorithm*, Journal of High Energy Physics **2008** (2008), 063.

[50] M. Capeans, T. Flick, R. Vuillermet, G. Darbo, H. Pernegger, K. Einsweiller, M. Garcia-Sciveres, M. Elsing, O. Rohne, and C. Gemme, *Atlas insertable b-layer technical design report*, (2010).

[51] CMS Collaboration, *Observation of a new boson at a mass of 125 gev with the cms experiment at the lhc*, (2012).

[52] T. Cornelissen, M. Elsing, S. Fleischmann, W. Liebig, E. Moyse, and A. Salzburger, *Concepts, design and implementation of the atlas new tracking (newt).*

[53] G. Cowan, K. Cranmer, E. Gross, and O. Vitells, *Asymptotic formulae for likelihood-based tests of new physics.*

[54] M. Dittmar, H. K. Dreiner, and O. J. P. Éboli, *How to find a higgs boson with a mass between 155 and 180 gev at the lhc*, Physical Review D **55** (1997).

[55] R. P. Feynman, *The theory of positrons*, 1949.

[56] J. Frederick, *Statistical methods for experimental physics*, year.

[57] H. Fritzsch and M. Gell-Mann, *Current algebra: Quarks and what else?*, (1972).

[58] R. Fruhwirth, *Application of kalman filtering to track and vertex fitting*, Nucl. Instrum. Meth (1987).

[59] R. Fruhwirth, W. Waltenberger, and P. Vanlaer, *Adaptive vertex fitting*, (2007).

[60] R. Früwirth, *Data analysis techniques for high-energy physics*, year.

[61] M. Gell-Mann, *A schematic model of baryons and mesons*, (1964).

[62] S. L. Glashow, *Partial-symmetries of weak interactions*, (1961).

[63] D. Griffiths, *Introduction to elementary particles*, 2008.

[64] J. Griffiths, *Introduction to electrodynamics*, 2013.

[65] F. Halzen and A. D. Martin, *Quarks and leptons*, 1984.

[66] J. Hewett and T. Rizzo, *Collider signals of new physics*.

[67] P. W. Higgs, *Broken symmetries and the masses of gauge bosons*, (1964).

[68] C. Illingworth, *The large hadron collider: The extraordinary story of the higgs boson and other stuff that will blow your mind*, Andre Deutsch, 2014.

[69] Thomas Junk, *Confidence level computation for combining searches with small statistics*.

[70] Krane, *Modern physics*, 2020.

[71] David Krohn, Jesse Thaler, and Lian-Tao Wang, *Jet trimming*.

[72] D. Lincoln, *The large hadron collider: Unraveling the mysteries of the universe*, Oxford University Press, 2014.

[73] D. Martschei et al., *Advanced event reweighting using multivariate analysis*, Journal of High Energy Physics **2012** (2012), 159.

[74] L. Meng, *Atlas itk pixel detector overview.*

[75] A. Onion, *Nicolaus copernicus*, 2009.

[76] W. Pauli, *Exclusion principle and quantum mechanics*, (1925).

[77] A. L. Read, *Presentation of search results: the cl_s technique.*

[78] A. Salam, *Weak and electromagnetic interactions*, (1968).

[79] A. Salzburger, *Tracking tutorial, in artemis school on calibration and performance of atlas detectors*, (2008).

[80] J. Schwinger, *Quantum electrodynamics. i. a covariant formulation*, Progress of Theoretical Physics (1948).

[81] ———, *On angular momentum*, (1950).

[82] T. Sjostrand, S. Mrenna, and P. Z. Skands, *Pythia 6.4 physics and manual*, JHEP **0605** (2006).

[83] O. Sturgeon, *A brief history of physics*, (2021).

[84] The ATLAS Collaboration, *Atlas collaboration*, 2008.

[85] M. Thomson, *Modern particle physics*, 2013.

[86] S. Tomonaga, *On a relativistically invariant formulation of the quantum theory of wave fields*, Progress of Theoretical Physics (1948).

[87] S. Weinberg, Phys. Rev. Lett. **19** (1967), 1264.

[88] ———, *A model of leptons*, (1967).

[89] P. A. Zyla, *Particle data group.*

APPENDICES

A Further Definitions in the SM

Quarks

- **Definition:** Quarks are elementary particles and fundamental constituents of matter. They combine to form hadrons, such as protons and neutrons.
- **Properties:**
  - Electric Charge: Fractional charges ($\frac{2e}{3}$ or $-\frac{e}{3}$ for up/down, etc.)
  - Color Charge: Quarks carry color charge (red, green, or blue).
  - Flavor: Six types - up (u), down (d), charm (c), strange (s), top (t), bottom (b).
  - Weak Isospin: Quarks have weak isospin of $\pm\frac{1}{2}$.

Leptons

- **Definition:** Leptons are elementary particles that do not experience the strong force. Examples include electrons and neutrinos.
- **Properties:**
  - Electric Charge: Integral charges ($-e$ for electrons, e for positrons).
  - Weak Isospin: Leptons have weak isospin of $\pm\frac{1}{2}$.
  - Flavor: Three generations - electron (e), muon (μ), tau (τ); and their corresoponding neutrinos.

Gauge Bosons

- **Definition:** Gauge bosons are force carriers that mediate the fundamental forces between particles.

- **Properties:**

  - Photon (γ): Mediates electromagnetic force.

  - W and Z bosons (W^+, W^-, Z^0): Mediate weak nuclear force. The $W^\pm$ carries a charge of $\pm e$ and act on left-handed chiral particles only. They transform a particle with weak isospin to it's doublet partner, for example: $W^+ \to e\bar{\nu}_e$.

  - Gluons (g): Mediate strong nuclear force. Each gluon carries 2 color charges, for example $R\bar{B}$, or $B\bar{G}$. There is one color singlet that has no interaction with any SM field which is $1/6(R\bar{R} + B\bar{B} + G\bar{G})$. This means this (ninth) gluon cannot be produced or detected.

Hadrons

- **Definition:** Hadrons are composite particles made up of quarks. They include baryons and mesons.

Baryons

- **Definition:** Baryons are hadrons composed of three quarks.

- **Properties:**

  - Electric Charge: Can be neutral or carry integer charges.

  - Color Charge: Combinations of red, green, and blue that always combine in such a way to make a color neutral particle.

  - Examples: Protons, neutrons.

Mesons

- **Definition:** Mesons are composite particles made up of one quark and one antiquark.
- **Properties:**
  - Electric Charge: Can be neutral or carry integer charges.
  - Color Charge: Neutral in color, as they contain a quark and an antiquark pair.
  - Examples: Pions (π), Kaons (K).

Higgs Boson

- **Definition:** The Higgs boson is an elementary particle associated with the Higgs field, which gives mass to other elementary particles.
- **Properties:**
  - Electric Charge: Neutral.
  - Spin: 0.
  - Mass: Discovered mass is around 125 GeV/c^2.

B Spin Statistics

In the realm of particle physics, one of the intriguing aspects governing the behavior of subatomic particles is the interplay between their intrinsic angular momentum, or spin, and the fundamental principle known as statistics. Spin statistics lies at the heart of the quantum nature of particles and plays a crucial role in determining the overall structure and properties of matter.

Fermions and Fermi-Dirac Statistics

Fermions, such as electrons and quarks, exhibit half-integer spin values (e.g., $s = \frac{1}{2}$). The Pauli exclusion principle, formulated by Wolfgang Pauli in 1925, dictates that no two identical fermions can occupy the same quantum state simultaneously. Mathematically, this is expressed through Fermi-Dirac statistics, with the Fermi-Dirac distribution function:

$$f(E) = \frac{1}{e^{(E-\mu)/kT} + 1} \tag{B.1}$$

This equation illustrates the probability distribution of fermions at different energy levels (E) and temperatures (T), where μ is the chemical potential and k is the Boltzmann constant.

Bosons and Bose-Einstein Statistics

Bosons, characterized by integer spin values (e.g., $s = 0, 1, 2, \ldots$), follow Bose-Einstein statistics. This statistical framework, allowing an arbitrary number of identical bosons to occupy the same quantum state, is described by the Bose-Einstein distribution function:

$$f(E) = \frac{1}{e^{(E-\mu)/kT} - 1} \tag{B.2}$$

The mathematical expression above illustrates the distribution of bosons at different energy levels (E) and temperatures (T), with μ as the chemical potential and k as the Boltzmann constant.

Pauli Exclusion Priciple

Assume, for the sake of contradiction, that two identical fermions (e.g., electrons) occupy the same quantum state. This implies that both particles have the same energy level (E), the same chemical potential (μ), and the same temperature (T).

For two fermions to occupy the same state, the denominator of the Fermi-Dirac distribution function ($e^{(E-\mu)/kT} + 1$) must be equal to zero (**this "infinity" in the probablity density function is what would allow the simultaneous population of quantum states**). To avoid this contradiction, the denominator must be nonzero, ensuring that $f(E)$

remains well-defined and finite. This condition enforces the Pauli exclusion principle, preventing multiple fermions from occupying the same quantum state simultaneously.

Again, the Fermi-Dirac distribution function $f(E)$ is given by:

$$f(E) = \frac{1}{e^{(E-\mu)/(kT)} + 1} \tag{B.3}$$

Now, let's analyze the behavior of the function for different energy states:

1. **When $E = \mu$:**

   At this point, the exponent becomes $(E - \mu) = 0$. The denominator becomes $e^0 + 1 = 1 + 1 = 2$, and thus the numerator is 1. So, $f(E) = \frac{1}{2}$ when $E = \mu$.

2. **When $E > \mu$:**

   As $(E - \mu)$ becomes positive, the exponent in the denominator increases, making $e^{(E-\mu)/(kT)}$ much larger than 1. The denominator becomes dominated by the exponential term, and $e^{(E-\mu)/(kT)} + 1$ approaches $e^{(E-\mu)/(kT)}$. Consequently, the numerator remains 1, and $f(E)$ decreases towards 0.

3. **When $E < \mu$:**

   As $(E - \mu)$ becomes negative, the exponent in the denominator decreases, making $e^{(E-\mu)/(kT)}$ smaller than 1. The denominator becomes dominated by the constant 1, and $e^{(E-\mu)/(kT)} + 1$ approaches 1. Consequently, the numerator remains 1, and $f(E)$ increases towards 1.

The Bose-Einstein distribution function $f(E)$ is given by:

$$f(E) = \frac{1}{e^{(E-\mu)/(kT)} - 1} \tag{B.4}$$

Here, the numerator remains 1, similar to the Fermi-Dirac distribution function, to ensure the function is well-behaved. However, the crucial difference lies in the sign in the denominator. The Bose-Einstein distribution has a minus sign, whereas the Fermi-Dirac distribution has a plus sign.

Now, let's analyze the behavior of the Bose-Einstein distribution function for different energy states:

1. **When $E = \mu$:**

   At this point, the exponent becomes $(E - \mu) = 0$. The denominator becomes $e^0 - 1 = 1 - 1 = 0$. This leads to an undefined result, indicating that the Bose-Einstein distribution function is not defined at $E = \mu$ (**this is what leads the occupation states to can become degenerate**). This is in contrast to the Fermi-Dirac distribution, which is well-defined at $E = \mu$.

2. **When $E > \mu$:**

   The denominator becomes positive, and $e^{(E-\mu)/(kT)} - 1$ is greater than 0. The numerator remains 1, and $f(E)$ decreases towards 0.

3. **When $E < \mu$:**

   The denominator becomes negative, and $e^{(E-\mu)/(kT)} - 1$ is less than 0. The numerator remains 1, and $f(E)$ becomes negative. This behavior indicates that Bose-Einstein statistics allow for a macroscopic occupation of the lowest energy state at low temperatures, leading to phenomena such as Bose-Einstein condensation.

In summary, the logic that applies to the Fermi-Dirac distribution function, based on the Pauli exclusion principle, does not extend directly to Bose-Einstein statistics due to the different nature of bosons and their ability to occupy the same quantum state simultaneously.

The Spin-Statistics Connection

The spin statistics theorem, formulated by Julian Schwinger in 1950, establishes a connection between the spin of a particle and the type of statistics it obeys. This relationship is expressed as:

$$\text{Spin} \times \text{Statistics} = (-1)^{2s}$$

where s is the spin of the particle. For fermions ($s = \frac{1}{2}$), the right side evaluates to -1, enforcing Fermi-Dirac statistics. For bosons ($s = 0, 1, 2, \ldots$), the right side evaluates to $+1$, leading to Bose-Einstein statistics.

These mathematical formulations and principles, including the proof by contradiction, are fundamental to understanding the statistical behavior of particles based on their spin quantum numbers, providing a concise and precise framework in the field of particle physics [76, 81].

C Higgs Mechanism

The Higgs mechanism is a fundamental concept in particle physics that explains how particles acquire mass.

The Higgs field potential, as seen in Figure 64, is given by:

$$V(\Phi) = \mu^2|\Phi|^2 + \lambda|\Phi|^4 \tag{C.1}$$

- μ^2 is a parameter determining the strength of the potential.
- λ is the self-coupling constant of the Higgs field.

The Higgs field is written in its complex doublet form:

$$\Phi = \begin{pmatrix} \phi^+ \\ \phi^0 \end{pmatrix} \tag{C.2}$$

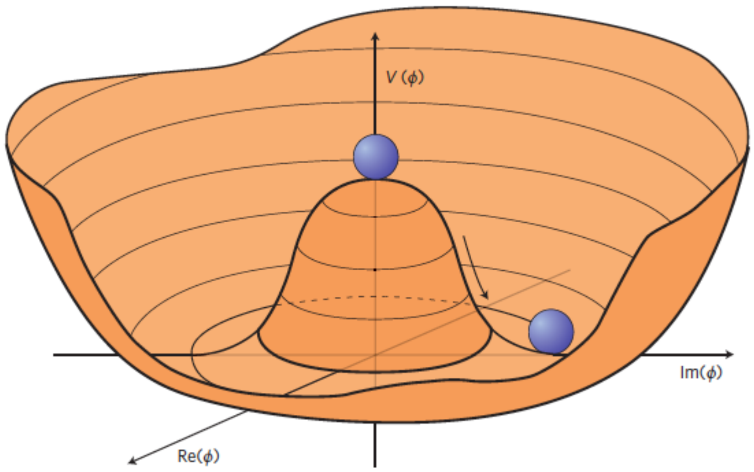

Figure 64: The geometry of the Higgs field, showing that there is no stable field at a potential energy value of zero. The "rolling" of the field value down to the VEV is the act that breaks the SU(2) symmetry and allows for the mass endowment to the other SM particles [67].

The minimum of the potential occurs when the Higgs field takes a non-zero vacuum expectation value (VEV):

$$\langle \Phi \rangle = \frac{1}{\sqrt{2}} \begin{pmatrix} 0 \\ v \end{pmatrix} \tag{C.3}$$

Here, v is the vacuum expectation value, responsible for spontaneous symmetry breaking.

Mass Terms for Gauge Bosons

The kinetic terms for the Higgs field (Φ) in the Lagrangian are expressed as:

$$\mathcal{L}_{\text{kin}} = (D_\mu \Phi)^\dagger (D^\mu \Phi) \tag{C.4}$$

Here, D_μ is the covariant derivative, incorporating the interactions with SU(2) and U(1) gauge fields:

$$D_\mu = \partial_\mu - ig\frac{\sigma^a}{2} W_\mu^a - ig'\frac{Y}{2} B_\mu \tag{C.5}$$

- g is the SU(2) gauge coupling constant.
- g' is the U(1) gauge coupling constant.

- σ^a are the Pauli matrices.
- W_μ^a are the SU(2) gauge fields.
- B_μ is the U(1) gauge field.
- Y is the hypercharge.

After electroweak symmetry breaking, the Higgs field (Φ) takes a non-zero vacuum expectation value (VEV) (v) as seen above:

$$\langle \Phi \rangle = \frac{1}{\sqrt{2}} \begin{pmatrix} 0 \\ v \end{pmatrix} \tag{C.6}$$

The mass terms for the gauge bosons (W and Z) are obtained by substituting Φ and D_μ into the kinetic terms:

$$\mathcal{L}_{\text{kin}} \supset \frac{1}{2}\left(\frac{1}{2}gv\right)^2 W_\mu^+ W^{-\mu} + \frac{1}{8}\left(\frac{1}{2}\sqrt{g^2+g'^2}v\right)^2 Z_\mu Z^\mu \tag{C.7}$$

From here, we know that mass terms in the Lagrangian take on the form:

$$\mathcal{L}_{\text{mass}} = -m^2 \psi \bar{\psi} \tag{C.8}$$

Therefore: $m_W = \frac{1}{2}gv$ is the mass of the W bosons, and $m_Z = \frac{1}{2}\sqrt{g^2+g'^2}v$ is the mass of the Z boson.

In summary, the kinetic terms of the Higgs field, in conjunction with electroweak symmetry breaking, contribute to the masses of the W and Z bosons in the Standard Model. The gauge bosons acquire mass through their interactions with the non-zero VEV of the Higgs field, which breaks the electroweak symmetry. [63, 65]

Mass Terms for Fermions

The Yukawa interactions in the Lagrangian are expressed as:

$$\mathcal{L}_{\text{Yukawa}} = -y_u \bar{Q}_L \tilde{\Phi} u_R - y_d \bar{Q}_L \Phi d_R - y_\ell \bar{L}_L \Phi e_R + \text{h.c.} \tag{C.9}$$

Here:

- y_u, y_d, and y_ℓ are Yukawa coupling constants for up-type quarks, down-type quarks, and charged leptons, respectively.
- Q_L and L_L are left-handed quark and lepton doublets.
- u_R, d_R, and e_R are right-handed up-type quarks, down-type quarks, and charged leptons, respectively.
- Φ is the Higgs field.
- $\tilde{\Phi}$ is the conjugate of the Higgs field.

Again, after electroweak symmetry breaking, the Higgs field acquires a vacuum expectation value (VEV), denoted as v:

$$\langle \Phi \rangle = \frac{1}{\sqrt{2}} \begin{pmatrix} 0 \\ v \end{pmatrix} \tag{C.10}$$

The resulting mass terms for fermions are given by:

$$\mathcal{L}_{\text{mass}} = -\frac{1}{\sqrt{2}} (y_u v \bar{u}_L u_R + y_d v \bar{d}_L d_R + y_\ell v \bar{e}_L e_R) + \text{h.c.} \tag{C.11}$$

Here:

- u_L, d_L, e_L are the left-handed components of up-type quarks, down-type quarks, and charged leptons, respectively.

- u_R, d_R, e_R are the right-handed components of up-type quarks, down-type quarks, and charged leptons, respectively.

In summary, Yukawa interactions between fermion fields and the Higgs field, combined with electroweak symmetry breaking, give rise to mass terms for fermions in the Standard Model. The strength of the interaction is determined by the Yukawa coupling constants, and the masses are proportional to the VEV of the Higgs field. [63, 65]

D Dirac's Relativistic Wave Equation

Schrödinger Equation

The Schrödinger equation, formulated by Erwin Schrödinger in 1925, governs the evolution of the wave function for non-relativistic particles:

$$i\hbar \frac{\partial}{\partial t} \Psi(\mathbf{r}, t) = H\Psi(\mathbf{r}, t) \tag{D.1}$$

Here, $\Psi(\mathbf{r}, t)$ is the wave function, H is the Hamiltonian operator, $\hbar$ is the reduced Planck constant, and $\mathbf{r}$ represents spatial coordinates.

Klein-Gordon Equation

In an attempt to describe relativistic particles, Oskar Klein and Walter Gordon independently proposed the Klein-Gordon equation in 1926:

$$\left(\frac{1}{c^2} \frac{\partial^2}{\partial t^2} - \nabla^2 + \frac{m^2 c^2}{\hbar^2} \right) \psi = 0 \tag{D.2}$$

This equation is relativistic but describes spin-0 particles. It encountered challenges related to negative probability densities, posing interpretational difficulties.

To derive the Klein-Gordon equation, one starts with the relativistic energy-momentum relation $E^2 = p^2c^2 + m^2c^4$ for a free particle, where E is energy, p is momentum, m is mass, and c is the speed of light. Then, replacing E and p with operators in the quantum formalism, the Klein-Gordon equation is obtained.

Dirac Equation

Addressing the issue of negative probabilities, Paul Dirac introduced the Dirac equation in 1928 to describe spin-1/2 particles, such as electrons. The Dirac equation is a relativistic wave equation:

$$(i\gamma^\mu \partial_\mu - m)\psi = 0 \tag{D.3}$$

Here, ψ is the four-component Dirac spinor, and γ^μ are the Dirac matrices.

The Dirac matrices are often chosen as the Pauli matrices $(\sigma_x, \sigma_y, \sigma_z)$ along with the identity matrix (I):

$$\gamma^0 = \begin{pmatrix} I & 0 \\ 0 & -I \end{pmatrix}, \quad \gamma^i = \begin{pmatrix} 0 & \sigma^i \\ -\sigma^i & 0 \end{pmatrix} \tag{D.4}$$

The four components of the Dirac spinor are written as:

$$\psi = \begin{pmatrix} \psi_1 \\ \psi_2 \\ \psi_3 \\ \psi_4 \end{pmatrix} \tag{D.5}$$

An example of a four-component Dirac spinor in the standard representation is:

$$\psi = \begin{pmatrix} \phi \\ \chi \end{pmatrix} \tag{D.6}$$

Here, ϕ and χ are two-component spinors representing the particle's amplitudes in different spin states.

The Dirac equation is derived by seeking a relativistic generalization of the Schrödinger equation. By combining the principles of quantum mechanics and special relativity, Dirac's formulation accommodates both the wave-particle duality and the intrinsic spin of electrons [65].

E The SM Lagrangian

The Standard Model Lagrangian is typically written as the sum of different terms:

$$\mathcal{L}_{\text{SM}} = \mathcal{L}_{\text{gauge}} + \mathcal{L}_{\text{fermion}} + \mathcal{L}_{\text{Higgs}} \tag{E.1}$$

1. **Gauge Boson Lagrangian ($\mathcal{L}_{\text{gauge}}$):**

$$\mathcal{L}_{\text{gauge}} = -\frac{1}{4} F^a_{\mu\nu} F^{a\mu\nu} \tag{E.2}$$

Here, $F^a_{\mu\nu}$ are the field strength tensors for the gauge bosons.

2. **Fermion Lagrangian ($\mathcal{L}_{\text{fermion}}$):**

$$\mathcal{L}_{\text{fermion}} = \sum_f \bar{\psi}_f (i\gamma^\mu D_\mu - m_f)\psi_f \tag{E.3}$$

Here, ψ_f represents the Dirac spinor for the fermion f, D_μ is the covariant derivative, and m_f is the mass of the fermion.

3. **Higgs Lagrangian ($\mathcal{L}_{\text{Higgs}}$):**

$$\mathcal{L}_{\text{Higgs}} = (D_\mu \phi)^\dagger (D^\mu \phi) - V(\phi) \tag{E.4}$$

Here, ϕ is the Higgs field, D_μ is the covariant derivative, and $V(\phi)$ is the Higgs potential.

As a starting point, we will utilize this Lagrangian to derive the equations of motion for the various fields and particles it describes. The fundamental tool for this derivation is the Euler-Lagrange equation, which provides a systematic and elegant method to obtain the equations governing the evolution of fields over spacetime.

By applying the Euler-Lagrange equations to the Standard Model Lagrangian, denoted as $\mathcal{L}_{\text{SM}}$, we aim to predict the behavior of particles in diverse physical processes. The operation involves extremizing the action, S, defined as the integral of the Lagrangian over spacetime:

$$S = \int \mathcal{L}_{\text{SM}} \, d^4x \tag{E.5}$$

The Euler-Lagrange equations for a field ϕ are given by:

$$\frac{\partial \mathcal{L}_{\text{SM}}}{\partial \phi} - \partial_\mu \left(\frac{\partial \mathcal{L}_{\text{SM}}}{\partial(\partial_\mu \phi)} \right) = 0 \tag{E.6}$$

These equations yield a set of differential equations that dictate how the fields evolve and interact. Moreover, this approach aligns with the principle of least action (just as in classical mechanics), where the Lagrangian serves as the integrand to determine the action [85].

F Feynman Rules

As mentioned in the SM section, the probabalistic nature of quantum mechanics makes the invariant amplitude one of the more valuable pieces of information that we can solve for using the SM Lagrangian and the Euler-Lagrange equation. This is not a trivial feat, however, Richard Feynman developed a pictorial formulation that makes this process much easier.

The pictorial representations of particle interactions are called Feynman diagrams, which greatly simplified the calculation of scattering amplitudes in quantum field theory. Feynman's approach provides an intuitive and graphical way to visualize and calculate complex processes without explicitly solving the Euler-Lagrange equations.

Here are the key ideas behind Feynman's rules:

1. **Feynman Diagrams:** Feynman diagrams are graphical representations of particle interactions (see Figure 65). In these diagrams, particles are represented by lines, and interactions are depicted by vertices where lines meet. The lines connecting vertices can be thought of as particle trajectories.

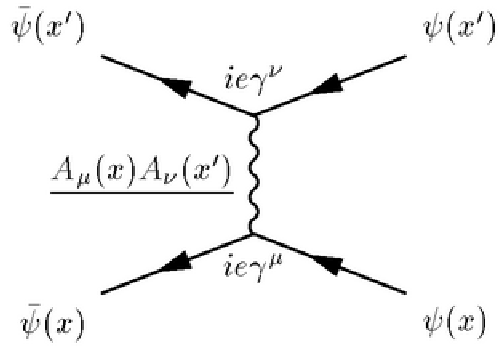

Figure 65: Example Feynman Diagram with the appropriate mathmatical formulations located adjacent to their pictorial counterpart [55].

2. **Propagators and Vertices:**

   - **Propagators (Lines):** Lines represent particles and are associated with propagators that describe the probability amplitude for a particle to travel from one point to another (see Figure 66).

   - **Vertices:** Vertices represent interactions between particles. Each vertex is associated with a factor that accounts for the probability amplitude of the interaction.

3. **Conservation of Energy and Momentum:** At each vertex, the total energy and momentum must be conserved. Feynman's rules incorporate these conservation laws, making them naturally consistent with the principles of physics.

4. **Assigning Momenta and Polarizations:** Feynman diagrams allow one to assign momenta to incoming and outgoing particles and polarizations for internal lines. This facilitates the calculation of scattering amplitudes by expressing them in terms of these momenta and polarizations.

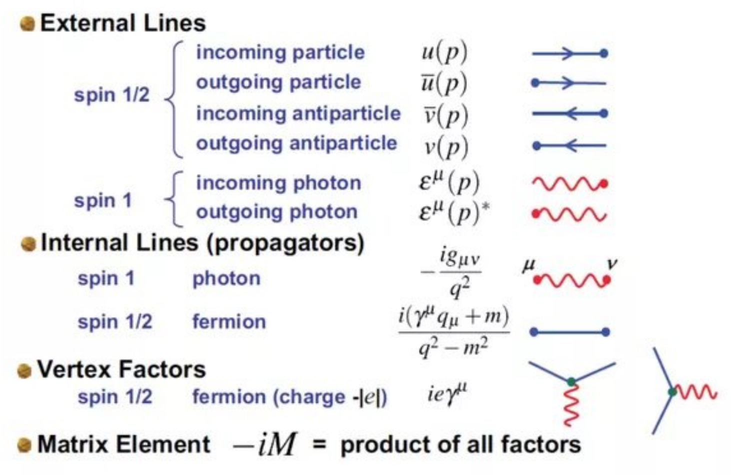

Figure 66: List of Feynman rules and their pictorial counterparts [65].

5. **Amplitude Calculation:** The amplitude for a process is obtained by combining the contributions from all possible Feynman diagrams corresponding to that process. Each diagram contributes a factor to the overall amplitude, and the total amplitude is the sum of these contributions.

6. **Path Integral Formulation:** Although Feynman diagrams provide a powerful calculational tool, Feynman also introduced the path integral formulation of quantum mechanics. This approach expresses the probability amplitude for a particle to travel from one point to another as a sum over all possible paths, each weighted by a complex exponential factor.

As an example, let's look at electron scattering.

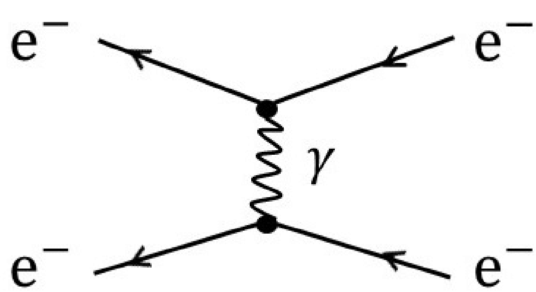

1. **External Lines:**

- Incoming electron with momentum p_1.
- Incoming electron with momentum p_2.
- Outgoing electron with momentum k_1.
- Outgoing electron with momentum k_2.

2. **Internal Line (Propagator):**

   - Virtual photon with momentum q and polarization.

3. **Vertices:**

   - Each vertex contributes a factor of $(-ie)$, where e is the electron charge.

4. **Conservation of Energy and Momentum:**

   - Apply conservation of energy and momentum at each vertex using Dirac delta functions:

$$(2\pi)^4\delta^4(p_1 + p_2 - k_1 - k_2) \tag{F.1}$$

5. **Amplitude for a Single Feynman Diagram:**

   - The amplitude ($\mathcal{M}_{\text{diagram}}$) for the single Feynman diagram is given by the product of the vertex factor and the propagator:

$$\mathcal{M}_{\text{diagram}} = (-ie)^2 \frac{g_{\mu\nu}}{q^2} \tag{F.2}$$

   - $(-ie)^2$: This term comes from the interaction vertices. Each vertex contributes a factor of $-ie$, where e is the elementary charge.
   - $\frac{g_{\mu\nu}}{q^2}$: This term comes from the virtual photon propagator. The propagator is a fundamental quantity that describes the probability amplitude for the virtual photon to travel from one point to another. It depends on the momentum of the virtual photon (q).

- $g_{\mu\nu}$: This is the metric tensor, and it represents the spacetime structure. In the context of a spacetime with Minkowski signature, the metric tensor is diagonal with entries $(-1, 1, 1, 1)$. Therefore, $g_{\mu\nu}$ is effectively the four-dimensional identity matrix.

- q^2: This is the square of the four-momentum of the virtual photon, given by $q^\mu q_\mu$. It accounts for the virtual photon's energy and spatial components.

6. **Integration for Overall Amplitude:**

   - Integrate over all internal momenta to obtain the overall amplitude for the entire process:

$$\mathcal{M}_{\text{overall}} = \int \frac{d^4q}{(2\pi)^4} \left[\mathcal{M}_{\text{diagram}}\right] \tag{F.3}$$

Feynman's rules significantly simplify the computation of scattering amplitudes compared to solving the Euler-Lagrange equations directly. They provide an intuitive, visual, and systematic method for organizing calculations in quantum field theory. Feynman diagrams became a fundamental tool in particle physics, allowing physicists to make predictions and interpret experimental results with unprecedented ease.

G Chirality and Vector-Like Particles

In the context of particle physics, the chirality of fermions, which include quarks and leptons, is a key property. The chirality of a fermion is typically denoted by the projection operators P_L (left-handed) and P_R (right-handed). Chirality makes for a better quantum number than helicity because it is Lorentz invariant.

For a given fermion field ψ (representing a quark or lepton), the left- and right-handed components are expressed as:

$$\begin{aligned} \text{Left-Handed Component:} \quad \psi_L = P_L\psi = \frac{1}{2}(1-\gamma^5)\psi, \\ \text{Right-Handed Component:} \quad \psi_R = P_R\psi = \frac{1}{2}(1+\gamma^5)\psi. \end{aligned} \tag{G.1}$$

Here, γ^5 is the gamma matrix associated with the fifth component of spacetime, and the factors of $\frac{1}{2}$ ensure normalization. The left- and right-handed components represent the chiral states of the particle.

Chirality becomes particularly relevant in the context of weak interactions, where only left-handed fermions and right-handed antifermions participate. The weak force couples exclusively to left-handed particles and right-handed antiparticles. This chiral nature is reflected in the structure of the electroweak sector of the Standard Model and is essential for understanding phenomena such as the weak decays of particles [62, 87, 78].

When considering what is and is not a chiral particle:

Chiral Particles

- **Left-Handed Fermions:** In the context of the weak force, the weak interactions involve left-handed fermions. Examples of left-handed fermions include left-handed neutrinos and left-handed components of quarks and leptons.

- **Chiral Doublets:** Some particles, especially in the context of electroweak interactions, form chiral doublets. These are pairs of particles with opposite handedness that transform into each other under weak isospin symmetry. The classic example is the electroweak doublet of leptons, such as the electron (e) and its left-handed neutrino (ν_e) [89].

Non-Chiral Particles

- **Right-Handed Fermions:** Right-handed fermions, are often considered non-chiral in the context of weak interactions. The weak force couples to left-handed fermions, therefore, right-handed fermions do not participate in weak interactions.

- **Charged Bosons:** Bosons, such as the W^+ and W^- bosons, are not chiral particles. While they mediate weak interactions, they do not exhibit chirality themselves. The weak force couples to the left-handed components of fermions, and the bosons transmit these interactions [89].

Chirality and Weak Interactions in the Lagrangian

The electroweak interactions in the Standard Model are governed by the following Lagrangian for the charged current interactions:

$$\mathcal{L}_{\mathrm{CC}} = -\frac{g}{\sqrt{2}} \sum_f \overline{\psi}_{fL} \gamma^\mu W_\mu^+ \psi_{fL} + \text{h.c.} \tag{G.2}$$

where g is the weak coupling constant, ψ_{fL} represents the left-handed component of the fermion field for a specific flavor f, W_μ^+ is the W^+ boson, and h.c. denotes the Hermitian conjugate. Notice here that only the left-handed component of the particle is acted upon by the W boson [63].

Vector-Like Particles

Now, let's introduce a vector-like fermion field χ that does not distinguish between left- and right-handed components in weak interactions [6, 66]. The Lagrangian for its charged current interactions would be:

$$\mathcal{L}_{\mathrm{CC}}^{\mathrm{VL}} = -g_V \overline{\chi} \gamma^\mu W_\mu^+ \chi + \text{h.c.} \tag{G.3}$$

where g_V is the coupling constant for the Vector-Like fermion. Again, pointing out that in this case, there is not left/right handed chiral distinction in the field the W boson is acting on.

Vector-Axial Vector (V-A) vs. Vector-Like Couplings

The chiral projection operators:

$$\begin{aligned} P_L &= \frac{1}{2}(1-\gamma^5) \\ P_R &= \frac{1}{2}(1+\gamma^5) \end{aligned} \tag{G.4}$$

are applied to fermion fields in the Lagrangian, they project out the left-handed and right-handed components of the fermion fields, respectively. This separation allows for the distinction between V-A couplings for weak interactions.

However, it's important to note that after applying the chiral projection operators, the terms in the Lagrangian do indeed manifest as combinations of left-handed and right-handed currents.

For example, in the charged current weak interaction $W^{\pm}$ -boson exchange, the interaction term involves both left-handed and right-handed components of the fermion fields:

$$\mathcal{L}_{\text{CC}} = \frac{g}{\sqrt{2}} W_\mu^+ \left(\bar{\nu}_e \gamma^\mu P_L e + \bar{u}_{\text{L}} \gamma^\mu P_L d_{\text{L}}\right) + \text{h.c.} \tag{G.5}$$

Here, $\bar{\nu}_e$ represents the left-handed electron neutrino, e represents the left-handed electron, u_{L} and d_{L} represent the left-handed up and down quarks, respectively. The chiral projection operators P_L ensure that only the left-handed components contribute to the interaction.

So while the terms in the Lagrangian may initially contain V-A couplings, after the chiral projection, they indeed manifest as left-handed or right-handed currents, depending on the specific interaction being considered.

The distinction between chirality and vector-like behavior becomes evident when comparing the coupling terms in the Lagrangians. The coupling in the chiral case depends on the left-handed components of fermion fields, while the coupling in the vector-like case treats both left- and right-handed components equally [6].

This mathematical framework reflects the essential feature of chirality in weak interactions and the departure from this chiral behavior in the case of vector-like particles.

H Vector-Like Quark Mass

In the Standard Model Lagrangian, the mass terms for fermions are introduced through Yukawa couplings with the Higgs field, see appendix C. However, for a vector-like particle, such as a Vector-Like Quark, which doesn't directly couple to the Higgs field, the mass term can be introduced differently.

Consider a Vector-Like Quark, denoted as Q, with a mass term that doesn't involve direct Yukawa coupling to the Higgs field. The mass term for this Vector-Like Quark can be written as:

$$\mathcal{L}_{\text{mass}} = -m_Q^2 \bar{Q} Q \tag{H.1}$$

Here,

- $\mathcal{L}_{\text{mass}}$ represents the mass term in the Lagrangian,
- M_Q is the mass parameter associated with the Vector-Like Quark,
- $\bar{Q}$ is the Dirac conjugate of the Vector-Like Quark field, and
- Q is the Vector-Like Quark field.

This term is similar to the mass term for a standard Dirac fermion, but note that in the Standard Model, the masses are typically generated through Yukawa interactions with the Higgs field. The absence of direct Yukawa interactions in the above mass term for the Vector-Like Quark is what makes it "vector-like."

The full Lagrangian for the Vector-Like Quark, without the Yukawa interaction with the Higgs field, would then include kinetic terms and any other relevant interactions:

$$\mathcal{L}_Q = \bar{Q}(i\gamma^\mu \partial_\mu - M_Q)Q + \text{other terms} \tag{H.2}$$

Here, $\mathcal{L}_Q$ represents the full Lagrangian for the Vector-Like Quark Q.

It's important to note that the absence of direct Yukawa interactions with the Higgs field means that the Vector-Like Quark does not directly contribute to the electroweak symmetry breaking, which is the mechanism responsible for generating masses for the Standard Model fermions.

This kind of mass term is common in models beyond the Standard Model where new particles might be introduced with different mass generation mechanisms. The specific details of such models can vary, and the above representation is a simplified example.

I Group Theory for Particle Physics

Definition of Group Theory

Group theory is a powerful tool that allows us to look at "objects" that belong to a particular group, then extend the properties (and symmetries) of that group to other "objects" that belong to that same group.

A group in mathematics is a set equipped with a binary operation (usually denoted as $*$) that satisfies four fundamental properties:

1. **Closure:** If a and b are elements in the group, then $a * b$ is also in the group.

2. **Associativity:** The operation is associative, meaning $(a * b) * c = a * (b * c)$ for all elements a, b, c in the group.

3. **Identity Element:** There exists an identity element e such that $a * e = e * a = a$ for all elements a in the group.

4. **Inverse Element:** For every element a in the group, there exists an inverse element a^{-1} such that $a * a^{-1} = a^{-1} * a = e$, where e is the identity element.

As an example, let us consider the set of integers $\mathbb{Z}$ under addition. This forms a group because:

1. **Closure:** The sum of any two integers is still an integer.

2. **Associativity:** Addition is associative.

3. **Identity Element:** The identity element is 0 since $a + 0 = 0 + a = a$ for any integer a.

4. **Inverse Element:** The inverse of an integer a is $-a$, as $a + (-a) = (-a) + a = 0$.

Lie Groups in Particle Physics

In the context of group theory and its application to particle physics, a **Lie group** is a mathematical object that combines the structure of a group with the smoothness of a manifold.

1. **Group Structure:** A Lie group is a group, satisfying the four fundamental properties: closure, associativity, identity element, and inverse element.

2. **Manifold Structure:** A Lie group is also a smooth manifold, resembling Euclidean space locally.

Lie Group Definition

A Lie group is a set G equipped with a group operation $(\cdot)$ that is also a smooth manifold, such that the group operations and the inverse operation are smooth functions on the manifold.

Example: SU(2) - Special Unitary Group of Degree 2

An example of a Lie group relevant to particle physics is $SU(2)$, the Special Unitary Group of Degree 2. $SU(2)$ is a group of 2×2 complex matrices with unit determinant. Its elements are parameterized by three real numbers, and it forms a three-dimensional Lie group.

In the context of the Standard Model, $SU(2)$ is part of the electroweak symmetry group $(SU(2) \times U(1))$ governing the weak force and electromagnetic force.

The SM Lagrangian

Within group theory, there can be many representations of a certain group. For instance, if we think of a triangle that can be rotated by 120 degrees and appear the same, this is a visual representation of the group D3. This does not mean that this is the only representation of D3. We use group theory in particle physics because we know that the SM Lagrangian is a representation that respects 3 group symmetries, $SU(3)_{\text{color-charge}} \times SU(2)_{\text{weak isospin}} \times U(1)_{\text{hyper-charge}}$, until the higgs mechanism spontaneously breaks the $SU(2)$ symmetry. This means that in the "space" of these groups, you can apply the "rotations" to the Lagrangian without changing the physics of the universe.

Let's focus on the symmetries of the standard model before the $SU(2)$ breaking: The Standard Model Lagrangian is based on principles of gauge symmetry, with associated groups $SU(3)_C$ for Quantum Chromodynamics (QCD), $SU(2)_L$ for weak isospin, and $U(1)_Y$ for hypercharge as mentioned above, but listed more succinctly here for clarity.

$SU(3)_C$ **- Color Symmetry (Quantum Chromodynamics)**

- **Group Structure:** $SU(3)_C$ is the group of special unitary matrices of order 3 with a determinant of 1.

- **Representation:** Associated with the "color charge" carried by quarks (red, green, and blue).

- **Confinement:** Exhibits color confinement; quarks and gluons exist only within color-neutral combinations (hadrons).

$SU(2)_L$ **- Weak Isospin Symmetry**

- **Group Structure:** $SU(2)_L$ is the group of special unitary 2x2 matrices with a determinant of 1.
- **Representation:** Associated with weak isospin, involving left-handed components of fermions (doublets).
- **Weak Force:** Mediates the weak force through W and Z bosons, affecting only left-handed particles in the electroweak theory.

$U(1)_Y$ **- Hypercharge Symmetry**

- **Group Structure:** $U(1)_Y$ is the group of unitary 1x1 matrices (complex numbers with magnitude 1).
- **Representation:** Associated with hypercharge, a combination of weak hypercharge and weak isospin.
- **Electric Charge:** The electric charge is related to hypercharge and weak isospin through the Gell-Mann–Nishijima formula.
- **Electromagnetic Force:** Mediates the electromagnetic force through the exchange of the massless photon (γ).

Let's consider a simple example of an SU(3) rotation for a quark field in the QCD part of the Standard Model Lagrangian. The QCD Lagrangian for a single quark flavor (q) is given by:

$$\mathcal{L}_{\text{QCD}} = \bar{q}(i\gamma^\mu D_\mu - m)q - \frac{1}{4}G^a_{\mu\nu}G^{a\mu\nu} \tag{I.1}$$

where:

- $\bar{q}$ is the quark field.
- D_μ is the covariant derivative.
- m is the quark mass.
- $G^a_{\mu\nu}$ is the gluon field strength tensor.

Now, let's perform an SU(3) rotation on the quark field:

$$q'(x) \to Uq(x) \tag{I.2}$$

where U is an SU(3) matrix representing the rotation in color space.

For simplicity, let's consider a specific SU(3) matrix, which is an element of the group SU(3):

$$U = \begin{pmatrix} e^{i\theta} & 0 & 0 \\ 0 & e^{i\phi} & 0 \\ 0 & 0 & e^{-i(\theta+\phi)} \end{pmatrix} \tag{I.3}$$

This is a valid SU(3) matrix because the determinant is 1, and it represents a rotation in the complex color space. Now, substitute $q'(x)$ and U into the Lagrangian and show that it remains invariant:

$$\mathcal{L}'_{\text{QCD}} = \bar{q}'(i\gamma^\mu D_\mu - m)q' - \frac{1}{4}G'^a_{\mu\nu}G'^{a\mu\nu} \tag{I.4}$$

Substitute $q'(x) \to Uq(x)$ into the Lagrangian and simplify:

$$\mathcal{L}'_{\text{QCD}} = \bar{U}\bar{q}(i\gamma^\mu D_\mu - m)Uq - \frac{1}{4}G'^a_{\mu\nu}G'^{a\mu\nu} \tag{I.5}$$

After performing the calculations it is shown that $\mathcal{L}_{\text{QCD}}$ and $\mathcal{L}'_{\text{QCD}}$ are equivalent.

This is a simplified example, and actual SU(3) rotations can involve more complex matrices. The specific choice of U and the details of the calculation can vary, but the key idea is to demonstrate the invariance of the QCD Lagrangian under SU(3) rotations of the quark field.

Symmetry Breaking

After the spontaneous breaking of the electroweak symmetry through the Higgs mechanism, the symmetry that remains unbroken is the electromagnetic $U(1)_Q$ symmetry. This remaining symmetry corresponds to the electromagnetic force, mediated by the massless photon (γ).

To summarize:

1. **Initial Symmetry:** The electroweak symmetry is initially described by the group $SU(2)_L \times U(1)_Y$.

2. **Spontaneous Symmetry Breaking:** The ground state of the system, determined by the Higgs field's non-zero vacuum expectation value (VEV), breaks the $SU(2)_L \times U(1)_Y$ symmetry spontaneously.

3. **Remaining Symmetry:** The electromagnetic force remains described by the unbroken $U(1)_Q$ symmetry, where Q represents electric charge. This symmetry corresponds to the massless photon (γ), which continues to mediate the electromagnetic interactions.

In summary, the spontaneous breaking of the electroweak symmetry leaves the strong force $SU(3)_C$ and electromagnetic $U(1)_Q$ symmetry unbroken, resulting in the manifestation of the electromagnetic force as we observe it in our universe ($U(1)_Q$). The broken $SU(2)_L$ symmetry contributes to the masses of the W and Z bosons, which mediate the weak force.

J Gauge Bosons

Now that the basics of symmetries has been explained in the previous section, we can see how a specific selection in that symmetrical space (or gauge) can be used. In particular physics, a *gauge* refers to a mathematical symmetry principle that is applied to the description of physical fields, such as electromagnetic fields or other fundamental forces. The term "gauge" in this context comes from the idea of a mathematical transformation, known as a gauge transformation, that leaves the physics of the system unchanged. Gauge symmetries are essential for constructing theories that accurately describe the fundamental forces in the Standard Model of particle physics.

As an example, let's look at the electromagnetic potential 4-vector is given by:

$$A_\mu = (\phi, \mathbf{A}) \tag{J.1}$$

where ϕ is the scalar potential and $\mathbf{A}$ is the vector potential. The field strength tensor $F_{\mu\nu}$ is defined as the antisymmetric derivative of the electromagnetic potential:

$$F_{\mu\nu} = \partial_\mu A_\nu - \partial_\nu A_\mu. \tag{J.2}$$

Consider a gauge transformation of the electromagnetic potential A_μ given by:

$$A_\mu \to A'_\mu = A_\mu - \partial_\mu \alpha, \tag{J.3}$$

where α is the gauge parameter.

The transformed field strength tensor $F'_{\mu\nu}$ is given by:

$$F'_{\mu\nu} = \partial_\mu A'_\nu - \partial_\nu A'_\mu. \tag{J.4}$$

Substitute the expression for A'_μ into the above equation:

$$F'_{\mu\nu} = \partial_\mu (A_\nu - \partial_\nu \alpha) - \partial_\nu (A_\mu - \partial_\mu \alpha). \tag{J.5}$$

Expand the derivatives:

$$F'_{\mu\nu} = \partial_\mu A_\nu - \partial_\mu (\partial_\nu \alpha) - \partial_\nu A_\mu + \partial_\nu (\partial_\mu \alpha). \tag{J.6}$$

Now, rearrange the terms:

$$F'_{\mu\nu} = F_{\mu\nu} - (\partial_\mu \partial_\nu \alpha - \partial_\nu \partial_\mu \alpha). \tag{J.7}$$

The term in the parentheses is symmetric in μ and ν, so the antisymmetry of the field strength tensor ensures that this term is zero. Therefore:

$$F'_{\mu\nu} = F_{\mu\nu}. \tag{J.8}$$

This demonstrates that under a gauge transformation of the electromagnetic potential A_μ, the field strength tensor $F_{\mu\nu}$ remains unchanged.

Gauge Bosons in the Electroweak Theory

Gauge bosons are particles that mediate the fundamental forces between other particles. In the Standard Model, there are four known fundamental forces: electromagnetism, the weak nuclear force, the strong nuclear force, and gravity (gravity is not described by gauge bosons in the Standard Model, and its mediator is not part of the particle content described by gauge theories in the same way as the other forces).

The gauge bosons associated with the three non-gravitational forces in the Standard Model are:

1. Photon (γ): Mediates the electromagnetic force.

2. W and Z bosons (W^+, W^-, Z^0): Mediate the weak nuclear force.

3. Gluons: Mediate the strong nuclear force.

The term "gauge" in gauge bosons comes from the fact that these particles arise from the gauge symmetries in the theoretical framework used to describe the corresponding forces. The gauge bosons are the force carriers that transmit the interactions between particles that experience the associated force. For example, photons mediate electromagnetic interactions between charged particles.

The formalism extends similarly to quantum chromodynamics (QCD) for the strong force, where gluons are the gauge bosons associated with the SU(3) color symmetry.

In summary, the term "gauge" in particle physics refers to a mathematical symmetry principle, and gauge bosons are particles associated with the mediation of fundamental forces in a way consistent with these gauge symmetries. The name "gauge" reflects the role of these symmetries in the theoretical framework used to describe particle interactions [63, 86].

K Luminosity and Cross Section

Luminosity in the context of the Large Hadron Collider (LHC) refers to the measure of the rate at which particle collisions occur within the accelerator. It is a crucial parameter that characterizes the performance of the LHC and is essential for understanding the efficiency of experiments conducted at this high-energy physics facility.

The luminosity ($\mathcal{L}$) of the LHC is defined as the number of particle interactions per unit time and unit cross-sectional area. Mathematically, it is expressed as:

$$\mathcal{L} = \frac{N}{A \cdot t} \tag{K.1}$$

where N is the number of collisions, A is the cross-sectional area of the colliding beams, and t is the time over which collisions are recorded. In the case of the LHC, the luminosity is typically measured in inverse femtobarns fb^{-1}; where $1\,\mathrm{fb} = 10^{-43}\,\mathrm{m}^2$).

The intensity of the particle beams circulating in the LHC is directly related to luminosity. The intensity refers to the number of particles per unit length of the beam, and the luminosity can be increased by enhancing the intensity of the colliding beams. The relationship between luminosity and intensity is given by:

$$\mathcal{L} = f \cdot n_1 \cdot n_2 \tag{K.2}$$

where f is the revolution frequency of the beams and n_1 and n_2 are the number densities of particles in the two colliding beams. This relationship highlights that luminosity can be increased by increasing the number of particles in the beams or by increasing the frequency of collisions.

Several factors contribute to achieving high luminosity in the LHC. One crucial factor is the use of powerful superconducting magnets to focus and steer the particle beams, minimizing their divergence and maximizing the probability of collisions. Additionally, advanced beam optics and sophisticated beam control systems are employed to maintain stable and dense beams during collisions.

Cross section (σ) is a fundamental quantity that describes the likelihood of a particular process occurring during a collision between particles. It represents the effective area for an interaction to take place and is typically measured in units of area, such as barns or femtobarns.

The formula for the number of expected events (N) in a particle physics experiment is given by:

$$N = \sigma \cdot \mathcal{L} \tag{K.3}$$

where σ is the cross section and $\mathcal{L}$ is the integrated luminosity. This formula expresses that the number of events is proportional to the cross section and the integrated luminosity.

Integrated luminosity ($\mathcal{L}$) is a measure of the total number of potential interactions that could occur during the experiment. It is calculated by integrating the instantaneous luminosity over time:

$$\mathcal{L} = \int L \, dt \tag{K.4}$$

Here, L is the instantaneous luminosity, which represents the rate of events per unit cross-sectional area and time. The integral captures the cumulative effect of the luminosity over the entire duration of data-taking.

The Large Hadron Collider (LHC) uses the integrated luminosity and cross section to predict the number of expected events in its experiments. As the collider accumulates integrated luminosity over time, the researchers can use this information along with the known or measured cross section for specific processes to estimate the total number of events expected to be observed.

L Detector Terms

- Parton: A parton is a constituent partile of a hadron, either a quark or gluon. In the early stages of high-energy collisions, such as those in the ATLAS detector, these partons are the primary objects involved in the interactions.

- Parton Distribution Function (PDF): This function describes the probability of finding a parton within a proton, depending on its momentum fraction and the energy scale of the interaction. PDFs are crucial for predicting the results of pp collisions in the LHC.

- Tracks: Tracks refer to the paths traced by charged particles as they move through the detector's magnetic field. These tracks are reconstructed from the signals in the tracking detectors and are used to identify and measure the momentum of particles.

- Showers: Showers are cascades of secondary particles produced when a high-energy particle (like an electron, photon, or hadron) interacts with the material in the detector. Electromagnetic showers are caused by electrons and photons, while hadronic showers are caused by hadrons.

- Parton Showers: These are sequences of branching processes that partons (quarks and gluons) undergo before they turn into hadrons. Parton showers involve the emission of additional partons.

- Hadronization: This is the process by which partons (quarks and gluons) transform into hadrons. This occurs because quarks and gluons are confined within hadrons due to the nature strong force becoming stronger at longer distances.

- Jets: Jets are narrow cones of particles produced by the hadronization of quarks and gluons that were initially produced in high-energy processes. In detectors like ATLAS, these jets are observed as clusters of detected particles.

- Scale Uncertainties: In particle physics, scale uncertainties are related to the theoretical predictions of processes at different energy scales. These uncertainties arise due to limitations in our ability to calculate quantum chromodynamics (QCD) pertubitive terms.

- Detector Response: This term refers to how the ATLAS detector reacts to and records the various particles produced in high-energy collisions. Many calibrations are needed in order to compensate for the fact that the detector is not perfect.

- Truth Information: This refers to the parts of the collision that we can know for the MC samples, but not data. An example would be the exact momentum of the t quark before it's decay, or the COM frame from the PDF.

M Event Reconstruction

In the LHC, particles resulting from *pp* collisions are detected by the ATLAS detector. These particles create distinct signatures as they move through various subsystems of the detector. To analyze these events for physics research, the raw data, which consists of digitized signals from these collisions, must be transformed into a precise representation of the physical particles involved. This transformation is done using a series of algorithms known as event reconstruction. The process starts with low-level data, like clusters from calorimeter energy deposits and tracks from the ID, and progresses to identifying high-level physics objects such as electrons, photons, muons, and jets. Each type of particle generates a unique signature in ATLAS by combining information from tracking and calorimeter systems. Additionally, missing transverse momentum, a crucial factor in detecting non-interacting particles, is calculated. The subsequent sections detail the tracking, vertexing, and reconstruction methods for these particles, with particular emphasis on charged particle track reconstruction in the ID.

Tracks and Vertices

In the ATLAS experiment, tracking charged particles is complex, especially in proton-proton collisions at a center-of-mass energy of $\sqrt{s} = 13\,\text{TeV}$. Each collision typically generates around 15 charged particles, leading to approximately 500 particles per bunch crossing, given the 34 simultaneous interactions during Run 2 [79]. Efficient track reconstruction while minimizing false tracks due to random hits in the ID is crucial. Accurately identifying pp interaction points is essential for differentiating the primary event from multiple pile-up interactions, achieved through track clustering for vertex reconstruction.

Tracking in ATLAS involves fitting hits in the ID to a parametrized helical trajectory of a charged particle in a magnetic field. In an ideal homogeneous field without material interactions, this trajectory is a helix parallel to the field. The trajectory is described by five parameters at the perigee (see Figure 67):

$$\tau = (d_0, z_0, \phi_0, \theta_0, q/p) \tag{M.1}$$

where d_0 and z_0 are transverse and longitudinal impact parameters, ϕ_0 and θ_0 the azimuthal and polar angles, and q/p the charge-to-momentum ratio.

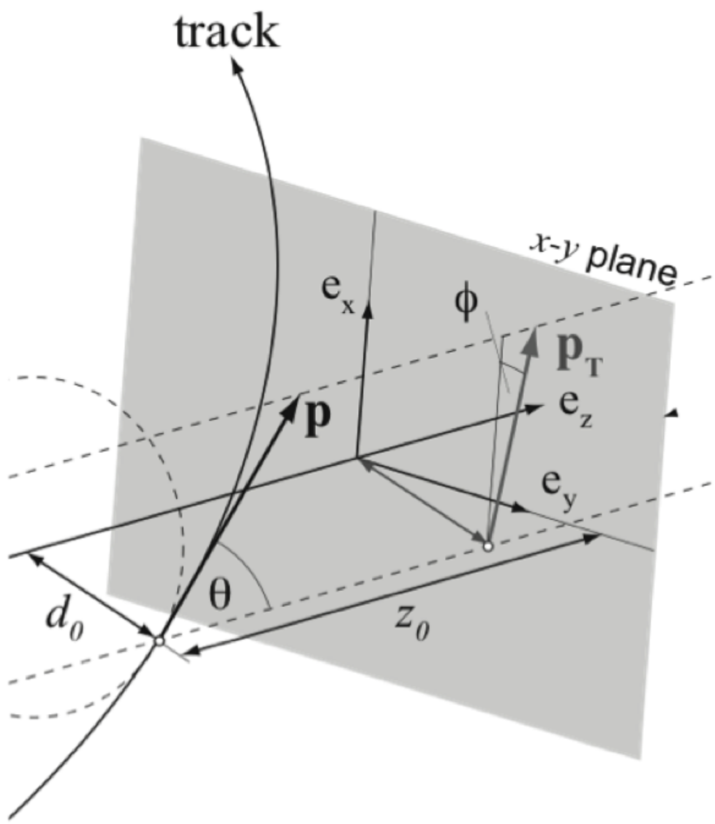

Figure 67: Track parameters at the perigee with respect to the detector origin [79].

Deviations from this ideal path due to magnetic field inhomogeneities and particle-material interactions are accounted for by tracking algorithms.

The subsequent subsections focus on standard tracking and vertexing procedures in ATLAS, including track representation parameters. Standard tracking, optimized for particles from the collision point, is inadequate for massive long-lived particles (LLPs) that do not point back to this point. These LLPs, predicted by BSM theories, require specialized event reconstruction with Large Radius Tracking (LRT) and secondary vertexing algorithms. For the purposes of this paper, primary tracks and vertexing will be considered.

Track Reconstruction

Tracking of charged particles involves two main approaches: inside-out and outside-in tracking [52]. The process starts with the inside-out tracking, which begins in the silicon detectors and extends into the TRT, optimized for primary tracks from *pp* interactions. Conversely, the outside-in tracking starts in the TRT and moves into the silicon detectors, targeting secondary particles like electrons from photon conversions or b-hadron decays. Both methods presuppose that the tracks originate from the collision point.

Inside-out Tracking

There are several substeps:

Spacepoint Creation: Hits in the silicon detectors are transformed into 3D spacepoints, representing intersections of charged particles with detector layers. For the IBL and Pixel detector, hits directly correlate with spacepoints, while in the SCT, stereo-angle information is used for spacepoint construction.

Track Seeding: Initial seeds are identified from triplets of hits in silicon layers, assuming a perfect helical trajectory. These seeds form the basis for further track construction.

Track Candidate Building: Employing a combinatorial Kalman filter [58, 45], track candidates are developed by adding hits that align with the predicted trajectory. The process iteratively refines track parameters through detector layers, culminating in a global least-squares fit.

Ambiguity Solving: A scoring algorithm assesses track candidates, favoring tracks with unshared hits and penalizing for shared hits or holes. Tracks exceeding a certain score are accepted.

Track Extension: Tracks are extended into the TRT, integrating compatible hits and refined through a final global fit.

Outside-in Tracking

This method builds on the inside-out approach, using remaining hits and TRT segments. It follows a similar process of Kalman filtering, ambiguity resolution, and final fitting, particularly focusing on calorimeter-seeded regions.

Primary Vertex Reconstruction

The process for reconstructing primary vertices involves using the tracks established earlier to locate the spatial points of pp interactions. These interaction points, or primary vertices, are identified by pinpointing where at least two tracks intersect near the beam axis. This identification is carried out through an iterative method [18]. Additionally, only those tracks that meet certain quality criteria related to hit multiplicities in the Inner Detector layers [12] are considered for vertex construction. The primary vertex reconstruction procedure is characterized by several steps, starting with the selection of a seed position and followed by an adaptive fitting process to refine the vertex position. This process is repeated until all relevant tracks are utilized or no further vertices can be detected.

1. **Vertex Seed Selection:** The initial seed for the first vertex is set based on the detector origin and the peak of the z_0-distribution of tracks.

2. **Vertex Position Fitting:** An adaptive vertex fitter [59], using a least-squares approach, iteratively refines the vertex position, down-weighting incompatible tracks.

3. **Track Exclusion and Vertex Finalization:** Incompatible tracks are excluded for each vertex, repeating the process until all tracks are utilized or no new vertex is found.

4. **Vertex Information Output:** The output includes 3D vertex positions and covariance matrices, with the primary vertex (PV) identified by the highest sum of track p_T.

The vertex reconstruction algorithm's output comprises sets of three-dimensional vertex positions and their respective covariance matrices. The event's Primary Vertex (PV) is defined as the one with the maximum sum of the transverse momentum (p_T) of its associated tracks. This distinction is crucial for distinguishing the main hard interaction from other pileup interactions in the analysis.

Once the primary vertices are determined, they facilitate the identification of the beamspot, which indicates the region of pp interactions within the detector. The beamspot's characterization involves an unbinned maximum-likelihood fit to the spatial distribution of primary vertices, gathered from numerous events [59]. This process is conducted periodically during data collection, typically every two minutes [8]. The beamspot's center serves as an additional reference in the primary vertex fit, aiding in constraining the transverse position. Moreover, all track parameters are recalculated with the beamspot as the reference point.

Object Reconstruction

Electrons and Photons

Electron and photon identification and reconstruction involve integrated data from the ID and the EM calorimeter [26]. Electrons typically leave tracks in the ID and deposit their entire energy in the calorimeter, whereas photons, being neutral, only produce showers in the calorimeter. The process accounts for electron energy losses through Bremsstrahlung and potential photon conversions into electron-positron pairs in the ID.

Reconstruction starts with identifying energy clusters [19] in the calorimeter, which then guide a specialized tracking process considering an electron's higher energy loss compared to a default pion. Clusters are matched with ID tracks based on position and momentum. Clusters linked to two tracks forming a conversion vertex are identified as converted photons, while those without associated tracks are considered unconverted photons.

Central electron p_T is gauged from both calorimeter energy and track measurements, with angular coordinates derived from the track. In the forward region lacking ID coverage, electron energy is less precisely determined, and cluster centers provide angular coordinates.

Each electron candidate undergoes a quality assessment using a likelihood algorithm, classifying them into categories like Loose, Medium, or Tight, based on different criteria affecting purity and identification efficiency [13]. Photons receive similar classification.

Additionally, isolation requirements help differentiate signal electrons from backgrounds, like those from hadron decays, by evaluating the energy of surrounding particles. This helps in identifying promptly produced electrons and distinguishing them from others embedded in jets or arising from converted photons.

Muons

Muons typically leave tracks in the ID, small energy deposits in the calorimeters, and tracks in the Muon Spectrometer. The primary method for muon reconstruction, *combined muons*, involves matching tracks from the Muon Spectrometer with ID tracks. These tracks are initially reconstructed separately in both systems before being combined through an overall fit.

Additionally, ATLAS utilizes other muon types:

- **Stand-alone muons:** Created from Muon Spectrometer tracks extrapolated to the beam line, accounting for energy losses and multiple scattering in the calorimeters. This is primarily used in the $2.5 < |\eta| < 2.7$ region where ID coverage is absent.

- **Segment-tagged muons:** Start from ID tracks and look for matching segments in the first Muon Spectrometer layer. This type recovers inefficiencies for low-p_T muons that may not reach all layers of the Muon Spectrometer.

- **Calorimeter-tagged muons:** Formed from ID tracks matched to compatible calorimeter energy deposits, particularly in very central $|\eta|$ regions lacking Muon Spectrometer coverage.

Muons are also categorized based on quality and isolation into Loose, Medium, Tight, and High-p_T classifications [14]. Key variables for discrimination include the q/p significance, which evaluates the consistency between ID and Muon Spectrometer momentum measurements, and the χ^2 of the combined fit. The Medium selection is the standard for central regions and is complemented by stand-alone muons above $|\eta| = 2.5$.

Jets

A jet is recognized as a focused stream of particles, a byproduct of quark or gluon hadronization, notable for substantial energy deposits in the calorimeters. There are various algorithms for assembling these energy deposits into jets, each influencing the jet's final characteristics. ATLAS primarily uses the anti-k_t algorithm for jet reconstruction [49], known for its infrared safety — ensuring stability against additional soft radiation — and collinear safety, which guarantees the incorporation of divided partons into the jet.

The anti-k_T algorithm starts with clusters that are connected in the EM and hadronic calorimeters. The clusters are then merged into jets by considering their separation and transverse momonta. The separation parameter is defined as:

$$d_{ij} = \min(p_{T,i}^{-2}, p_{T,j}^{-2}) \frac{\Delta R_{ij}^2}{D^2} \tag{M.2}$$

Here, $p_{T,i}$ and $p_{T,j}$ are the transverse momenta of the 2 associated clusters, ΔR_{ij} is there separation and D is the distance parameter.

The anti-k_T algorithm starts with the cluster with the highest p_T as cluster seed i, then calculates d_{ij}, where j is the next closest cluster. This is then compared to the distance to the beam axis, which is given by:

$$d_{iB} = p_{T,i}^{-2} \tag{M.3}$$

If the distance d_{ij} is smaller than the distance d_{iB}, the two clusters are merged into a new one, which becomes the new seed. Otherwise, the seed i is classified as a jet, and its associated clusters are removed from consideration. This process is repeated until all clusters are assigned to a jet. The anti-kt algorithm, with its inverse p_T dependence, typically produces jets that are conical, featuring energetic cores and softer edges. The parameter D, defining the cone size and minimum jet separation, is commonly set to 0.4.

Jet energies in ATLAS are measured from calorimeter energy deposits and require calibration for various experimental effects [28, 16], including energy losses in inactive detector areas, jet energy leakage, and pileup interactions. A multi-step calibration, involving correction factors from both simulations and data, is applied. The Jet Vertex Tagger (JVT) algorithm evaluates the likelihood of jets being due to pileup interactions [10], based on track origins. Additionally, b-tagging is used to identify jets containing b-hadrons, utilizing their significant decay length for secondary vertex reconstruction.

Missing Transverse Momentum

Note: It is common to write Missing Transverse Energy (MET) in place of missing transvers momentum. This is due to the likeness of momentum to energy in the severe relativistic limit...although it is not accurate, expecially with directional vector notation...this explaination will use p_T rather than energy E.

Missing transverse momentum ($\vec{p}_{\mathrm{T}}^{\mathrm{miss}}$) is used to infer the presence of undetected particles. It is defined as the negative vector sum of the transverse momenta (p_{T}) of all reconstructed particles and detector energy deposits in an event:

$$\vec{p}_{\mathrm{T}}^{\mathrm{miss}} = -\left(\sum \vec{p}_{\mathrm{T}}^{\mathrm{jet}} + \sum \vec{p}_{\mathrm{T}}^{\mathrm{electron}} + \sum \vec{p}_{\mathrm{T}}^{\mathrm{muon}} + \sum \vec{p}_{\mathrm{T}}^{\mathrm{photon}} + \sum \vec{p}_{\mathrm{T}}^{\mathrm{soft}}\right) \tag{M.4}$$

The term $\vec{p}_{\mathrm{T}}^{\mathrm{soft}}$ includes all energy deposits not associated with the reconstructed jets, electrons, muons, and photons. The principle is that since interacting partons in a pp collision have negligible transverse momentum, any detected missing transverse momentum suggests the presence of invisible particles. The soft term can be calculated from either calorimeter or track measurements, with the magnitude of the missing transverse momentum vector denoted by ($\vec{p}_{\mathrm{T}}^{\mathrm{miss}}$).

Overlap Removal

In the ATLAS experiment's object reconstruction, energy deposits and tracks might be shared between different particles and jets, risking double counting. To address this, an overlap removal process is employed to determine and eliminate overlapping objects. This process is vital for maintaining accurate counts and is executed on baseline objects, which are subject to looser selections than the final objects used in analyses. The process includes specific steps for handling overlaps between different types of objects, such as between electrons and muons, electrons and jets, muons and jets, and between photons and other objects or jets. The criteria for removal are based on the spatial proximity measured by the delta R (ΔR) parameter and, in some cases, involve additional considerations like b-tagging for jets near electrons.

Overlap removal is crucial to avoid double counting of shared calorimeter energy deposits and tracks. The process, applied to baseline objects, involves:

- **Electron-Muon Overlap:** Electrons sharing an ID track with a muon are removed.
- **Electron-Jet Overlap:** Jets within $\Delta R = 0.2$ of an electron are discarded, unless b-tagged, in which case the electron is removed. Remaining electrons within $\Delta R < \min(0.04 + \frac{10\,GeV}{p_T}, 0.4)$ of a jet are also removed.
- **Muon-Jet Overlap:** Treated identically to Electron-Jet.

- **Photon Overlaps:** Photons within $\Delta R = 0.4$ of baseline electrons or muons, and jets within $\Delta R = 0.4$ of remaining photons, are removed.

N Uncertainty

Statistical Uncertainties

Introduction to Statistical Uncertainties

Statistical uncertainties, also known as random uncertainties, arise from the inherent variability in data and measurements. They are caused by factors that vary randomly from one measurement to the next, such as fluctuation in experimental conditions, instrumental precision, or sampling methods. Understanding and quantifying these uncertainties are crucial for accurate data interpretation and reliable conclusions.

Common Distributions for Modeling Statistical Uncertainties

Statistical uncertainties are often modeled using probability distributions, which describe how the values of a random variable are distributed. Two of the most common distributions are:

Gaussian Distribution

The Gaussian or normal distribution is a continuous probability distribution characterized by its mean (average value) and standard deviation (a measure of spread). It is mathematically represented as:

$$P(x|\mu,\sigma) = \frac{1}{\sqrt{2\pi\sigma^2}} e^{-\frac{(x-\mu)^2}{2\sigma^2}} \tag{N.1}$$

where x is the variable, μ is the mean, and σ is the standard deviation. This distribution is symmetrical and describes many natural phenomena, especially those that are the result of many small, independent effects.

Poisson Distribution

The Poisson distribution is a discrete probability distribution that expresses the probability of a given number of events occurring in a fixed interval of time or space. It is defined as:

$$P(k|\lambda) = \frac{\lambda^k e^{-\lambda}}{k!} \tag{N.2}$$

where k is the number of occurrences and λ is the average number of occurrences. This distribution is particularly useful in processes that count occurrences, such as radioactive decay or arrival of customers at a store.

Systematic Uncertainties

Introduction to Systematic Uncertainties

Systematic uncertainties, in contrast to statistical uncertainties, arise from biases in measurements or analysis. These are not random and cannot be reduced by increasing the sample size. They may result from calibration errors, environmental conditions, theoretical models, or data processing biases. Identifying and quantifying systematic uncertainties are often more challenging than statistical uncertainties but are essential for the integrity of the results.

Challenges in Quantifying Systematic Uncertainties

Quantifying systematic uncertainties requires a deep understanding of the measurement process and the theoretical models involved. It often involves estimating the effects of various sources of bias and how they propagate through the analysis. Systematic uncertainties can be correlated, making their combined effect non-trivial to estimate.

Examples in the ATLAS experiment

The ATLAS experiment encounters various sources of systematic uncertainties due to limitations in measurement capabilities, theoretical models, and experimental setup. Some common examples include:

1. **Detector Calibration and Resolution**: Uncertainties in the calibration of detector components, such as the electromagnetic calorimeter or the muon spectrometer, affect energy scale, energy resolution, and momentum resolution.

2. **Luminosity Measurement**: The uncertainty in the measurement of luminosity, which quantifies the number of particles colliding per unit area per unit time, impacts the cross-section measurements.

3. **Background Estimation**: Accurate estimation of backgrounds, such as known Standard Model processes, is crucial. Misestimation leads to systematic errors.

4. **Monte Carlo Simulations**: Systematic uncertainties arise from the choice of models, parameters in simulations, and limitations of the simulation methods.

5. **Particle Identification and Reconstruction**: Uncertainties in the efficiency of identifying and reconstructing particles like electrons, muons, jets, or missing transverse energy contribute to systematic errors.

6. **Pile-up Effects**: Estimating and correcting for pile-up, referring to multiple proton-proton collisions, introduces systematic uncertainties.

7. **Theoretical Uncertainties**: These include uncertainties in cross-section calculations, parton distribution functions, and higher-order QCD corrections.

8. **Beam Conditions and Alignment**: Variations in beam conditions, such as beam energy and alignment of beamline components, can introduce systematic uncertainties.

Each of these uncertainties is carefully estimated and accounted for in the data analysis to ensure the reliability and accuracy of the results.

Incorporating Systematic Uncertainties in Models

Nuisance Parameters

Nuisance parameters are variables in a statistical model that are not of direct interest but must be accounted for in the analysis. In the context of systematic uncertainties, these parameters represent sources of bias or variation that affect the primary measurements.

Profile Likelihood Method

The profile likelihood method is a technique used to incorporate nuisance parameters into the analysis, see appendix O. It involves maximizing the likelihood function over the nuisance parameters to obtain a profile likelihood function that depends only on the parameters of interest. Mathematically, the profile likelihood function for a parameter of interest θ is:

$$\mathcal{L}(\theta, \phi) = L(\theta, \hat{\hat{\phi}}(\theta)) \tag{N.3}$$

where ϕ represents the nuisance parameters. The double hat notation $\hat{\hat{\phi}}$ indicates that the nuisance parameters are estimated for each fixed value of θ.

Maximization of the Likelihood Function

In this approach, the likelihood function is maximized with respect to the nuisance parameters for fixed values of the parameters of interest. This process effectively “profiles out” the nuisance parameters, leading to a likelihood function that is a function of the parameters of interest alone.

Importance in Statistical Analysis

This method is particularly important in complex analyses where several systematic effects need to be accounted for. It allows for a more accurate estimation of the parameters of interest and provides a way to quantify the impact of systematic uncertainties on the final results.

O Profile Likelihood Fitting

The Likelihood Function and Its Components

The likelihood function in high energy particle physics is essential for quantifying how well a theoretical model with a specific set of parameters explains observed experimental data. The full likelihood function, denoted as $L(\theta)$, encompasses both the parameter of interest, μ, and the nuisance parameters, ν, that account for systematic uncertainties. It is represented as

$$L(\theta) = L(\mu, \nu). \tag{O.1}$$

In practical applications, analysts often work with the negative log-likelihood, $-\ln L(\theta)$, because minimizing this function is mathematically equivalent to maximizing the likelihood. This approach simplifies the calculations, particularly in complex analyses involving numerous parameters [89].

Minimization and Nuisance Parameters

The minimization of the negative log-likelihood is a key step in determining the values of the parameters that best fit the data. For a fixed value of the parameter of interest μ, the nuisance parameters ν are adjusted to minimize the negative log-likelihood, yielding the conditional estimate $\hat{\hat{\nu}}(\mu)$. This process leads to the formation of the profile likelihood, defined by fixing μ and optimizing over the nuisance parameters. Mathematically, the profile likelihood for a given μ is expressed as

$$\mathcal{L}_p(\mu) = L(\mu, \hat{\hat{\nu}}(\mu)), \tag{O.2}$$

and in its negative log form as

$$-\ln \mathcal{L}_p(\mu) = -\ln L(\mu, \hat{\hat{\nu}}(\mu)). \tag{O.3}$$

The minimization of the negative log-likelihood is a key step in determining the values of the parameters that best fit the data. For a fixed value of the parameter of interest μ, the nuisance parameters ν are adjusted to minimize the negative log-likelihood, yielding the conditional estimate $\hat{\hat{\nu}}(\mu)$. This process leads to the formation of the profile likelihood, defined by fixing μ and optimizing over the nuisance parameters. Mathematically, the profile likelihood for a given μ is expressed as

$$\mathcal{L}_p(\mu) = L(\mu, \hat{\hat{\nu}}(\mu)), \tag{O.4}$$

and in its negative log form as

$$-\ln \mathcal{L}_p(\mu) = -\ln L(\mu, \hat{\hat{\nu}}(\mu)). \tag{O.5}$$

NLL

In the context of hypothesis testing, the negative log-likelihood becomes particularly relevant when we use the log likelihood ratio. This ratio is a tool for comparing two hypotheses: typically, a null hypothesis H_0 and an alternative hypothesis H_1. The log likelihood ratio is defined as

$$\Lambda = -2 \ln \left(\frac{L(\mu_0, \hat{\nu})}{L(\hat{\mu}, \hat{\nu})} \right), \tag{O.6}$$

where μ_0 is the parameter value under the null hypothesis and $\hat{\mu}$ is the parameter value that maximizes the likelihood under the alternative hypothesis. This ratio measures how much more likely the data is under one hypothesis compared to the other.

The negative sign in the negative log-likelihood and in the log likelihood ratio is essential. It is used because, in many statistical contexts, minimization problems are more standard and often more computationally stable than maximization problems. By converting the likelihood to a negative log-likelihood, we turn a maximization problem into a minimization one, which is more aligned with common optimization algorithms.

In hypothesis testing, smaller values of the log likelihood ratio Λ indicate that the null hypothesis H_0 is less likely compared to the alternative hypothesis H_1. This ratio forms the basis of many statistical tests, such as the likelihood ratio test, and is fundamental in determining the significance of the results, helping to decide whether to reject the null hypothesis in favor of the alternative hypothesis.

This framework allows statisticians and researchers to make informed decisions based on the data, taking into account both the parameter of interest and the nuisance parameters that might affect the outcome [89].

Hypothesis Testing: Signal vs. Background

In high energy physics, hypothesis testing typically involves comparing two scenarios: the null hypothesis (often the background-only hypothesis) and the alternative hypothesis (signal plus background). The likelihood ratio test statistic,

$$\lambda(\mu) = \frac{L(\mu, \hat{\hat{\nu}}(\mu))}{L(\hat{\mu}, \hat{\nu})}, \tag{O.7}$$

where $\hat{\mu}, \hat{\nu}$ maximize the likelihood without constraints, is used for this purpose. The significance of a potential discovery is determined by the deviation of $\lambda(\mu)$ from its expected value under the null hypothesis. A significant deviation suggests that the observed data is unlikely under the null hypothesis, indicating evidence for the alternative hypothesis, such as the discovery of a new particle.

Role of Parameters in Likelihood

In these analyses, the parameter of interest, μ, is the focus, representing the existence or properties of a new particle. The nuisance parameters, ν, are equally important as they represent systematic uncertainties such as detector efficiency and background estimation errors. Proper management of these nuisance parameters is crucial for accurate estimation of μ and for reliable hypothesis testing [89].

P WbX: Studies on the Method of Calculating Limits

Toys Vs. Asymptotic

TRExFitter has the capability to expidite the limit calculation process by using an asymptotic approach. The initial studies were done on the limits with this method, then as the analysis became more mature, we needed to verify this method was returning accurate results. The branching ratio $Wb = 100$ was investigated by generating 1000 toys and comparing the calculated limits at various mass points seen in Figure 68. The conclusion was the asymptotic method was indeed a viable limit calculation tool.

Q WbX: Binning Studies of the Single Top Control Regions

The VLQ pair event reconstruction algorithm assumes two particles with the same mass in the event, like in the case of $t\bar{t}$ and VLQ signal. For other backgrounds, like single top, the invariant mass difference between the two reconstructed VLQs, $\Delta M(VLQ1, VLQ2)$, takes a random value. The $\Delta M(VLQ1, VLQ2)$ values in $t\bar{t}$ background and the VLQ signal events are therefore low, while regions requiring high $\Delta M(VLQ1, VLQ2)$ value are enriched in the important single top background. These regions can be used as single top control regions to

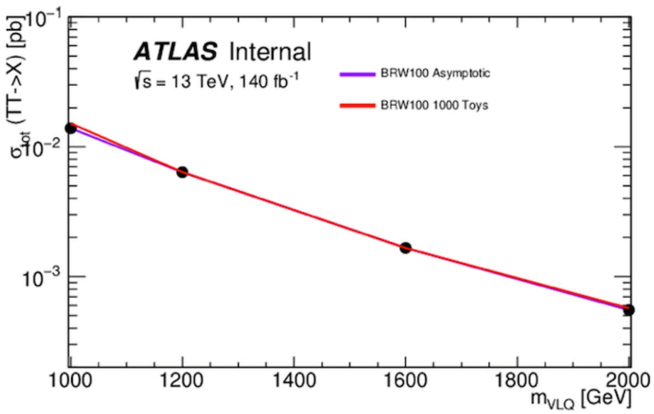

Figure 68: A comparison of the two different methods of calculating sensitivity limits.

constrain the single top modeling and the corresponding nuisance parameters. Two control regions, at low and high event S_T with a cut at $S_T = 1.9$ TeV, trace the evolution of the modeling as a function of the event S_T which has been observed in similar analyses as well. The low S_T single top CR has an expected yield of about 300 events, the high S_T single top CR of about 150 events and are binned in the invariant mass of the reconstructed leptonically decaying VLQ, like the signal regions. Two possible binning options, the "(2,2) sp" and "(2,3)" options are shown in Figures 69 and 70, respectively. The first number in the binning option names indicate the bin number of the low S_T single top CR and the second number the bin number in the high S_T single top CR.

To give the fit more freedom to consider the evolution of the single top modeling as a function of S_T, the single top DS/DR modeling systematic is splitted in a low ("DSDRLow") and a high S_T component ("DSDRHigh"). The following studies assume an equal branching ratio of T to its three possible decay modes.

A high sensitivity on the CR binning has been observed according to Figure 71:

- The higher the pull of DSDRHigh, the higher the single top normalization factor (SF) (Figure 71, right)

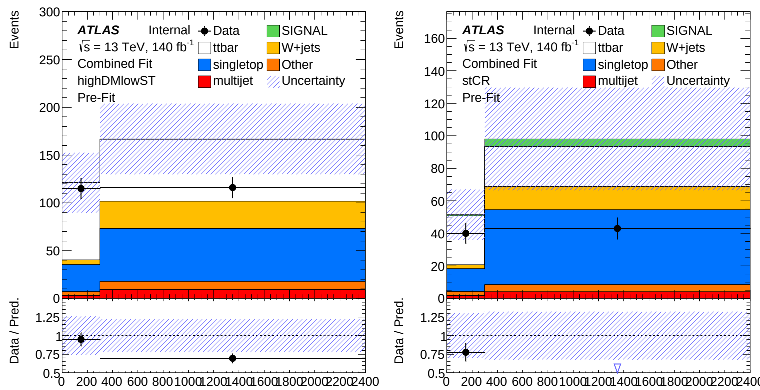

Figure 69: Binning option (2,2) sp. Note that the "sp" is short for "special" to differenciate from another option called "(2,2)". The difference between the options is that the bin edge of (2,2)sp is at $m_{VLQ} = 300\ GeV$ while the first bin is more inclusive in the (2,2) option. The idea is to have a $t\bar{t}$-dominated bin. On the left, the low S_T single top CR is shown, on the right, the high S_T single top CR.

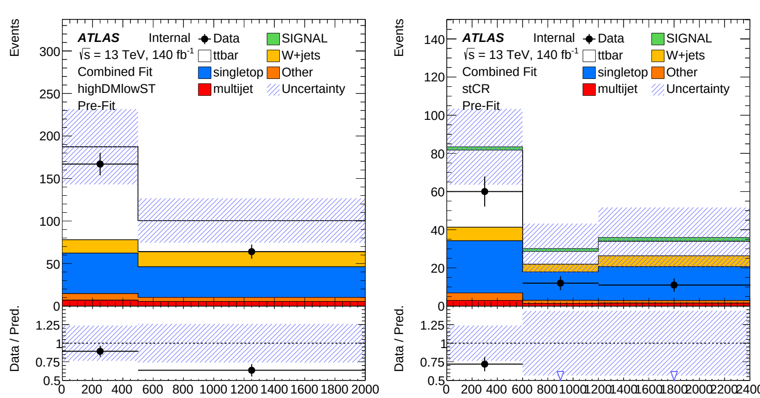

Figure 70: Binning option (2,3). On the left, the low S_T single top CR is shown, on the right, the high S_T single top CR.

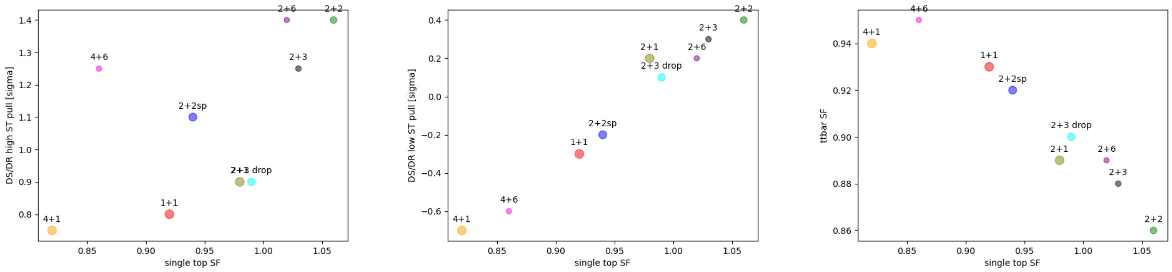

Figure 71: Dependence of the DSDRHigh pull on the single top SF for different binning options (left), dependence of the DSDRLow pull on the single top SF (center) and dependence of the single top SF on the $t\bar{t}$ SF (right). The radius of the data point is proportinal to the fraction of expected data in the highest bin in m_{VLQ} of the high S_T single top CR.

- The higher the pull of DSDRLow, the higher the single top SF (Figure 71, center)
- The higher the single top SF, the lower the $t\bar{t}$ SF (Figure 71, right)

The central single top model is DR and $+1\ \sigma$ indicates that the data is compatible with a DS-like signal model. The higher the DSDR pulls, the more DS-like the single top, the lower the single top contribution. The prediction of a DS-like Wt single top models nearly 100% lower than of a DR-like model for high S_T [1]. The fit determines the single top contribution via the DS/DR nuisance parameters and the single top SF. DS/DR is a large uncertainty and has the power to change significantly the single top yield. Both $t\bar{t}$ and single top are important backgrounds, if one of them increases, the other decreases. Depending on how the binning of the single top CRs is chosen, the SFs and DS/DR nuisance parameters shift and the $t\bar{t}$ and its nuisance parameters compensate in the fit to the data.

A test is done with the high S_T single top CR binned in three bins in the reconstructed m_{VLQ} (binning (2,3)): the last bin of three is dropped and the impact on the parameters in question (DSDRHigh, single top SF and $t\bar{t}$ SF) is observed (light blue data point in Figure 71: last bin dropped, grey data point (2,3) corresponds to the fit to the whole m_{VLQ} spectrum). Dropping that last bin in m_{VLQ} drops 25% of the region statistics, the distribution is cut off at $m_{VLQ} = 1.2$ TeV. The low-statistics tail of a distribution should

[1]Single top Wt DS and DR are shifted in S_T: DR predicts a harder S_T spectrum

not impact the fit significantly and the single top modeling should not depend on m_{VLQ}, a reconstructed variable. The DSDRHigh, single top SF and $t\bar{t}$ SF are however impacted significantly. This gives a hint that statistical fluctuations in distribution tails of the data and the MCs play a role in the interplay DS/DR / single top SF / $t\bar{t}$ SF. It is also observed that the DSDRHigh pull is higher, the less inclusive in m_{VLQ} the last bin, which clearly hint for statistical fluctuations as the reason for the strong parameter shifts. The data point radii in Figure 71 are proportional to the fraction of expected data in the highest bin in m_{VLQ} in the high S_T single top CR. In Figure 71 on the left, it can be seen that data point with small radii (less inclusive high m_{VLQ} bins) are accumulated at high DSDRHigh pulls.

Other observations:

- The DSDRHigh pull depends on the binning of the high S_T single top CR.
- The DSDRLow pull depends on the binning of the low S_T single top CR.
- The value of DSDRLow seems random and ranges from -0.7 σ to +0.4 σ while the value of DSDRHigh is consistently around +1 σ for all fits.

These observations show that the fit uses the shape of the DS/DR nuisance parameter to adjust to fluctuations of the data statistics. That the DS/DR nuisance parameter and the single top SF show correlated behaviour is not surprising as both determone the yield of the single top background and DS/DR is a very large uncertainty which has the power to compensate and change the single top yields significantly. However, the $t\bar{t}$ background yield and the nuisance parameters should be constrained in the high-statistics, high purity $t\bar{t}$ control region. The S_T dependence of the $t\bar{t}$ modeling should have no impact neither as it is taken into account by the $t\bar{t}$ shape correction as a function of S_T. an ideal fit, the $t\bar{t}$ SF should be as close as possible to the result of a $t\bar{t}$ control region only fit. This is an indication that less pulls/compensation of $t\bar{t}$ SF and nuisance parameters is happening. The $t\bar{t}$ SF result of a $t\bar{t}$ CR only fit is used as a “standard candle” to determine the binning of

Parameter	single top SF	$t\bar{t}$ SF
Value	0.93 ± 0.28	0.91 ± 0.13

Table 4: Background normalization factors resulting from a $t\bar{t}$CR only fit.

the single top CR leading to the least compensation of $t\bar{t}$ fit parameters. The post-fit results of the relevant parameters are shown in Table 4.

The binning which results into the most similar $t\bar{t}$ SF is the (2,2)sp binning. Also the single top SF resulting from the $t\bar{t}$ CR only fit is similar to the single top SF of the (2,2)sp binning fit. Interestingly, the $t\bar{t}$ SF takes a value which is close to the value when dropping events with $m_{VLQ} > 1.2$ TeV. This is an indication that statistical fluctuation of the data also the MC lead to the compensation between $t\bar{t}$ and single top SF and nuisance parameters. According to these studies, splitting both single top CRs in two bins, with the binning option "(2,2)sp" is the best option. These studies have been repeated with 100% branching ratio of $T \rightarrow Wb$ and lead to the same conclusion.

R Single VLQ: Reweighting Validation

Upon initial comparison of the data and Monte Carlo (MC) modeling in the control and validation regions for this analysis, it became evident that there existed a notable discrepancy between the predicted outcomes and the observed results, even when taking into account both systematic and statistical uncertainties. Such discrepancies are not uncommon in high-energy searches and were previously observed in the two analyses [3][1] within this particular channel. Various factors can contribute to these disparities, as discussed in [73], including but not limited to:

- Suboptimal detector simulation.
- Insufficient modeling of the hard processes (often calculated only to a finite order).
- Unaccounted cross-sections and branching ratios for specific processes at certain energy levels.

- Altered behavior of certain processes at these high energies.

In practice, a considerable portion of the MC used in nearly all ATLAS analyses undergoes reweighting, with corrections applied to all events by default to address some of the aforementioned issues. These corrections involve the introduction of scale factors, such as those for jet energy scale and pile-up reweighting. While these scale factors can lead to satisfactory agreement in certain regions or observables (typically around well-studied energy regimes, like the W-mass peak), they may have adverse effects in other regions. Given the focus of this analysis on a very high-energy range, it is not unexpected that perfect agreement is challenging to achieve.

In the preceding analysis, a significant disparity between data and MC was also observed and was attributed to the mismodeling of the W+jets background [1]. As outlined in [44], scale factors for the W+jets background were derived by comparing the distribution of the leading b-jet p_T in the pre-selection region. These scale factors were not directly employed to adjust the W+jets samples but were instead incorporated as additional uncertainties in the fitting procedure.

Procedure

The procedure employed in [3] was initially tested for this analysis but was found to be inadequate in this specific case. The procedure from [3] was likely sufficient due to the lower luminosity, which imposed statistical limitations on high m_{VLQ} ranges. However, the increased luminosity in this analysis unveiled a more substantial disagreement. Various reweighting techniques were explored, encompassing different regions and observables. Ultimately, a consensus was reached among all involved parties to implement a two-dimensional reweighting approach for the W+jets, $t\bar{t}$, and single top Wt channel backgrounds, with the latter two being considered as a combined sample for reweighting purposes. Unlike [3], where only one kinematic observable (leading jet p_T) was used, here each sample was reweighted based on the examination of two kinematic observables simultaneously.

For the W+jets background, jet multiplicity versus m_{VLQ} was employed in a W+jets enriched region, created by applying the same selection criteria as the pre-selection region, but with the b-tag requirement on the leading jet removed and a b-jet veto applied. This results in a region with a high purity ($\geq 90\%$) of W+jets events, from which the reweighting scale factors for the W+jets reweighting were derived. Figure 72 illustrates the agreement between data and MC in the W+jets enriched region, from which the W+jets reweighting factors were obtained.

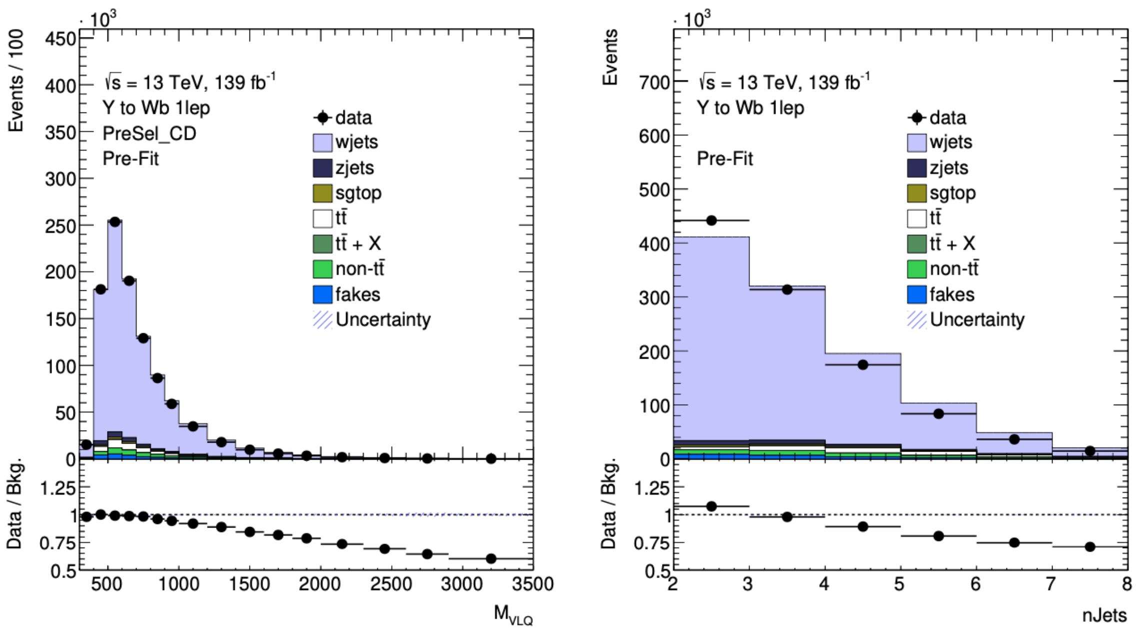

(A) m_{VLQ} in the W+jets enriched region

(B) Jet multiplicity in the W+jets enriched region

Figure 72: The W+jets enriched region used to extract the W+jets reweighting weights

Due to the significant interference between the $t\bar{t}$ and singletop Wt backgrounds, they are treated as a single background for the purpose of reweighting, meaning they share the same scale factors. In the case of $t\bar{t}$ and Wt, leading jet p_T versus W p_T were used as the observables. The W+jets reweighting obtained in the previous step is then applied to the W+jets sample in the analysis pre-selection region. Assuming that the contribution to mismodeling arising from W+jets has been resolved, the remaining mismodeling is attributed mainly to $t\bar{t}$ and single top Wt backgrounds. Figure 73 illustrates the leading jet p_T and W

p_T distributions in the pre-selection region after the W+jets reweighting has been applied but before the reweighting for $t\bar{t}$ and single top Wt backgrounds is performed.

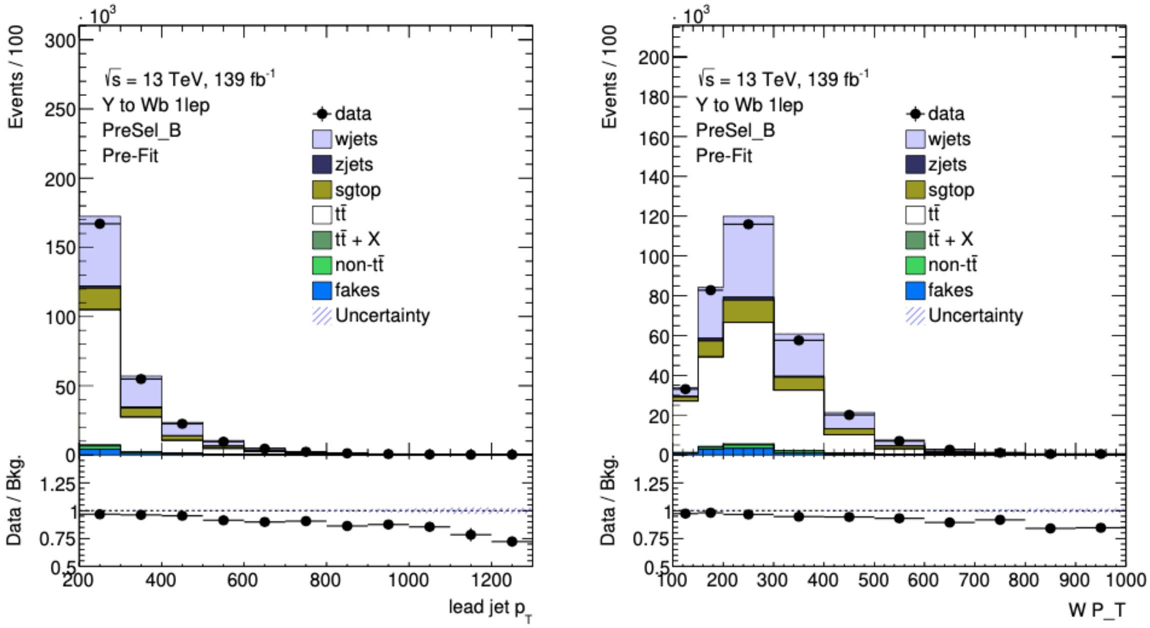

(A) Lead jet p_T in the pre-selection region

(B) W p_T in the pre-selection region

Figure 73: The distributions in the preselection region used to extract the $t\bar{t}$ reweigthing weights

Figure 74 shows the reweighting weights used in the analysis. As can be seen, the weights vary significantly across the range of the observables used.

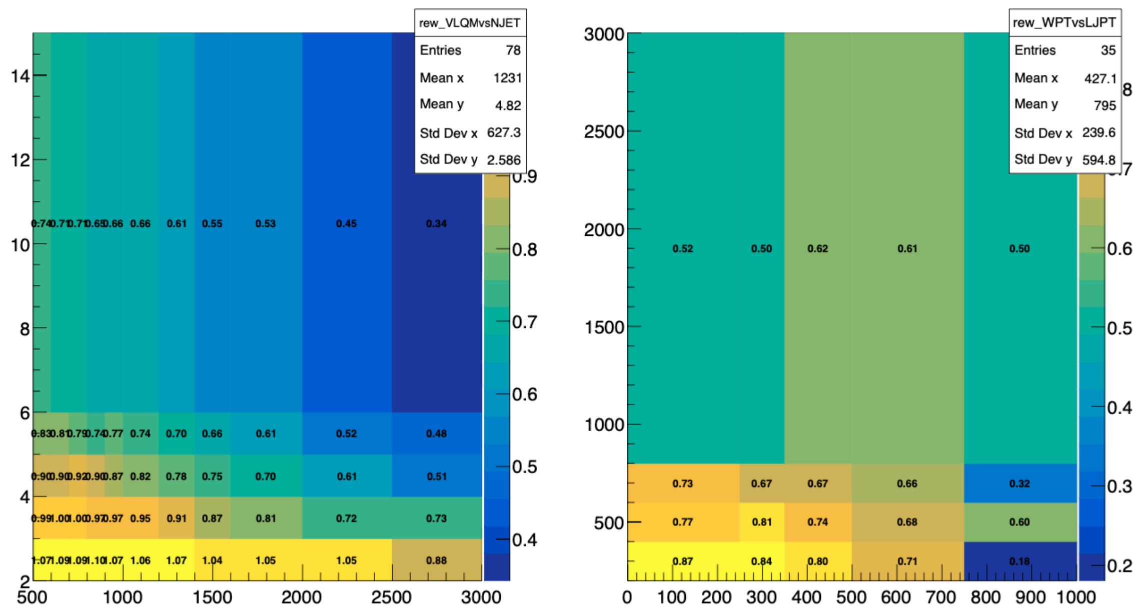

(A) Reweighting weights applied to the W+jets backgrounds.

(B) Reweighting weights applied to the $t\bar{t}/Wt$ backgrounds.

Figure 74: The 2D reweighting "map" that shows the weights used in each scenario

S SLAC: Tooling Mechanical Drawings

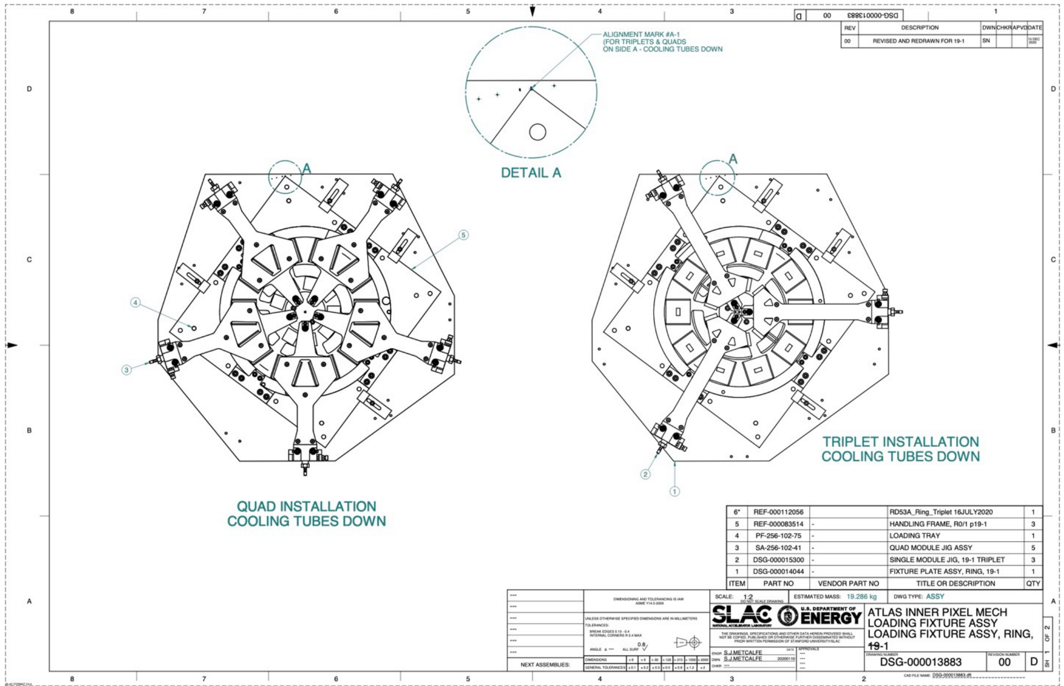

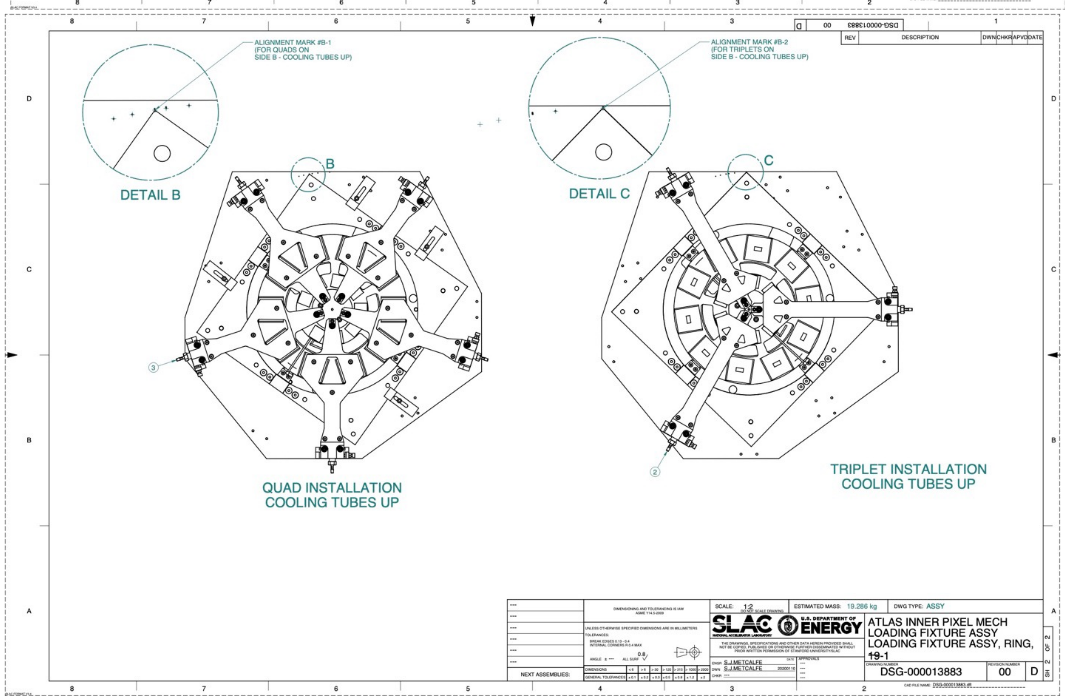

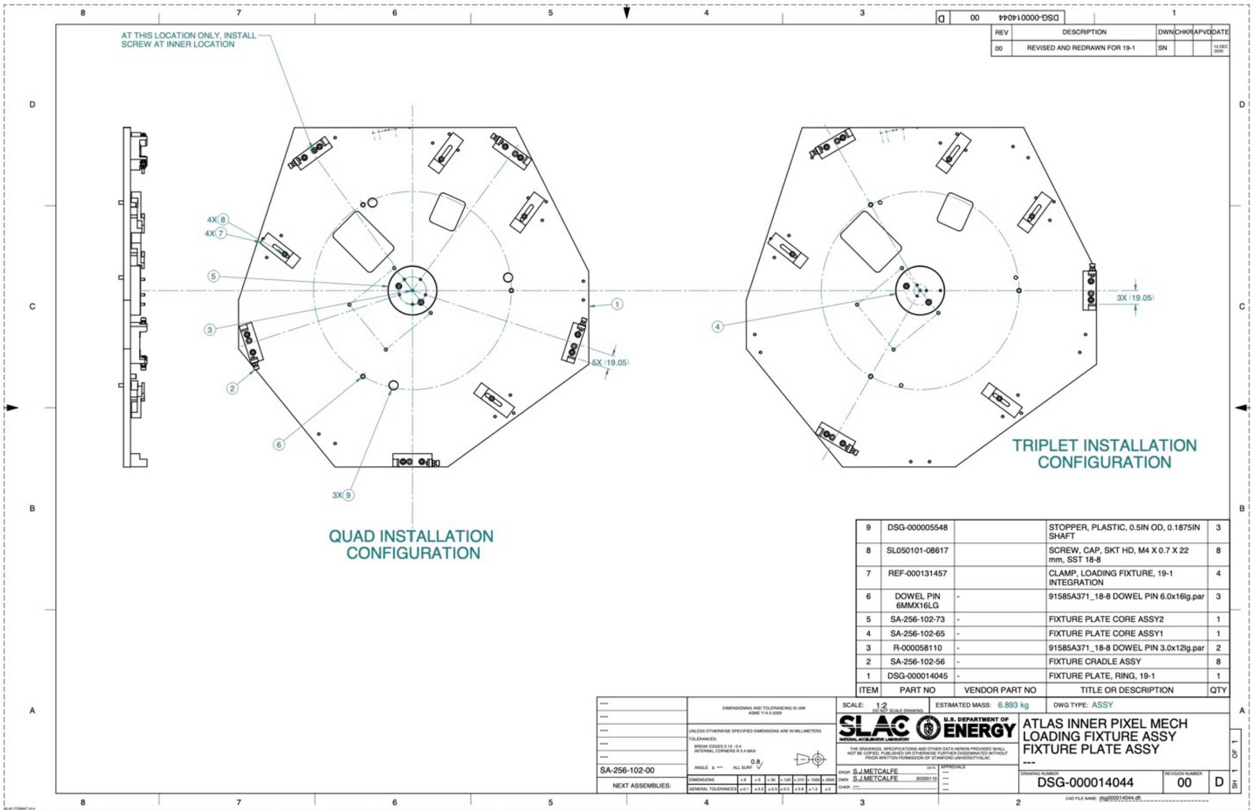

ITEM	PART NO	VENDOR PART NO	TITLE OR DESCRIPTION	QTY
9	DSG-000005548		STOPPER, PLASTIC, 0.5IN OD, 0.1875IN SHAFT	3
8	SL050101-08617		SCREW, CAP, SKT HD, M4 X 0.7 X 22 mm, SST 18-8	8
7	REF-000131457		CLAMP, LOADING FIXTURE, 19-1 INTEGRATION	4
6	DOWEL PIN 6MMX16LG	-	91585A371_18-8 DOWEL PIN 6.0x16lg.par	3
5	SA-256-102-73	-	FIXTURE PLATE CORE ASSY2	1
4	SA-256-102-65	-	FIXTURE PLATE CORE ASSY1	1
3	R-000058110	-	91585A371_18-8 DOWEL PIN 3.0x12lg.par	2
2	SA-256-102-56	-	FIXTURE CRADLE ASSY	8
1	DSG-000014045	-	FIXTURE PLATE, RING, 19-1	1

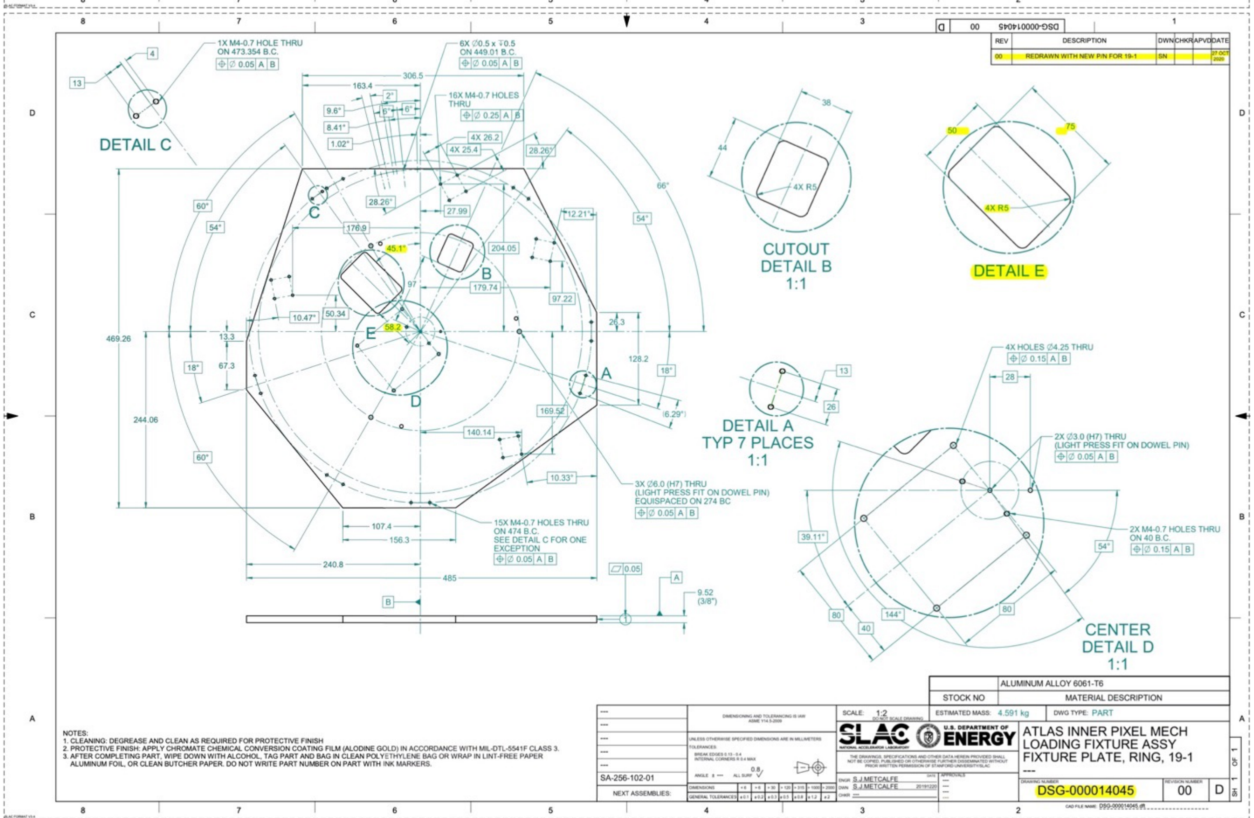

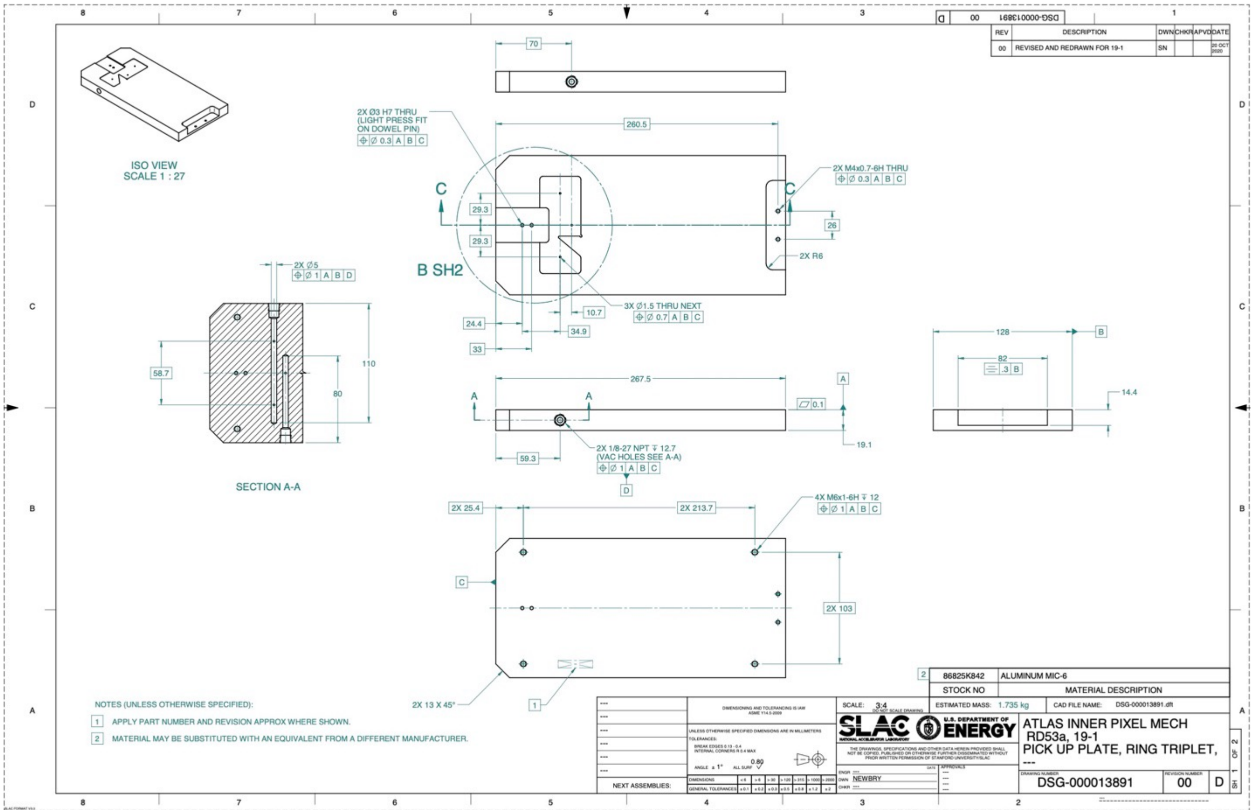
ISO VIEW
SCALE 1 : 27
SECTION A-A
B SH2
NOTES (UNLESS OTHERWISE SPECIFIED):
1 APPLY PART NUMBER AND REVISION APPROX WHERE SHOWN.
2 MATERIAL MAY BE SUBSTITUTED WITH AN EQUIVALENT FROM A DIFFERENT MANUFACTURER.
REVISED AND REDRAWN FOR 19-1
86825K842
ALUMINUM MIC-6
STOCK NO
MATERIAL DESCRIPTION
ESTIMATED MASS: 1.735 kg
SCALE: 3:4
ATLAS INNER PIXEL MECH
RD53a, 19-1
PICK UP PLATE, RING TRIPLET,
DSG-000013891
NEXT ASSEMBLIES:
NEWBRY

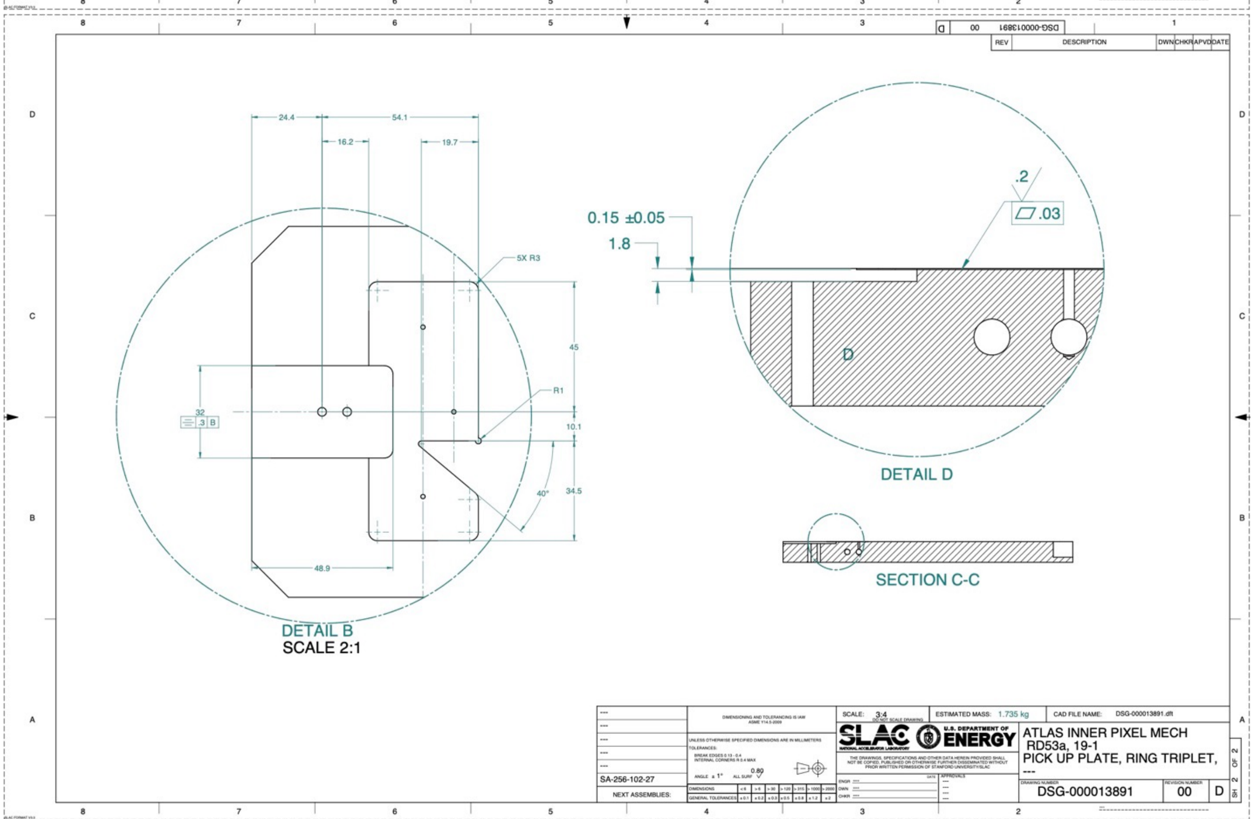
DETAIL B
SCALE 2:1
DETAIL D
SECTION C-C
0.15 ±0.05
1.8
ESTIMATED MASS: 1.735 kg
SCALE: 3:4
ATLAS INNER PIXEL MECH
RD53a, 19-1
PICK UP PLATE, RING TRIPLET,
DSG-000013891
SA-256-102-27
NEXT ASSEMBLIES:

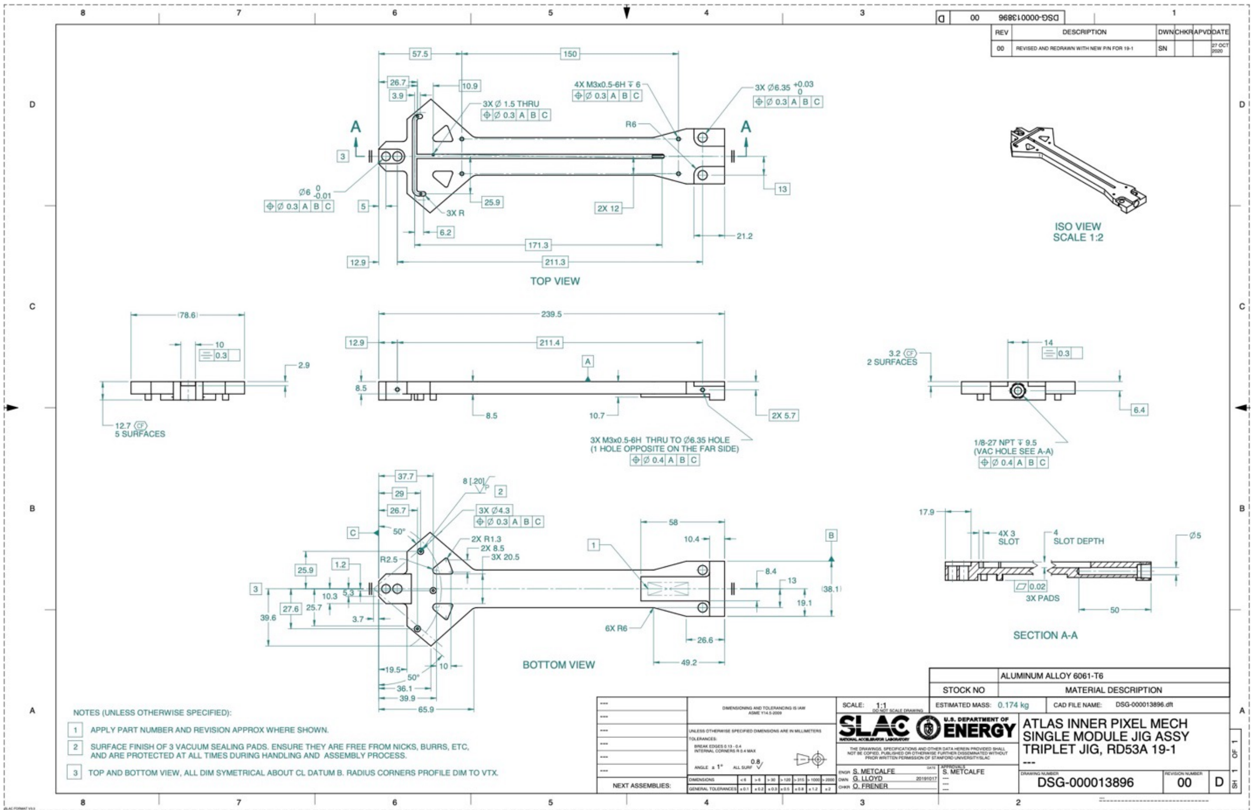
TOP VIEW
ISO VIEW
SCALE 1:2
BOTTOM VIEW
SECTION A-A
REV
DESCRIPTION
00
REVISED AND REDRAWN WITH NEW P/N FOR 19-1
NOTES (UNLESS OTHERWISE SPECIFIED):
1 APPLY PART NUMBER AND REVISION APPROX WHERE SHOWN.
2 SURFACE FINISH OF 3 VACUUM SEALING PADS. ENSURE THEY ARE FREE FROM NICKS, BURRS, ETC, AND ARE PROTECTED AT ALL TIMES DURING HANDLING AND ASSEMBLY PROCESS.
3 TOP AND BOTTOM VIEW, ALL DIM SYMETRICAL ABOUT CL DATUM B. RADIUS CORNERS PROFILE DIM TO VTX.
ALUMINUM ALLOY 6061-T6
STOCK NO
MATERIAL DESCRIPTION
ESTIMATED MASS: 0.174 kg
CAD FILE NAME: DSG-000013896.dft
SCALE: 1:1
SLAC
U.S. DEPARTMENT OF ENERGY
ATLAS INNER PIXEL MECH
SINGLE MODULE JIG ASSY
TRIPLET JIG, RD53A 19-1
S. METCALFE
G. LLOYD
Q. FRENER
NEXT ASSEMBLIES:
DSG-000013896
00
D

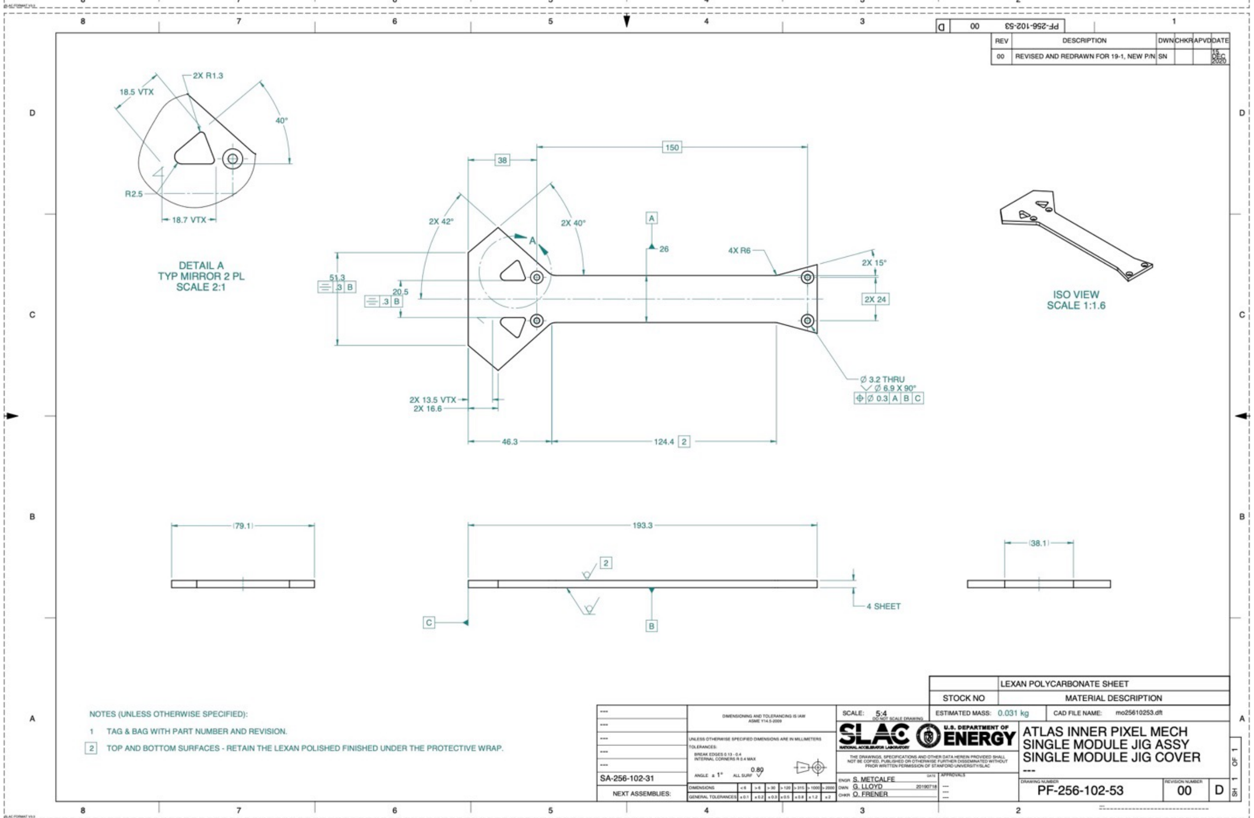
DETAIL A
TYP MIRROR 2 PL
SCALE 2:1
ISO VIEW
SCALE 1:1.6
REV
DESCRIPTION
00
REVISED AND REDRAWN FOR 19-1, NEW P/N
NOTES (UNLESS OTHERWISE SPECIFIED):
1 TAG & BAG WITH PART NUMBER AND REVISION.
2 TOP AND BOTTOM SURFACES - RETAIN THE LEXAN POLISHED FINISHED UNDER THE PROTECTIVE WRAP.
LEXAN POLYCARBONATE SHEET
STOCK NO
MATERIAL DESCRIPTION
ESTIMATED MASS: 0.031 kg
SCALE: 5:4
SLAC
U.S. DEPARTMENT OF ENERGY
ATLAS INNER PIXEL MECH
SINGLE MODULE JIG ASSY
SINGLE MODULE JIG COVER
SA-256-102-31
NEXT ASSEMBLIES:
S. METCALFE
G. LLOYD
Q. FRENER
PF-256-102-53
00
D

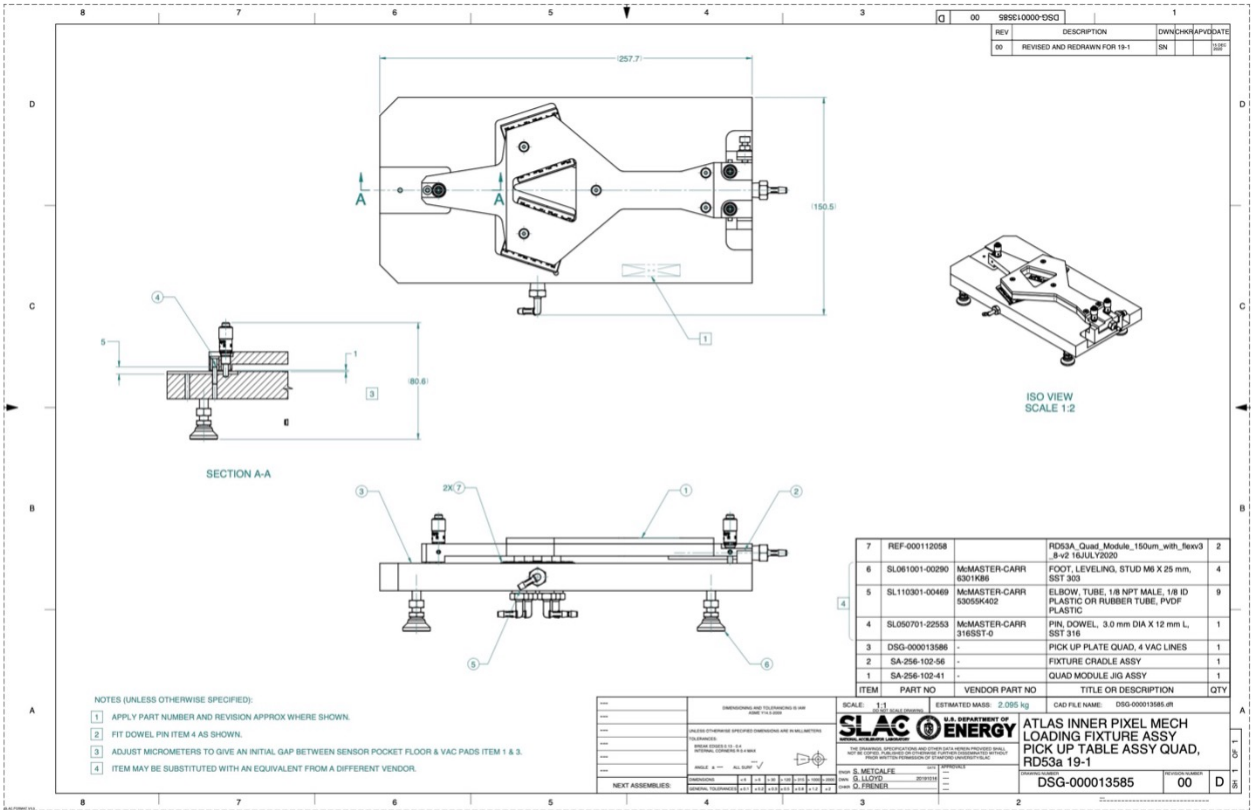
DSG-000013585 00
REV DESCRIPTION DWN CHKR APVD DATE
00 REVISED AND REDRAWN FOR 19-1 SN
257.7
150.5
80.6
SECTION A-A
ISO VIEW
SCALE 1:2
7 REF-000112058 RD53A_Quad_Module_150um_with_flexv3_8-v2 16JULY2020 2
6 SL061001-00290 McMASTER-CARR 6301K86 FOOT, LEVELING, STUD M6 X 25 mm, SST 303 4
5 SL110301-00469 McMASTER-CARR 53055K402 ELBOW, TUBE, 1/8 NPT MALE, 1/8 ID PLASTIC OR RUBBER TUBE, PVDF PLASTIC 9
4 SL050701-22553 McMASTER-CARR 316SST-0 PIN, DOWEL, 3.0 mm DIA X 12 mm L, SST 316 1
3 DSG-000013586 - PICK UP PLATE QUAD, 4 VAC LINES 1
2 SA-256-102-56 - FIXTURE CRADLE ASSY 1
1 SA-256-102-41 - QUAD MODULE JIG ASSY 1
ITEM PART NO VENDOR PART NO TITLE OR DESCRIPTION QTY
NOTES (UNLESS OTHERWISE SPECIFIED):
1 APPLY PART NUMBER AND REVISION APPROX WHERE SHOWN.
2 FIT DOWEL PIN ITEM 4 AS SHOWN.
3 ADJUST MICROMETERS TO GIVE AN INITIAL GAP BETWEEN SENSOR POCKET FLOOR & VAC PADS ITEM 1 & 3.
4 ITEM MAY BE SUBSTITUTED WITH AN EQUIVALENT FROM A DIFFERENT VENDOR.
NEXT ASSEMBLIES:
SCALE: 1:1
ESTIMATED MASS: 2.095 kg
SLAC
ENERGY
S. METCALFE
G. LLOYD
O. FRENER
ATLAS INNER PIXEL MECH
LOADING FIXTURE ASSY
PICK UP TABLE ASSY QUAD,
RD53a 19-1
DSG-000013585 00 D

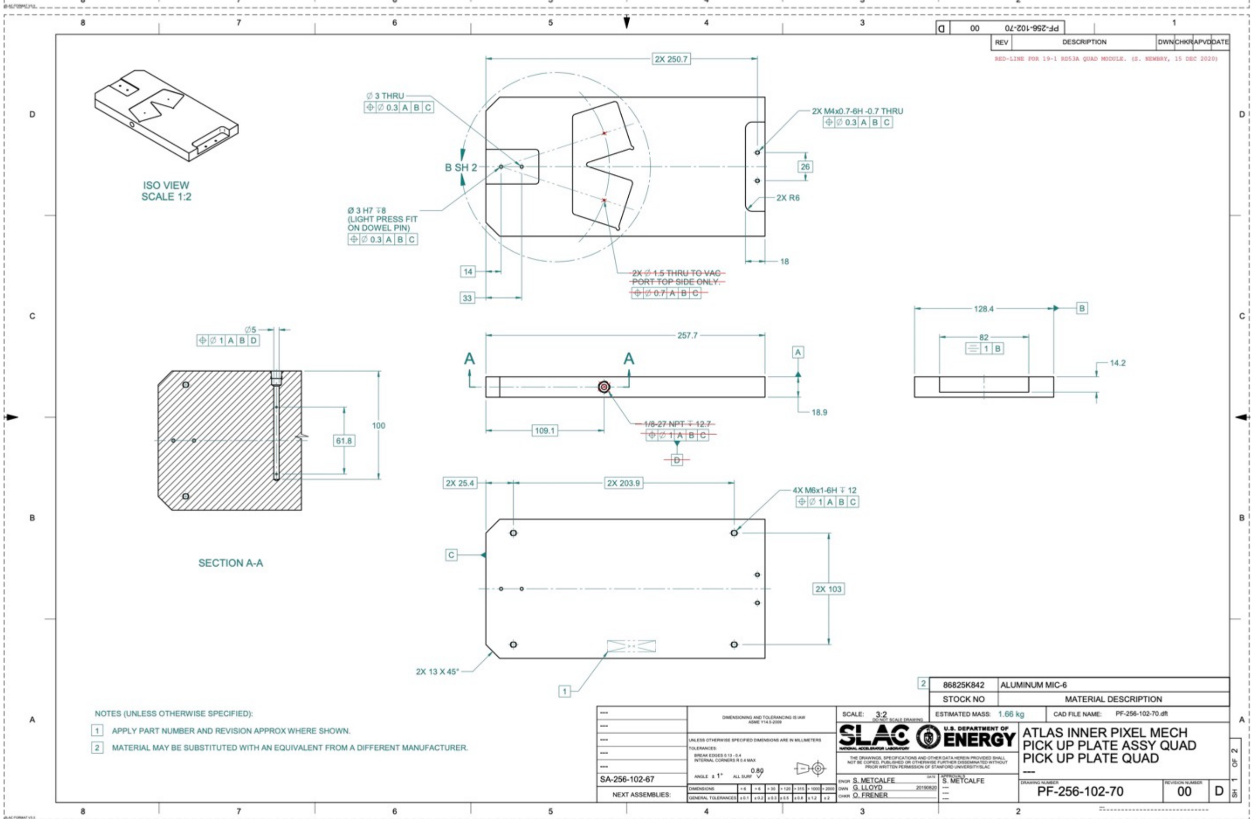
PF-256-102-70 00
REV DESCRIPTION DWN CHKR APVD DATE
RED-LINE FOR 19-1 RD53A QUAD MODULE. (E. NEWBRY, 15 DEC 2020)
ISO VIEW
SCALE 1:2
2X 250.7
Ø 3 THRU
2X M4x0.7-6H -0.7 THRU
B SH 2
26
2X R6
Ø 3 H7 ↧8
(LIGHT PRESS FIT
ON DOWEL PIN)
14
33
18
~~2X Ø 1.5 THRU TO VAC PORT TOP SIDE ONLY~~
257.7
128.4
82
14.2
18.9
109.1
~~1/8-27 NPT ↧ 12.7~~
100
61.8
SECTION A-A
2X 25.4
2X 203.9
4X M6x1-6H ↧ 12
2X 103
2X 13 X 45°
2 86825K842 ALUMINUM MIC-6
STOCK NO MATERIAL DESCRIPTION
NOTES (UNLESS OTHERWISE SPECIFIED):
1 APPLY PART NUMBER AND REVISION APPROX WHERE SHOWN.
2 MATERIAL MAY BE SUBSTITUTED WITH AN EQUIVALENT FROM A DIFFERENT MANUFACTURER.
SA-256-102-67
NEXT ASSEMBLIES:
SCALE: 3:2
ESTIMATED MASS: 1.66 kg
SLAC
ENERGY
S. METCALFE
G. LLOYD
O. FRENER
ATLAS INNER PIXEL MECH
PICK UP PLATE ASSY QUAD
PICK UP PLATE QUAD
PF-256-102-70 00 D

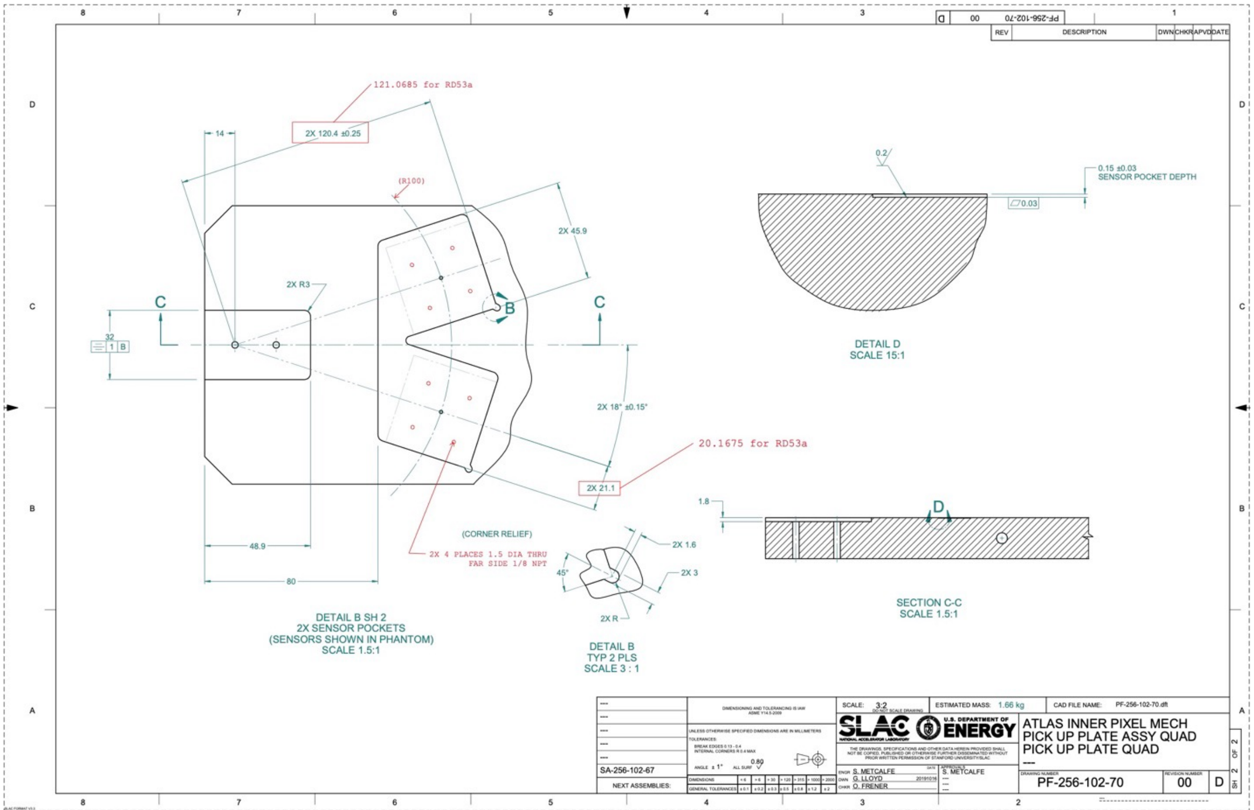
121.0685 for RD53a
2X 120.4 ±0.25
14
(R100)
2X 45.9
2X R3
C
B
C
32
1 B
2X 18° ±0.15°
20.1675 for RD53a
2X 21.1
48.9
80
(CORNER RELIEF)
2X 4 PLACES 1.5 DIA THRU
FAR SIDE 1/8 NPT
2X 1.6
45°
2X 3
2X R
DETAIL B SH 2
2X SENSOR POCKETS
(SENSORS SHOWN IN PHANTOM)
SCALE 1.5:1
DETAIL B
TYP 2 PLS
SCALE 3 : 1
0.2
0.15 ±0.03
SENSOR POCKET DEPTH
0.03
DETAIL D
SCALE 15:1
1.8
D
SECTION C-C
SCALE 1.5:1
PF-256-102-70
SA-256-102-67
NEXT ASSEMBLIES:
SCALE: 3:2
ESTIMATED MASS: 1.66 kg
CAD FILE NAME: PF-256-102-70.dft
SLAC
ENERGY
ATLAS INNER PIXEL MECH
PICK UP PLATE ASSY QUAD
PICK UP PLATE QUAD
S. METCALFE
G. LLOYD
O. FRENER
PF-256-102-70
00
D

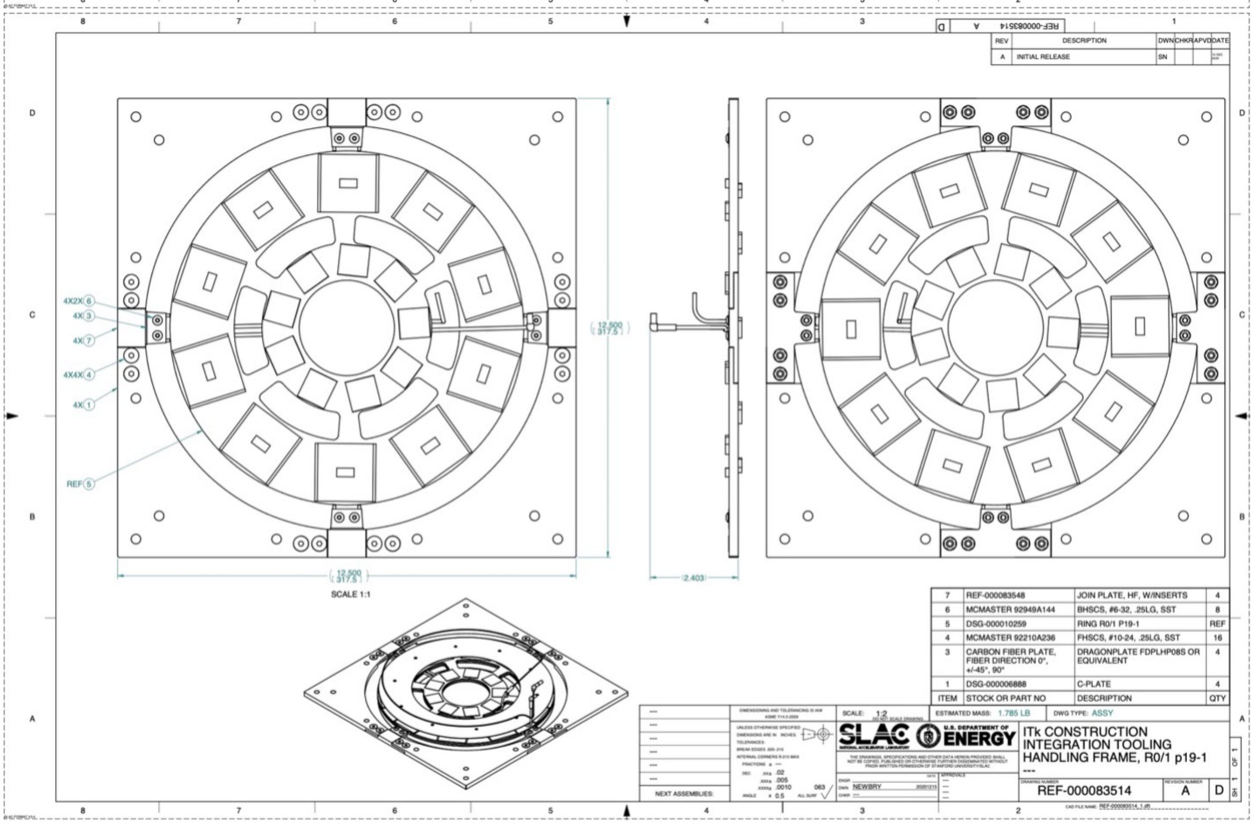
REF-000083514
INITIAL RELEASE
4X2X 6
4X 3
4X 7
4X4X 4
4X 1
REF 5
12.500
317.5
2.403
SCALE 1:1
7 | REF-000083548 | JOIN PLATE, HF, W/INSERTS | 4
6 | MCMASTER 92949A144 | BHSCS, #6-32, .25LG, SST | 8
5 | DSG-000010259 | RING R0/1 P19-1 | REF
4 | MCMASTER 92210A236 | FHSCS, #10-24, .25LG, SST | 16
3 | CARBON FIBER PLATE, FIBER DIRECTION 0°, +/-45°, 90° | DRAGONPLATE FDPLHP08S OR EQUIVALENT | 4
1 | DSG-000006888 | C-PLATE | 4
ITEM | STOCK OR PART NO | DESCRIPTION | QTY
SCALE: 1:2
ESTIMATED MASS: 1.785 LB
DWG TYPE: ASSY
SLAC
ENERGY
ITk CONSTRUCTION
INTEGRATION TOOLING
HANDLING FRAME, R0/1 p19-1
NEWBRY
REF-000083514
A
D
NEXT ASSEMBLIES:

VITA

Joshua Ryan Stewart

Candidate for the Degree of

Doctor of Philosophy

Dissertation: SEARCHES FOR VECTOR-LIKE QUARKS DECAYING TO W BOSONS AND MODULE PLACEMENT QUALITY ASSURANCE FOR THE ATLAS ITK UPGRADE

Major Field: Physics

Biographical:

Education:

Completed the requirements for the Doctor of Philosophy in Physics at Oklahoma State University, Stillwater, Oklahoma in May, 2024.

Completed the requirements for the Master of Science in Physics at Oklahoma State University, Stillwater, Oklahoma in June, 2022.

Completed the requirements for the Bachelor of Science in Physics at Cameron University, Lawton, Oklahoma in May, 2018.

Professional Membership:

American Physics Society